TU Delft

Delft University of Technology

The Singular Optics of Random Light
a 2D vectorial investigation

De Angelis, Lorenzo

DOI
10.4233/uuid:25dc497c-b218-4d6a-9796-001e9d569975

Publication date
2018

Document Version
Final published version

Citation (APA)
De Angelis, L. (2018). The Singular Optics of Random Light: a 2D vectorial investigation.
https://doi.org/10.4233/uuid:25dc497c-b218-4d6a-9796-001e9d569975

Important note
To cite this publication, please use the final published version (if applicable).
Please check the document version above.

Copyright
Other than for strictly personal use, it is not permitted to download, forward or distribute the text or part of it, without the consent of the author(s) and/or copyright holder(s), unless the work is under an open content license such as Creative Commons.

Takedown policy
Please contact us and provide details if you believe this document breaches copyrights.
We will remove access to the work immediately and investigate your claim.

This work is downloaded from Delft University of Technology.
For technical reasons the number of authors shown on this cover page is limited to a maximum of 10.

THE SINGULAR OPTICS OF RANDOM LIGHT

A 2D VECTORIAL INVESTIGATION

THE SINGULAR OPTICS OF RANDOM LIGHT

A 2D VECTORIAL INVESTIGATION

Proefschrift

ter verkrijging van de graad van doctor
aan de Technische Universiteit Delft,
op gezag van de Rector Magnificus Prof. dr. ir. T.H.J.J. van der Hagen,
voorzitter van het College voor Promoties,
in het openbaar te verdedigen op donderdag 20 december 2018 om 10:00 uur

door

Lorenzo DE ANGELIS

Master of Science in Physics,
Sapienza University of Rome, Italy,
geboren te Ronciglione, Italy.

Dit proefschrift is goedgekeurd door de

promotor: Prof. Dr. L. Kuipers
copromotor: Dr. S. Groeblacher

Samenstelling promotiecommissie:

Rector Magnificus	voorzitter
Prof. Dr. L. Kuipers	Technische Universiteit Delft
Dr. S. Groeblacher	Technische Universiteit Delft

Onafhankelijke leden:

Prof. Dr. H. P. Urbach	Technische Universiteit Delft
Prof. Dr. Ir. R. Hanson	Technische Universiteit Delft
Dr. S. Conesa-Boj	Technische Universiteit Delft
Prof. Dr. A. Mosk	Universiteit Utrecht
Prof. Dr. L. Marrucci	Università di Napoli Federico II
Prof. Dr. Y. Blanter	Technische Universiteit Delft, reservelid

Keywords: Light, phase, polarization, singularities, vortices, randomness, waves, chaos, correlation, 2D

Printed by: Gildeprint, Enschede

Front & Back: In the foreground, a phase singularity embed in a mask. In the background, the pattern produced by the spatial orientation of the polarization ellipse in 2D random light. Design advisor: Claudia Micheli.

Copyright © 2018 by L. De Angelis

Casimir PhD Series, Delft-Leiden 2018-48

ISBN 978-94-6186-995-1

An electronic version of this dissertation is available at
http://repository.tudelft.nl/.

All you need is love.

[1]The Beatles

CONTENTS

SUMMARY

In this thesis, we explore the physics of optical singularities. We investigate them in light waves propagating randomly in a planar nanophotonic chip. With a custom-built near-field microscope, we map the electromagnetic field resulting from the interference of these light waves. Our technique gives access to the full vectorial and complex nature of such an electromagnetic field, with subwavelength resolution. The resulting information allows us to precisely pinpoint and characterize the multitude of singularities that arise in the random light field. We detect phase singularities in the Cartesian components of light's vector field, i.e., points where the phase of the field components is undetermined and it circulates in a vortical flow around them (Part II). Moreover, we identify polarization singularities, e.g., C points: locations where the vector of light's electric field describes a perfect circle in time (Part III).

We experimentally determine the spatial correlation of phase singularities in the Cartesian components of vector random light waves, and compare it to the model for isotropic random waves. We demonstrate that, because of the vectorial nature of light, the spatial distribution of phase singularities becomes anisotropic. The anisotropy is caused by the direct relation between the wave propagation direction and the vector field orientation. This leads to an anisotropy in the propagation directions of the participating waves when considering a specific electric field component. We include this relation in existing scalar theory and find excellent agreement with our experiments.

We then consider the situation of isotropic random waves and determine the fluctuations of the topological charge for phase singularities, as a function of the size R of the observation window. We find that for two-dimensional fields such fluctuations increase with a super-linear scaling law, consistent with a $R \log R$ behavior. Additionally, we show that such scaling remains valid even in the presence of anisotropy.

As we tune an external parameter, namely the wavelength of the light field, phase singularities are displaced. When two of them are found at the same location, they have to have an opposite topological charge, resulting in their mutual annihilation. New pairs can be created as well. Supporting our experiments with theory and numerical simulations, we study the persistence and pairing statistics of phase singularities in random optical fields as a function of the excitation wavelength. We find a relation between the observed statistics and the eigenstate composition of the random light field. We find that the persistence of singularities that annihilate with their creation partner is smaller than that of singularities that "find another partner".

For C points in a two-dimensional random light field, we find that their spatial distribution is dramatically different when considering a truly two-dimensional field rather than a two-dimensional slice of a three-dimensional field. The most notable change is

that the probability of finding two C points with the same topological charge at a vanishing distance is actually enhanced in a two-dimensional field. These experimental findings are confirmed and supported with theory and excellent agreement is found between theory and experiment.

As a consequence of having two singularities with the same charge at the same location, higher-order singularities with twice the charge are created. We present the observation and the spatial correlation of these singularities – known as polarization vortices – in 2D random vector waves. We also discover that polarization vortices of positive charge occur more frequently than their negative counterpart. Such a symmetry breaking with respect to the polarization vortices' topological charge was unforeseen and surprising.

As a completion to the persistence studies performed for phase singularities, we also analyze persistence and pairing statistics of C points in random optical waves as a function of the excitation wavelength. Even though C points of different handedness are correlated in space, we observe that the influence that anti-handed dislocations exert on each other seems to be negligible for their evolution as a function of wavelength. We underpin this finding by computing the persistence statistics of C points, which behavior is highly similar to that observed for phase singularities in a the Cartesian components of the field.

Finally, we present with a quick overview some preliminary studies on singularities in random light, that offer interesting new avenues of research. These studies include the time evolution of phase singularities, the determination of an effective interaction potential for phase singularities from their pair correlation, and the transition from order to disorder as the number of waves which contribute to a random wave pattern is increased.

SAMENVATTING

Dit proefschrift beschrijft de fysica van optische singulariteiten. Deze singulariteiten ontstaan in het interferentiepatroon van vele lichtgolven die in willekeurige richtingen propageren over een vlakke nanofotonische chip. Door middel van een zelfbouw nabijeveld microscoop visualiseren we het interferentiepatroon. Onze techniek geeft toegang tot de volledige vectoriële en complexe eigenschappen van de elektromagnetische velden, met een ruimtelijke resolutie kleiner dan de golflengte van het licht. De gemeten informatie maakt het mogelijk om de optische singulariteiten precies te lokaliseren en te karakteriseren en geeft ons nieuwe inzichten in hun grote verscheidenheid. Wij meten fasesingulariteiten in de Cartesische componenten van het vectorveld van het licht. We vinden punten waar de fase van deze componenten ongedefinieerd is en waar het optische veld omheen wervelt (Deel II). Daarnaast nemen we ook polarisatiesingulariteiten waar, bijvoorbeeld C-punten: posities waar de elektrische veldvector van het optische veld een perfecte cirkel doorloopt in de tijd (Deel III).

We meten de ruimtelijke correlatie tussen de fasesingulariteiten in de Cartesische vectorcomponenten van het veld van de lichtgolven en vergelijken deze met een model voor isotrope wanordelijke golven. We laten zien dat doordat licht een vectorverschijnsel is, de ruimtelijke distributie van de fasesingulariteiten in een specifieke vectorcomponent anisotropisch wordt. Deze anisotropie komt doordat er een direct verband is tussen de voortplantingsrichting van een lichtgolf en de trilrichting van het elektrische veld. Wij voegen dit verband toe aan een scalaire beschrijving van het systeem, en vinden een uitstekende overeenstemming met de experimentele waarnemingen.

Wanneer we isotrope wanordelijke golven beschouwen, bepalen we de fluctuaties in de topologische lading van de fasesingulariteiten, als functie van de afmeting R van het waarnemingsvenster. We ontdekken dat zulke fluctuaties voor tweedimensionale velden groeien met een super-lineaire schalingswet, in overeenstemming met een $R \log R$ gedrag. Bovendien laten we zien dat deze schaalwet geldig blijft in de aanwezigheid van anisotropie.

Wij kunnen de fasesingulariteiten laten verplaatsen door een externe parameter, namelijk de golflengte van het licht, te variëren. Zodra twee singulariteiten zich op dezelfde positie bevinden, moeten deze een tegengestelde lading hebben, en zullen ze elkaar vernietigen. Naast het annihileren van singulariteitparen, kunnen er ook nieuwe paren ontstaan. Door onze experimentele waarnemingen te onderbouwen met theorie en numerieke simulaties, kunnen we de evolutie van de fasesingulariteiten en de statistieken van hun creatie-annihilatiebedrag bestuderen als functie van de excitatiegolflengte. Vervolgens vergelijken wij dit met de eigentoestanden van het wanordelijk lichtveld. Wij ontdekken dat singulariteiten die annihileren met hun creatiepartner een kleinere verandering om de golflengte “overleven” dan singulariteiten die “een andere partner vinden” om mee te annihileren.

Bij bestudering van de C-punten van een tweedimensionaal wanordelijk lichtveld, ontdekten we dat hun ruimtelijke verdeling drastisch afwijkt van hun verdeling in een tweedimensionale doorsnede van een driedimensionaal veld. Het duidelijkste verschil is dat de kans om twee C-punten te vinden met dezelfde topologische lading op een kleine onderlinge afstand in een echt tweedimensionaal veld toeneemt met de afstand. Ook in dit geval is er een uitstekende overeenstemming tussen onze experimentele waarnemingen en de theorie.

Als er zich twee singulariteiten met dezelfde lading op één plek bevinden, ontstaan er hogere orde singulariteiten met een dubbele lading. We nemen de ruimtelijke correlatie tussen deze nieuwe singulariteiten – bekend als polarisatie-vortices – in tweedimensionaal wanordelijk optische velden waar. We ontdekken daarnaast dat polarisatievortices met een positieve lading vaker voorkomen dan hun negatieve tegenhangers. Een dergelijke symmetriebreking in de topologische lading van de polarisatievortices is tegenintuïtief en verrassend. We hebben voor deze C-punten (net als voor de fasesingulariteiten) dezelfde evolutie en creatie-annihilatie statistiek bestudeerd als functie van de excitatiegolflengte. Ondanks het feit dat de C-punten van verschillende draairichting ruimtelijk zijn gecorreleerd, nemen we waar dat de invloed die de tegengesteld roterende singulariteiten op elkaar uitoefenen verwaarloosbaar is op de creatie-annihilatie statistiek. We onderbouwen deze vinding door de statistiek van de evolutie van deze C-punten uit te rekenen en vinden dat het gedrag sterk vergelijkbaar is met de waargenomen fasesingulariteiten in de Cartesische componenten van het veld.

Tenslotte geven wij een kort overzicht van enkele voorlopige vervolgstudies naar singulariteiten in wanordelijk licht, die nieuwe, interessante onderzoeksmogelijkheden bieden voor de toekomst. Deze studies omvatten de tijdsevolutie van fasesingulariteiten, het bepalen van een effectieve interactie potentiaal voor fasesingulariteiten gebaseerd op paarcorrelatie en de transitie van orde naar wanorde die plaatsvindt als het aantal golven dat bijdraagt aan een willekeurig golfpatroon wordt verhoogd.

I

INTRODUCTORY AND EXPERIMENTAL

1

LIGHT AND ITS SINGULARITIES

Happiness can be found in the darkest of times,
if one only remembers to turn on the light.

[2]Albus Dumbledore

In this introductory chapter we give a brief overview on wave optics and its singularities, introducing the few mathematical elements which are necessary to understand these entities. We then proceed to the main topic of this thesis: singularities in random waves. We position this thesis in the broader context of the investigation of wave phenomena and randomness in general. Subsequently, we explain how our work stands as a relevant completion of existing experiments and theories. Finally, we lay out the structure of this thesis with a concise summary of each chapter.

1

1.1. LIGHT

AMONG the myriad of planets orbiting in our universe, life could settle on earth. Many conditions were necessary for this magnificence to happen, one of which being the continual availability of light. The flow of energy supplied by the sun via light waves is indeed essential for life on our planet, straightforwardly for most plants, but for any living organism.

Relevance of light to our lives was already clear to early civilizations. The sun was worshiped in religious cults in Ancient Egypt, and light was already subject of investigation and speculation for Greek philosophers [1] and mathematicians [2]. Nowadays, we benefit of a deep scientific knowledge concerning light and its behavior in a wide variety of contexts. From ray optics and the first imaging instruments [3], to wave optics and the wonder of interference [4], all the way to quantum optics and the concept of photons [5], we are able to understand and influence the behavior of light at length scales spanning several orders of magnitude.

Such abilities caused modern societies to rely even more on light. In fact, we can collect and transform the energy of photons in order to power electric devices. Onto photons we encode information, which can be carried around the globe at the maximum speed one can reach, the speed of light. Even our meals can be warmed up with electromagnetic waves, which are just a bit *longer* than what we are used to call light.

But despite it being commonly used, light can still surprise us, and exhibit the most unpredictable behavior which could be at the basis of the technology of tomorrow. For this reason there is still a considerable effort in applied and fundamental research on light. In this thesis we focus on aspects of light which are called *singular* [6]. These are circumstances in which mathematics fails to describe some specific property of light as we express it [7]. Circumstances which may conceal weaknesses of the theories we use, opening the way for unexpected findings and innovation [8].

1.2. SINGULARITIES IN PHYSICS AND SINGULAR OPTICS

The concept of singularity is most clearly formulated in mathematics, as a point at which a given mathematical object is not defined or not "well-behaved", for example infinite or not differentiable [9]. Hence, singularities generally take place in anything that such a mathematical object can describe, from geometric curves [10] to physical quantities that we can measure. In fact, for as eccentric as it sounds, the observation of singularities is ubiquitous in physics, recurring in almost all its branches [11].

A very intriguing example are singularities of the space-time [12], points where the gravitational field diverges, which general relativity places in the inside of black holes. A more tangible case is the one of vortices. These are locations around which some quantity rotates, being undetermined in the middle. With this regard, a straightforward example is a water vortex, in which the direction of the flowing water rotates around the center of the vortex, where it is undetermined [13]. Quantum vortices are found in superconductors, as singularities of the order parameter, as well as in superfluids. In both cases, they play a leading role in understanding the superconducting/superfluid phase tran-

sition. Finally, also light exhibits optical vortices: points where the phase of the optical field is singular [14, 15].

In whichever domain of physics they occur, singularities are puzzling and fascinating. They are evocative of knowledge which is still not under our mathematical control, shifting our understanding from one theory to another, or from a length scale to a smaller one, or larger [8]. In this thesis we will focus our attention on the singularities exhibited by light described as a wave. These are phase and polarization singularities, the introduction of which requires some minimal notions on wave optics.

1.2.1. LIGHT AS A WAVE AND PHASE SINGULARITIES

In many circumstances light can be succesfully described as a wave. In fact, when ray optics breaks down, and before entering the quantum regime of single photons, light is effectively represented as an electromagnetic wave [16].

The easiest example of wave one could think of is a monochromatic plane wave

$$\psi_0(\mathbf{r},t) = A_0 \exp[i(\mathbf{k}\cdot\mathbf{r} - \omega t + \delta)], \tag{1.1}$$

propagating along the direction $\mathbf{k}$, with angular frequency ω, phase δ and amplitude A_0. For light, such a plane wave is the mathematical description of the coherent oscillations of the electric (or magnetic) field which constitutes light itself. In general, many plane waves with different amplitudes, frequencies and phases contribute to the formation of an optical field. The result is a complex field with a spatially dependent amplitude and phase, which can be expressed as

$$\begin{aligned} \psi(\mathbf{r},t) = & \sum_{\mathbf{k}} A_{\mathbf{k}} \exp[i(\mathbf{k}\cdot\mathbf{r} - \omega_{\mathbf{k}} t + \delta_{\mathbf{k}})] \\ = & \quad A(\mathbf{r},t) \exp[i\varphi(\mathbf{r},t)]. \end{aligned} \tag{1.2}$$

For a monochromatic field ($\omega_{\mathbf{k}} = \omega \ \forall \mathbf{k}$), the field in Eq. (1.2) is stationary and its time dependence is a single imaginary exponential

$$\psi(\mathbf{r},t) = \psi(\mathbf{r}) \exp[-i\omega t], \tag{1.3}$$

where $\psi(\mathbf{r})$ is a generic complex scalar field. Although scalar, in some cases this kind of function can be used to describe light, which is in general a vectorial quantity. For instance, we can use a scalar field to describe the field profile of a laser beam propagating in the paraxial regime. Figure 1.1 displays the typical field profile of a standard laser beam, exhibiting in its beam waist a Gaussian amplitude and a constante phase φ [16],

$$\psi_g(\mathbf{r}) \propto \exp[-r^2/2w^2]. \tag{1.4}$$

Having introduced a complex scalar field enables the explanation of the concept of phase singularity. In fact, there are situations in which the phase of a complex field cannot be defined [7]. These locations of undetermined phase are called phase singularities, in optics also known as optical vortices [15]. Phase singularities naturally arise in field patterns made of interfering waves. They appear at every location where destructive interference sets the amplitude of the field to be identically zero [17]. Again, the easiest

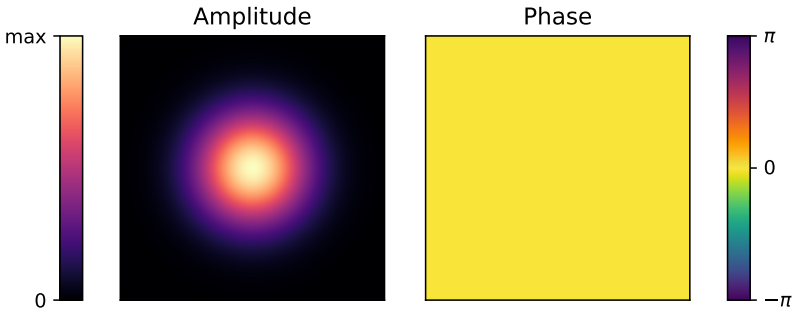

Figure 1.1: Profile (amplitude and phase) of a Gaussian beam [Eq. (1.4)]. The phase front of this beam is completely flat.

example of a phase singularity in a complex scalar field can be found in propagating light beams. In fact there is an entire class of beams which can exhibit phase singularities. These are Laguerre-Gaussian modes, in optics commonly called *vortex beams*. Figure 1.2 presents an example of a vortex beam with a topological charge $q = +1$. The charge q represents the net change of phase in a circuit $\mathscr{C}$ enclosing the phase singularity, quantized in units of 2π. For vortex beams, this is also equal to the quanta of orbital angular momentum $q\hbar$ carried by each photon in the propagating beam [15].

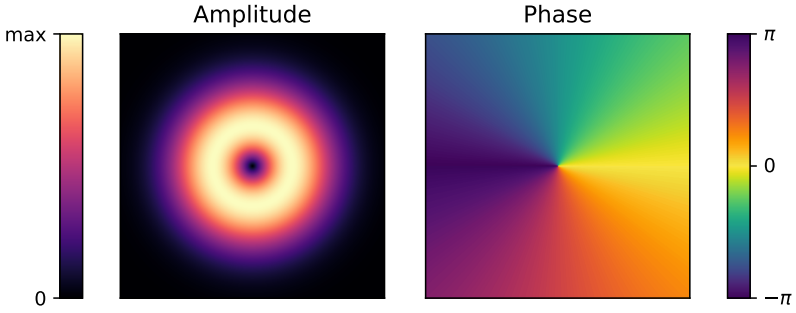

Figure 1.2: Profile (amplitude and phase) of a Laguerre-Gaussian beam of azimuthal index $l = 1$ and radial index $p = 0$. The beam exhibits a phase singularity with topological charge $q = 1$ in its center.

1.2.2. POLARIZATION AND C POINTS

So far we have limited our analysis to scalar quantities. However, light is in general described by a vector field. Particularly relevant to this case is the property of light called polarization. For a light beam, the polarization is the direction along which the electric field oscillates. The most intuitive case is that of linear polarization, for which the direction of oscillation is static as the wave propagates in time or space. This direction can also vary in time, describing circles or, in the most general case, ellipses. In these cases we talk about circular or elliptical polarization, respectively. Still, when the polarization of an optical field is homogeneous in space, the scalar description described in Section 1.2.1 can be effective. To give an example we can consider the Gaussian beam of Fig. 1.1, when this is linearly polarized along the horizontal direction $\hat{x}$. At the beam waist, it can simply be expressed as

$$\mathbf{E}(\mathbf{r}) = \hat{x}\, A_0 \exp[-r^2/2w^2], \tag{1.5}$$

which is a scalar field multiplied by the constant unit vector $\hat{x}$, with the exact same profile as the one presented in Fig. 1.1.

The picture becomes a lot richer when considering optical fields with spatially inhomogeneous polarization. This is the case whenever multiple waves with different phase and polarization contribute to generate an optical field. The expression of such a field now becomes a fully vectorial quantity, which requires a dedicated formalism for optimal representation.

For optical fields with their vector components lying in a plane (E_x, E_y), there are two very effective ways to quantitatively describe their polarization. The first is given by the Stokes parameters [18]:

$$S_0 = {E_x}^2 + {E_y}^2, \tag{1.6}$$

$$S_1 = {E_x}^2 - {E_y}^2, \tag{1.7}$$

$$S_2 = 2\,\mathrm{Re}(E_x {E_y}^*), \tag{1.8}$$

$$S_3 = -2\,\mathrm{Im}(E_x {E_y}^*). \tag{1.9}$$

S_0 represents the total intensity of the optical field, whereas each of the other parameters carries specific information on the polarization state of the field. S_1 is the parameter which indicates how much light is linearly polarized along the x ($S_1 > 0$) or y ($S_1 < 0$) direction. The information carried by the parameter S_2 is analogous to that of S_1, but for polarization oriented at ± 45 deg with respect to the x axis. Finally, S_3 is the parameter for circular polarization, positive for right-handed polarized light and negative for left-handed. In general, $\sum_{i=1}^{3} {S_i}^2 \leq {S_0}^2$, with the equality holding only for perfectly polarized states. This is also a way to quantify the degree of polarization of light [18],

$$\mathrm{DOP} = \frac{\sqrt{\sum_{i=1}^{3} {S_i}^2}}{S_0}, \tag{1.10}$$

equal to 1 for a perfectly polarized state and to 0 for unpolarized light.

For a more direct visualization of the polarization state, it is useful to normalize the last three parameters to the first. This new set of parameters $s_i = S_i/S_0$ can be used as

1

a coordinate system indicating a point in three dimensional space. In general, this is a point inside the unitary sphere depicted in Fig. 1.3, called the Poincaré sphere [18]. In this thesis we will focus on fully polarized states, which lie on the surface of this sphere. A point on the surface of the Poincaré sphere uniquely describes the polarization state of light.

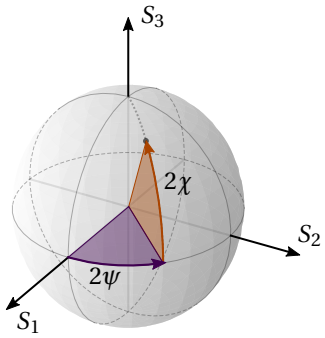

Figure 1.3: Illustration of the Poincaré sphere. The polarization state encoded in the parameters (s_1, s_2, s_3) defines a point in the sphere. When this state is perfectly polarized ($\sum_i {s_i}^2 = 1$), such point can also be determined by the two angles ψ and χ.

The second method to characterize polarization is given by the parametrization of its most generic elliptical state. To this end, we can define a polarization ellipse and parametrize it with its orientation angle ψ, ellipticity angle χ, and handedness h, i.e., the direction in which the electric field vector describes the ellipse in time (Fig. 1.4). Together, these three parameters also provide a complete description of light's polarization.

Whenever an optical field exhibits a spatial dependence of its polarization state, the Stokes parameters vary in space, and so does the polarization ellipse. Interestingly, the latter mathematical description of polarization intuitively highlights the potential presence of singularities. Namely, the orientation of the polarization ellipse ψ becomes un-

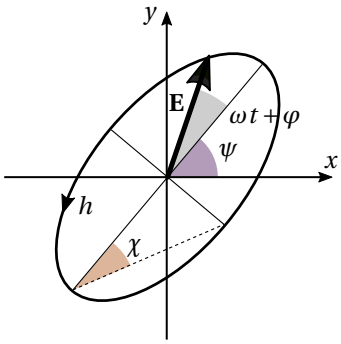

Figure 1.4: Illustration of the polarization ellipse used to describe the polarization state of light. The relevant parameters for the the definition of the ellipse are the orientation of the major axis ψ, the ellipticity angle χ and the handedness h. The last indicates whether the electric field vector $\mathbf{E}$ sweeps through the ellipse clockwise or anticlockwise.

determined as soon as the ellipse degenerates into a circle, leading to singularities of purely circular polarization known as C points. These are points in the plane, as it can be understood from the fact that in order to have purely circular polarization one has to satisfy $s_1 = s_2 = 0$, that is a system of two equations in two dimensions, which can be verified in a discrete set of points. Intuitively, in three-dimensional space C points become lines. Moreover, the ellipse handedness becomes ill defined for ellipses which collapse into a line, leading to singularities known as L lines ($s_3 = 0$). These two families of singularities also correspond to special locations on the Poincaré sphere, respectively the poles and the equator.

In this thesis we will focus on C points, dislocations that share a similar mathematical nature with phase singularities. Although C points are associated to completely different properties of the field with respect to phase singularities, being points of purely circular polarization rather than zeros of a scalar field, both entities are in fact still topological defects of a circulating angular variable. As opposed to phase singularities, for C points the circulation of such variable is a half integer times 2π (and multiple). This can be simply understood by the fact that the polarization ellipse is degenerate under rotation of π instead of 2π. Figure 1.5 presents as an example two C points of opposite topological index I. This is defined by the circulation of the orientation of the polarization ellipse

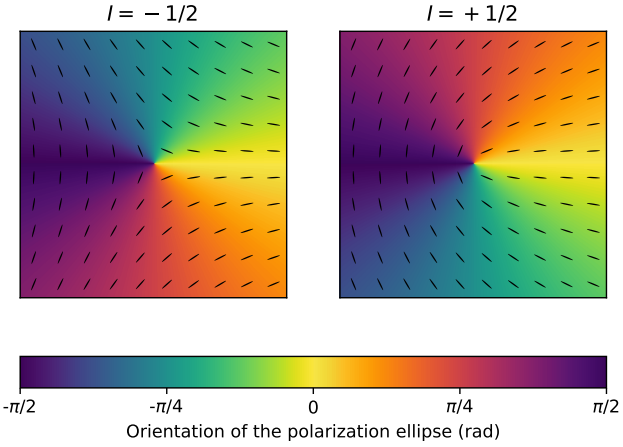

Figure 1.5: Example of C points with opposite topological index. The false-color map displays the orientation of the major axis of the polarization ellipse in a 2D plane, also indicated by the black directors. On the left panel a C point with topological index $I = -1/2$, and on the right with an index $I = +1/2$.

ψ around the singular point, in units of 2π. The orientation of the ellipse around the singularities is also depicted by its director (black lines). The pattern that this director field describes for the two different singularities is different for different indices [6], as it will be extensively discussed in Chapter 6.

While phase singularities attract interest for their connection to the orbital angular momentum of light [14], C points are representative of light's spin angular momentum [15]. In general, this is a topic of great interest and motif of investigation for fundamental

as well as applied research, as an important building block for light-matter interaction at the nanoscale [19–27]. From a fundamental science perspective, it is important to stress that C points are topological defects of the vector field which we use to describe light. As a consequence, they carry all the topological properties connected to dislocations. For example, they are topologically protected entities, meaning that a point where light is perfectly circularly polarized cannot be simply removed from a field [6]. This is only possible when two points of opposite topological index are combined. Note that this topological index is different from the handedness of a C point, i.e., its optical spin. Moreover, we stress that in principle higher order singularities are possible, and in particular we will discuss the case of a double rotation of an angle $\pm 2\pi$ which takes place in correspondence of second order C points, which we will address as polarization vortices.

As introduced also in this Section, optical singularities start to arise whenever interference among multiple light waves takes place. In this regard, arguably the most general case study one can think of is an ensemble of waves coming from all possible directions to randomly interfere. The study of random waves is indeed a well known and prosperous topic [28], and the physics of its singularities very rich. Describing it as an electromagnetic wave, we will use light as our tool to investigate singularities in random waves.

1.3. SINGULARITIES IN RANDOM LIGHT

The study of randomness is ubiquitous in science. Almost as much as the investigation of wave phenomena is dominant in physics. There is no mystery therefore for the incredible interest that the study of random wave fields has attracted in several communities in physics, whether this concerned the experimental realization or the theoretical modeling of the random patterns. A bold analogy was also made connecting the realm of random waves to quantum chaos, exploiting the equivalence of the Helmholtz equation with the stationary Scrödinger equation [28]. In this regard, several experiments and models have been developed, demonstrating fascinating analogies between classical and quantum systems [29–35].

Interestingly, singularities arise abundantly in fields created by randomly interfering waves. The behavior of dislocations in random waves was already source of interest for many theoretical and experimental physicists, starting from the pioneering works of Freund and coworkers [36–41] and Berry and Dennis [17, 42]. The physics of dislocations in random waves field was found to be very insightful for a comprehensive understanding of the wave field. This is especially true when considering the clear hallmark given by the spatial correlation of singularities in random waves, which makes it tempting to think of them as interacting entities [43–46]. Subsequently, knowledge and understanding grew hand in hand with technology, with several experiments performed in microwave chaotic billiards [47–49], with structured light beams generated via spatial light modulators [15, 50–52] as well as in light scattered by random media [53, 54]. The first series of studies was performed with a one-to-one correspondence to quantum mechanics in mind, in the second series an universal fractal behavior of singularities was unearthed, and in the third the focus was on Brownian statistics in relation to light in the diffusive regime. In all cases, interest for a broad physics community was again drawn.

In most of the models and experiments just mentioned, the investigations were performed either on fields described by scalar quantities or for vectorial light in the paraxial regime. However, light is fully vectorial in nature, and so are many other physical quantities of general interest. With the capability of resolving the polarization state of light fields confined in planar structures, we initiated the investigation of singularities in random light fields, while fully accounting for its vectorial nature. The many changes in the behavior of singularities which occur due to this vectorial nature are a central pillar of this work, and will be presented in detail.

1.3.1. THESIS LAYOUT

In this thesis, we study the collective behavior of optical singularities in light fields, with experiment, theory and numerical simulations. These investigations include spatial distribution as well as fluctuation and parametric evolution. The remainder of this first part of the thesis is devoted to introduce the experimental tools that allow our investigations. In the second part we focus our attention on phase singularities, whereas the third is dedicated to C points. Finally, the last part offers some additional leads for further ideas and analysis, as well as conclusions.

- In Chapter 2, we set the experimental framework, as we explain how to generate and detect two-dimensional random light fields at optical wavelengths.
- In Chapter 3, we explore the spatial distribution of phase singularities in the vector components of a transverse random light field.
- In Chapter 4, we present a study on the fluctuation of the topological charge in a finite observation window in relation to charge screening.
- In Chapter 5, we investigate the evolution of phase singularities in random light as the wavelength of the same optical field is varied.
- In Chapter 6, we study the spatial arrangement of C points in two-dimensional random light, with a special attention to the changes produced by the reduced dimensionality compared to the three-dimensional case.
- In Chapter 7, we discuss the occurrence of polarization vortices in two-dimensional random light, resulting from the superposition of pairs of same-index C points.
- In Chapter 8, we analyze the evolution of C points in random light as the wavelength is varied, drawing a relation to the evolution of phase singularities and to the occurrence of polarization vortices.
- In Chapter 9, we presents an outlook for additional studies that could be of interest to the rest of the thesis, such as effective interaction of phase singularities, evolution in time and the contrast between random and non-random waves.
- In Chapter 10, we draw the conclusions of our research on singularities in two-dimensional random waves.

2

GENERATION AND DETECTION OF 2D RANDOM LIGHT

I study people in their most ordinary occupations,
to see if I can succeed in discovering in others
what I feel that I myself lack in everything that I do:
the certainty that they understand what they are doing.

[3]Luigi Pirandello

As optical singularities are deep-subwavelength entities, their detection requires a precise measurement of the subwavelength structure of the field in which they occur. With near-field experiments, we probe a random light field and measure its amplitude, phase and polarization with subwavelength resolution. We generate the random field by coupling light into a chaotic resonator. This is a planar on-chip photonic crystal cavity with the shape of a quarter of a stadium. With a nanostructured probe we then detect the evanescent field which decays away above the surface of the resonator. By processing the complex data obtained from the experiment, we are able to determine all the vectorial and modal components of the random light field, allowing the study of optical singularities.

2.1. A PLATFORM FOR ON-CHIP RANDOM WAVES

To generate optical random waves, we couple monochromatic light at telecommunication frequencies into a chaotic cavity [55]. This cavity is a planar structure realized on a silicon-on-insulator platform, consisting of a 220 nm silicon slab on a 2µm thick silica buffer. A SEM image of the cavity is displayed in Fig. 2.1. From the figure, we can see that the shape of the cavity is enclosed by a photonic crystal, which was patterned in the silicon layer. Two ridge waveguides for in and out coupling are connected to the cavity via defect waveguides made of a single row of missing holes in the photonic crystal [56]. A detail of this structure is displayed in the zoomed-in image of Fig. 2.1, where a short fraction of the output ridge waveguides is also visible.

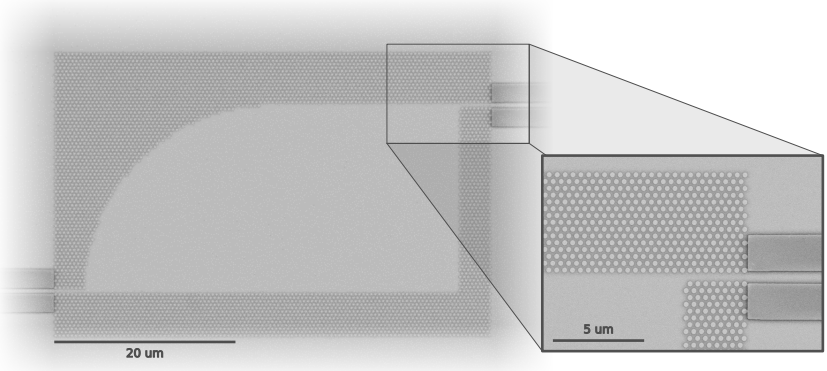

Figure 2.1: SEM image of the chaotic cavity used to generate random wave fields. The zoomed-in detail highlights the output waveguide, transitioning from a photonic crystal wavegui.

At a wavelegnth 1550 nm, the 220 nm thick silicon slab on glass supports the fundamental transverse electric (TE) and transverse magnetic (TM) electromagnetic modes. These optical modes have a strict relation between their vector field components and the wave propagation direction. The vectorial properties of the fields connected to these modes are depicted in Fig. 2.2 In the case of a TE mode the electric field **E** lies entirely in the plane of the slab, where it is perpendicular to the wave propagation direction, i.e., the in-plane wave vector $\mathbf{k}_{\text{in}}$. Instead, the magnetic field **H** is perpendicular to the total wave vector **k**, and to **E**. In fact, the magnetic field **H** of a TE mode has a longitudinal component, parallel to the propagation direction $\mathbf{k}_{\text{in}}$. The out-of-plane component of the wave vector **k** is purely imaginary, as the fields decay exponentially away from the surface and waves propagate in the plane only. For a TM mode electric and magnetic fields switch their roles, with the magnetic field **H** lying in the plane in the direction transverse to propagation, and the electric field having both out-of-plane and longitudinal components (Fig. 2.2).

At frequencies of approximately 1550 nm the photonic crystal which delimits the cavity does not support any TE mode, e.g., it exhibits a photonic band gap. Since for these frequencies TE light cannot enter the photonic crystal region, it will be reflected by the crystal, which effectively acts as a mirror. TE light will therefore be confined inside the

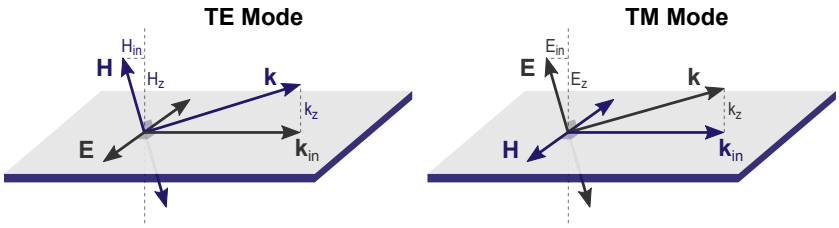

Figure 2.2: Illustration of the orientation of the optical electric and magnetic fields **E** and **H** for the case of a TE (left) and TM (right) mode.

chaotic cavity, the shape of which was designed to produce a random waves ensemble [55]. Optical cavities which support random wave propagation have been studied extensively in the context of microwave billiards [28]. This resulted in the identification of stadium-shaped cavities as the best platform for random random wave fields, with the added adaptation of only using a quarter of the total stadium shape to avoid unwanted symmetries in the system [28].

2.2. NEAR-FIELD MEASUREMENTS OF 2D RANDOM WAVES

2.2.1. NEAR-FIELD MICROSCOPY

We map the random light fields propagating in the chaotic cavity with a near-field microscope in collection mode [57]. We use a custom-built microscope that was developed in our group [58], as well as continuously upgraded [59], with features such as phase [60] and polarization resolution [61] or sensitivity to the optical magnetic field [61, 62]. A schematic of the near-field setup is displayed in Fig. 2.3. The core of this experimental technique consists of sensing the optical fields in a given sample by scanning its surface with a nanostructured probe. In our case, the probe is a tapered single-mode optical fiber coated with aluminum, the tip of which is truncated with a focused ion beam in order to have an aperture hole with a diameter of approximately 100 nm (Fig. 2.3) [63]. Different approaches can be pursued to image optical fields with subwavelength resolution [16, 64, 65]. A second powerful method is the so-called scattering type near-field microscopy, where an apertureless tip is used to scatter light to the free space, where it is then collected and measured [66–68]. In either case, a nanostructured probe is brought to within a height of tens of nanometers above the sample and then raster-scanned to map the near-field distribution. In general, the spectrum of application of different types of near-field microscopies is very broad, ranging from fundamental studies [69] to biology and nanomedicine [70], each type being more or less suited to each purpose.

In collection-mode near-field microscopy, the evanescent field which decays away from the surface of the sample under consideration is scattered by the aperture of the probe, exploiting a mechanism analogous to frustrated total internal reflection [58, 71]. As a result, a fraction of this evanescent wave is locally converted into a propagating wave which is then guided through the optical fiber from which the probe itself was fabricated. Scanning the probe over the surface of the sample allows the construction of an

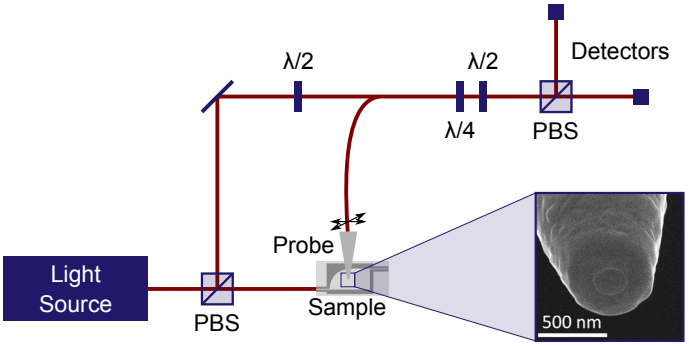

Figure 2.3: Schematic of the near-field setup used for the measurements presented in this thesis. The setup consists of a Mach-Zehnder interferometer, in which one of the two branches contains the near-field optical signal from the probe. Standard polarization optics is used to rotate the reference system of the polarized light signal collected with the probe. In the zoomed-in panel, a SEM picture of a typical near-field probe.

image of the optical fields in the sample, with a resolution limited by the characteristics of the nanostructured probe, rather than by the wavelength of light. A feedback mechanism based on shear-force interaction keeps the probe at a constant height of approximately 20 nm above the surface of the sample [72]. Once the optical near-field collected by the probe is delivered to the far field, we employ a heterodyne detection scheme for measuring amplitude and phase. This method essentially consists of an interferometric scheme in which the detected signal is combined with a reference beam extracted from the same laser used for the excitation of the sample. This reference beam is shifted in frequency by 40 kHz with a pair of acousto-optic modulators. This shift produces a beating in the interference of reference and signal beams, from which the signal can efficiently be extracted with lock-in methods [60]. With standard polarization optics we selectively detect the (E_x, E_y) Cartesian components of the in-plane electric field $\mathbf{E}$, thus gaining access to its vectorial content (see also section 2.2.5 of this chapter). The subwavelength resolution offered by near-field microscopy, as well as access to phase and polarization information, is a key feature in the detection of optical singularities [60, 61, 73]. As the investigation of these entities in random light is the main purpose of this thesis, we will now examine how we can use near-field microscopy to produce a vectorial mapping of the optical fields propagating in our chaotic cavity.

2.2.2. MAPS OF THE OPTICAL FIELD IN THE CHAOTIC CAVITY

With the near-field setup described in the previous section, we can produce maps the optical field propagating inside the chaotic cavity, resolving its amplitude, phase and polarization. As an example, Fig. 2.4 presents a measurement of the optical field in the entire cavity. The false-color map going from dark red to yellow is representative of the amplitude of the optical field, from low to high amplitudes, respectively. This image has an illustrative purpose, offering an overview on what the interference pattern produced by monochromatic light propagating in the cavity looks like.

For a more quantitative analysis, we measure the optical field in square regions positioned in the central part of the chaotic cavity. Figures 2.5(a)-(c) present the typical

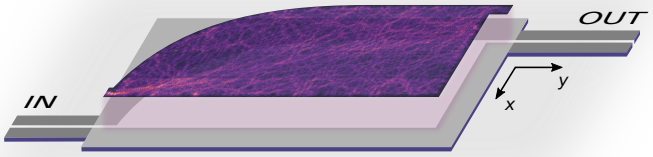

Figure 2.4: Example of a near-field measurement of the optical field in the entire chaotic cavity. The false-color map represents the amplitude of the electric field above the cavity, in which black corresponds to zero amplitude and white to high amplitude. The gray areas are a schematic representation of the chaotic cavity.

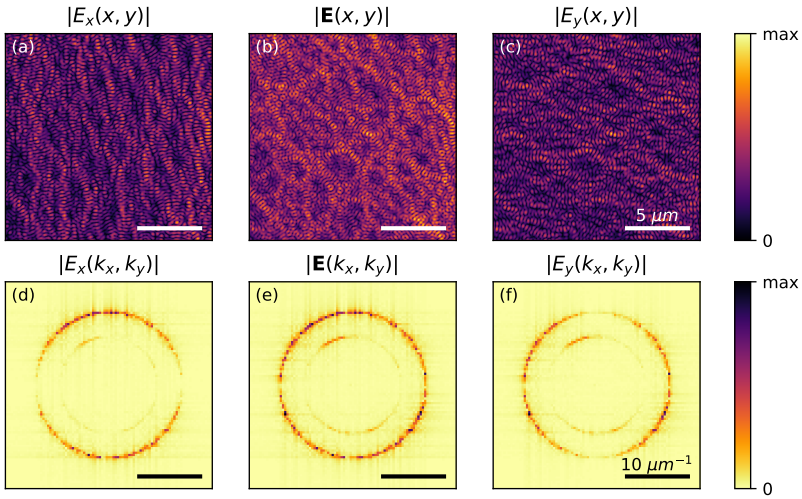

Figure 2.5: Example of a near-field map of the optical field in the chaotic cavity. The measurement is performed in a square area (17µm × 17µm) in the central region of the cavity. The first row of images (a-c) presents the amplitude of the x and y componente of the electric field (left and right), and the amplitude of the total in-plane electric field $|\mathbf{E}| = \sqrt{{E_x}^2 + {E_y}^2}$. In the second row (d-f) the amplitude of the Fourier decomposition $|\mathscr{F}[E_i]|$ for each of the fields displayed above. The Fourier image of $|\tilde{\mathbf{E}}(\mathbf{k})|$ displayed in (e) is obtained starting from those displayed in (d) and (f), $|\tilde{\mathbf{E}}(\mathbf{k})| = \sqrt{\tilde{E}_x(\mathbf{k})^2 + \tilde{E}_y(\mathbf{k})^2}$.

outcome of a measurement of the amplitude of the in-plane electric field [Fig. 2.5(b)] and of its Cartesian components E_x and E_y [Figs. 2.5(a) and (c)]. These components are computed in the reference system with the x axis parallel to the shorter side of the cavity, and the y axis to the longer side, as displayed in Fig. 2.4. In all the near-field maps of Fig. 2.5, we see a multitude of dark and bright spots, resulting from the interference of the light waves in the cavity. To better understand the origin of this interference pattern, it is useful to look at the Fourier decomposition of these fields, displayed in Figs. 2.5(d)-(f). Note that to numerically compute these Fourier images, it is essential to use the full complex information (amplitude and phase) of the field components $E_{x,y}$. In all of the three Fourier images in Fig. 2.5(d)-(f), we can recognize ring-like structures. A ring in Fourier space corresponds to an ensemble of waves which share the same amplitude for their wavevector, which is however oriented in every possible direction. De facto, this corresponds to an ensemble of monochromatic waves propagating in all directions. The result of the interference of these waves is the speckle-like pattern displayed in Figs. 2.5(a)-(c).

2.2.3. SEPARATION OF TE AND TM MODES

By having a closer look at the Fourier images of Fig. 2.5, we can identify more than one ring-like structure, for all field components. Actually, this is to be expected, since in Sec. 2.1 we already mentioned how the silicon slab supports two different modes, both the fundamental TE and TM. The two inner-ring features which appear in the Fourier images can indeed be related back to these two different modes. Inside the silicon these two modes experience a different effective refractive index n_{eff}, resulting in a different propagation constant k. We calculate these parameters by using a 1D mode solver for slab waveguides [74], searching for solutions of Maxwell's equation in a 220 nm silicon slab ($n = 3.48$) on glass ($n = 1.48$) and exposed to air ($n = 1$). With a free-space wavelength of 1550 nm we find that both the fundamental TE and TM modes are possible solutions. The field profiles corresponding to each mode are displayed in Fig. 2.6. The electric field is shown for the TE mode, and the magnetic for the TM. The mode solver also outputs the propagation constants of each mode: $k_{\text{TE}} = 11.5\,\mu\text{m}^{-1}$ and $k^{\text{TM}} = 7.8\,\mu\text{m}^{-1}$. By comparing these values to the radii of the ring structures displayed in Fig. 2.5, we can easily assign the outer ring of each figure to the TE mode, and the inner rings to the TM mode.

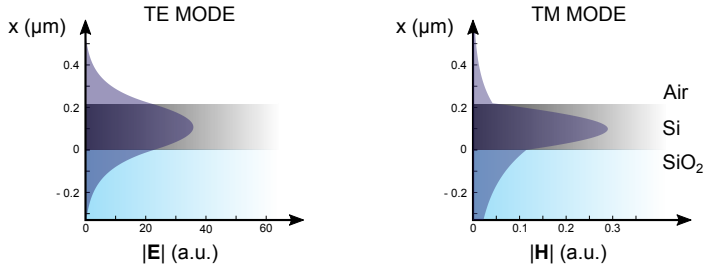

Figure 2.6: Field profiles of the fundamental TE (left) and TM (right) modes in a 220 nm silicon ($n = 3.48$) slab between air ($n = 1$) and glass ($n = 1.48$). We show the field profile of the electric field $|\mathbf{E}|$ the TE mode and of $|\mathbf{H}|$ for the TM [74].

It is important to notice that the ring associated to the TM mode is far from being a perfect ring, since it does not have equal intensity at every possible direction in k space. As briefly discussed in Section 2.1, the photonic crystal which determines the boundaries of the chaotic cavity is designed to have a bandgap for the TE mode but not for the TM. Hence, TM light can easily leave the cavity through its boundaries. As a result, it is not randomized by being reflected multiple times towards the inner region like the TE mode does. Since in this thesis we aim at analyzing the collective behavior of optical singularities in random light fields, we will filter out the data correspondent to the TM mode, as it is not a random field, and focus on the TE light only. This is an easy operation to perform in Fourier space, as illustrated in Fig. 2.7. We construct a ring with a radius equal to k_{TE} and a Gaussian profile [$\sigma = 4$ pixels $\approx 0.1\, k_{\mathrm{TE}}$, see Fig. 2.7(c)] and multiply this *mask* to the Fourier decomposition of the fields, e.g. to $E_x(\mathbf{k})$. After applying the mask, only the ring correspondent to the TE mode will be left in $E_x(\mathbf{k}) = E_x^{\mathrm{TE}}(\mathbf{k})$ [Fig. 2.7(d)]. Transforming back the field to real space will then lead to the filtered field $E_x^{\mathrm{TE}}(x, y)$, in which only the contribution of the TE mode is present.

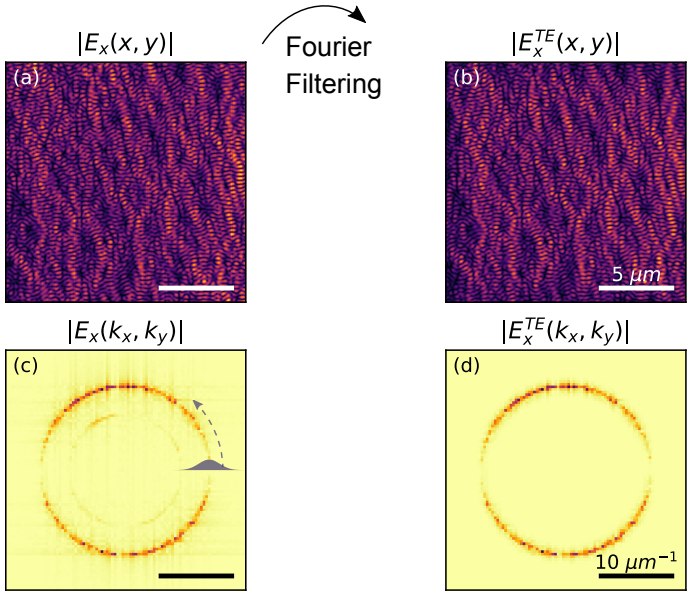

Figure 2.7: Illustration of the procedure used for filtering the TM mode out of the collected data. The purple Gaussian profile displays a 1D section of the Gaussian ring used for the Fourier filtering.

2.2.4. ELECTRIC AND MAGNETIC CONTRIBUTION TO THE DETECTED FIELD

From different studies in the literature [75–79] and from experiments performed with our own microscope [62], we know that a near-field probe is not only sensitive to the electric optical field, but it can detect the magnetic component as well. However, in [62] it was demonstrated that with our typical aperture probes E_x is always detected together with H_y, both contributing to the detected signal

$$L_x = \alpha E_x + \beta H_y, \tag{2.1}$$

where α and β are two complex constants [80]. In complete analogy E_y is collected with H_x and together they lead to L_y. Conveniently enough, in the case of a mode propagating in a planar structure, the paired electric and magnetic components of the fields coincide up to a constant, e.g., $H_y \propto E_x$ and $H_x \propto E_y$. To give an example, in the studied case of a TE mode we have that the electric field can be expressed as a function of the out-of-plane magnetic field,

$$\mathbf{E} \propto \begin{pmatrix} -k_y \\ k_x \\ 0 \end{pmatrix} H_z, \tag{2.2}$$

as it can be derived from the rotation equation for the electric field $\mathbf{H} \propto \nabla \times \mathbf{E}$. Additionally, combining the divergence equation for the magnetic field ($\nabla \cdot \mathbf{H} = 0$) and the z component of the rotation equation for the magnetic field ($\nabla \times \mathbf{H}|_z \propto E_z = 0$), we obtain

$$\mathbf{H} \propto \begin{pmatrix} k_z k_x \\ k_z k_y \\ k_{\text{in}}^2 \end{pmatrix} H_z, \tag{2.3}$$

where k_{in} is the amplitude of the in-plane wavevector ($k_{\text{in}}^2 = k_x^2 + k_y^2$) and k_z is the out-of-plane component, which is purely imaginary and describes the decay of the evanescent wave away from the surface of the 2D structure. Combining the information displayed in Eqs. (2.2) and (2.3), it is easy to notice that $H_y \propto E_x$ and $H_x \propto E_y$, and therefore

$$L_x = \alpha E_x + \beta H_y = \alpha E_x + \beta' E_x \propto E_x, \tag{2.4}$$

and analogously for E_y. The result of Eq. (2.4) is that what we measure in our experiments is indeed a combination of electric and magnetic field components, but that the measured signal is still equivalent to the electric (or magnetic) field alone. For ease of notation, in the rest of the thesis we will denote our measurements as maps of the optical electric field in the cavity.

2.2.5. PROJECTION OF THE POLARIZED LIGHT INTO THE $x-y$ BASIS

In Fig. 2.5 we have already introduced the measurements of the different projections of the vector field $\mathbf{E}$ in the $x-y$ basis. However, from an experimental point of view, the separation of the different vector field components is an often important but non-trivial operation in the context of near-field microscopy [81–85]. This is also because in propagating from the near-field probe, through the optical fiber, all the way to the detection

stage of our setup (Fig. 2.3), the reference system for the polarization of light on the surface of the sample typically undergoes a generic rotation. Moreover, birefringence effects in the bent optical fiber can induce slight variations in the ellipticity of the light's polarization. To invert such transformations, we use a quarter and a half waveplate just before projecting on the $x-y$ basis with a polarizing beam splitter (Fig. 2.5). But the rotation angle for these waveplates, which allows the transformation to be properly inverted, needs to be calibrated [80]. To do so, one can rely on known symmetries of the system under study, e.g., symmetric or antisymmetric modes in photonic waveguides [62], or on reference measurements on structures with a known mode profile. In the case of a random field we lack any kind of easy symmetry in the real space data. However, a symmetry of the electromagnetic modes can be exploited in Fourier space, where a very strict relation holds among wavevector and polarization. Precisely, in a TE mode the orientation of the in-plane electric field vector $\mathbf{E}$ is always perpendicular to the in-plane wavevector $\mathbf{k}_{\text{in}}$. This means that when considering the x-polarized field E_x only, we should not observe waves propagating along the x direction, and analogously for E_y. This is indeed clearly visible in the Fourier images of Fig. 2.5, where in the ring correspondent to the TE mode the amplitude vanishes at $k_y = 0$ for E_x, and at $k_x = 0$ for E_y.

This relationship between field direction and propagation direction forms the basis of our procedure for splitting the polarization in the two measured channels E_x and E_y. First, while performing a series of near-field maps of the same area we rotate the waveplates l_1 and l_2 in the setup (Fig 2.3), so to have mainly propagation along y in one channel and along x in the other. Then, we refine the outcome of our measurements in the analysis stage, by applying a virtual pair of waveplates through the Stokes formalism [18], and optimizing their rotation angle so to have

$$E_x(-k_{\text{TE}},0) = E_x(k_{\text{TE}},0) = E_y(0,-k_{\text{TE}}) = E_y(0,k_{\text{TE}}) = 0, \tag{2.5}$$

where k_{TE} is the amplitude of the TE mode wavevector $2\pi n_{TE}/\lambda_0$.

How accurately we are able to select the two orthogonal polarizations E_x and E_y strongly depends on the resolution in Fourier space, which is determined by the size of the maps in real space. With the 17 µm × 17 µm maps displayed in Figs. 2.5 and 2.7 we are able to achieve a level of unwanted signal of less than 1%, as estimated by the ratio $E_y(k_{\text{TE}},0)/E_x(k_{\text{TE}},0) > 100$.

2.3. SUPPLEMENTARY INFORMATION

2.3.1. RANDOMNESS OF THE MEASURED WAVE FIELD

From a mathematical point of view, for a wave field to be random it means that its real and imaginary parts,

$$\psi(\mathbf{r}) \doteq \xi(\mathbf{r}) + i\eta(\mathbf{r}), \tag{2.6}$$

and their derivatives, are independent Gaussian random functions [17]. This is a consequence of the central limit theorem, and it implies that the field intensity $|\psi|^2 = \xi^2 + \eta^2$ is distributed according to a chi-squared distribution with two degrees of freedom, i.e., an exponential function [86]. Figure 2.8 presents the probability density function for the intensities of the experimentally measured field components E_x^{TE} and E_y^{TE}. We assume Poissonian uncertainty on each data point of Fig. 2.8, computed by counting the occurrence of a given intensity I in our experimental maps [$\sigma(N) = \sqrt{N}$], and then normalized. The experimental distributions of the two components are consistent with respect to each other, suggesting that there are no anisotropy effects due to the shape of the sample. Both are in excellent agreement with the expected exponential behavior, underlying the randomness.

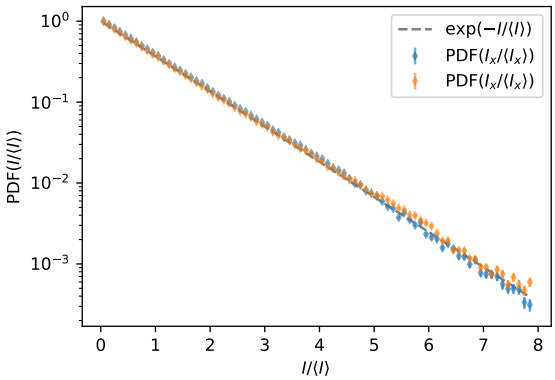

Figure 2.8: Probability Density Function (PDF) for the intensities I_x and I_y of the components of the electric field **E** associated to the TE mode in the cavity. The intensities are expressed in units of their spatial averages and the integral of the distribution functions is normalized to unity. The PDFs thus determined from our experimental data (diamonds) are compared with an exponential distribution (line).

II

PHASE SINGULARITIES

3

SPATIAL DISTRIBUTION OF PHASE SINGULARITIES IN VECTOR RANDOM WAVES

There is no reason why because it is dark
you should look at things differently from when it is light.
The hell there isn't.

[4]Ernest Hemingway

Phase singularities are dislocations widely studied in optical fields as well as in other areas of physics. With experiment and theory we show that the vectorial nature of light affects the spatial distribution of phase singularities in random light fields. While in scalar random waves phase singularities exhibit spatial distributions reminiscent of particles in isotropic liquids, in vector fields their distribution for the different vector components becomes anisotropic due to the direct relation between the wave propagation direction and the field orientation. By incorporating this relation in the theory for scalar fields by Berry and Dennis, we quantitatively describe our experiments.

Parts of this chapter have been published in Physical Review Letters **117**, 093901 (2016) [87].

3.1. INTRODUCTION

FINDING correlations in chaotic systems is the first step towards understanding. Many are the fields where such predictions could be exploited, from weather forecast to economic modeling [88, 89]. The study of random phenomena is a topic of great interest and inspiration for many branches of physics as well. In electromagnetism, for example, random wave fields have been a topic of intense studies since decades, an outstanding example being Anderson localization of light [90]. More recently the scientific interest on random wave fields has continued intensively, ranging from useful techniques as non-invasive imaging with speckle correlation [91] to fascination concerning the observation of rogue waves in optical fields [55, 92]. Zooming into the structure of a random wave field, attention has been pointed to deep-subwavelength dislocations known as phase singularities [7].

Phase singularities are locations in which the phase of a scalar complex field is not defined. In two-dimensional fields these locations are points in the plane. Although they are just a discrete set of points, phase singularities can describe the basic properties of the field in which they arise. For this reason they are widely studied in wave fields [36, 93–98], as well as in many areas of physics, where they are better-known as topological defects in nematics [99] or as vortices in superfluids [100].

For a single frequency phase singularities are fixed in space, and their spatial distribution in a scalar field of monochromatic random waves has been analytically modeled by Berry and Dennis [17]. The hallmark of such a distribution is a clear pair correlation, reminiscent of that of particles in liquids. By realizing random waves ensembles in microwave billiards [28, 48, 101], the correlation of phase singularities was tested for a field perpendicular to the plane of the billiard, showing excellent agreement with the theoretical expectations [102]. For such a field and in that geometry indeed scalar theory was appropriate. However, electromagnetic waves are vectorial in nature, and in a different framework it was already demonstrated how the presence of a spin degree of freedom can affect the correlation properties of a random field [103, 104].

Here, we show how the vectorial nature of light affects the distribution of its phase singularities. By mapping the in-plane optical vector field measured above a chaotic resonator, we investigate the distribution of phase singularities in two-dimensional random vector waves. We show that the distribution of phase singularities deviates from that for scalar random waves. This deviation is caused by the relation between the transverse field and waves propagation direction. Thus, even when the considered vector field is equipartitioned with respect to both the in-plane polarization and propagation direction, any specific choice of field component directly leads to an anisotropic distribution of the contributing propagation directions. By treating this anisotropy with an analytical model, we quantitatively explain our experimental observations. Finally, we show how an out-of-plane component that we construct from our in-plane fields obeys the predictions for scalar fields.

3.2. DETECTION OF PHASE SINGULARITIES IN RANDOM LIGHT

3.2.1. NEAR-FIELD MEASUREMENTS

As discussed in Chapter 2, we generate optical random waves by injecting monochromatic light ($\lambda_0 = 1550\,\text{nm}$) in a chaotic cavity, and measure the in-plane components of the optical field therein. Figure 3.1 presents the measurements of the amplitude of E_x and E_y. At first sight destructive and constructive interference occurs at random locations in the plane. On closer inspection a difference between the maps of the two field components catches the eye: the features of each pattern exhibit a preferred axis, related to the specific field component. A vertical stripy pattern with roughly $1-2$ micrometers between the stripes is present in the E_x field. A modulation of the amplitude is observed along the stripes as well, characterized this time by a shorter length scale. The case of E_y is completely analogous, but rotated by 90 degrees.

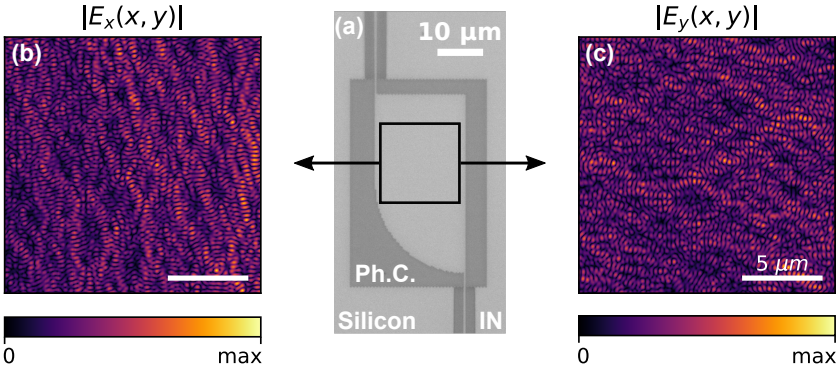

Figure 3.1: Near-field measurement of the amplitude of the two cartesian component E_x (b) and E_y (c) of the optical electric field in the *Chaotic Cavity* (optical micrograph shown) (a).

3.2.2. POSITION AND TOPOLOGICAL CHARGE PINPOINTING

By separately measuring the Cartesian components of the electric field we implicitly established a criterion to depict a vector $\mathbf{E}$ by using two complex fields (E_x, E_y), in which we can now seek for phase singularities [8]. Please note that such singularities cannot be found in the total intensity, which has no vanishing points. In a two-dimensional scalar complex field $\psi(\mathbf{r})$, phase singularities are points in which the phase φ of this field is undefined. The phase circulates around the singular points, assuming all its possible values from $-\pi$ to π [7]. Quantitatively, the line integral of φ along a path $\mathscr{C}$ enclosing only one singularity yields an integer multiple of 2π:

$$\int_{\mathscr{C}} d\varphi = 2\pi q, \tag{3.1}$$

where the integer q is called *topological charge* of the singularity. The definition of topological charge also gives us a powerful way to identify phase singularities.

We calculate the integral of Eq. (3.1) along 2×2 pixels loops at every point of the measured phase map, determining position and topological charge of all the optical vortices in the field, with a spatial accuracy that is limited by the pixel size, of approximately 20 nm. The computation of the integral in Eq. (3.1) is implemented with the trapezoidal rule, with some extra attention needed, because at each pixel j the value of the phase φ_j is defined up to a multiple of 2π. Indicating the pixels in the loop as $j = 1, 2, 3, 4$, the integral is computed by adding the phase differences between each pair of pixels,

$$q = \frac{1}{2\pi}[\Delta\varphi_{1,2} + \Delta\varphi_{2,3} + \Delta\varphi_{3,4} + \Delta\varphi_{4,1}],$$

with each difference being individually remapped to the interval $[-\pi, \pi]$:

$$\Delta\varphi_{j,k} = [(\varphi_j - \varphi_k + \pi) \mod 2\pi] - \pi.$$

The circulation integral is taken counterclockwise, following the convention of complex analysis. In general q will be equal zero, but in presence of a singularity it will be an integer number, with a positive or negative sign. Figure 3.2 shows the phase singularities pinpointed in a subset of the phase map of E_x. In this experiment, only topological charges of ±1 are observed.

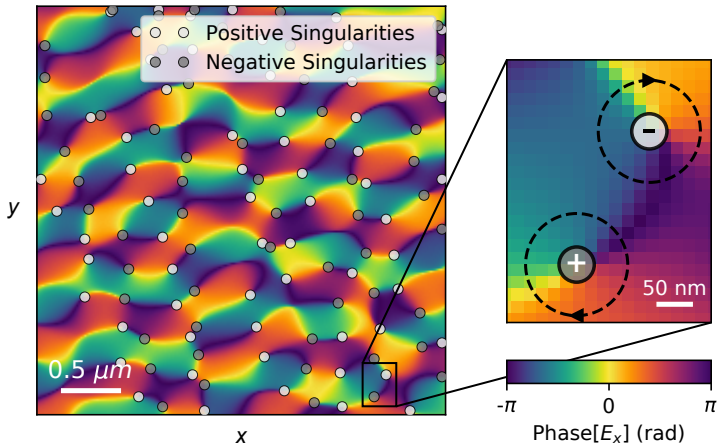

Figure 3.2: False-color map of the measured phase of E_x. The circles indicate the location of the phase singularities, with their topological charge: $q = +1$ (light gray) or $q = -1$ (dark gray). The zoomed-in image highlights how the direction of the circulation of the phase around the singular point determines its topological charge. The x and y axes are indicated in the main plot.

The distribution of optical vortices in the plane is rather disordered (Fig. 3.2), although already by eye a spatial correlation seems discernible, especially if taking into account the topological charge. In order to unveil such correlation, a good quantitative description of the spatial distribution of the ensenble of singularities is needed, which will be the main topic of the following section.

3.3. SPATIAL CORRELATION OF PHASE SINGULARITIES

3.3.1. PAIR AND CHARGE CORRELATION FUNCTION

The natural way to describe the spatial distribution of an ensemble of discrete entities, is to calculate their *pair correlation function*

$$g(r) = \frac{1}{N\rho}\langle \sum_{i\neq j} \delta(r - |\mathbf{r}_j - \mathbf{r}_i|)\rangle, \tag{3.2}$$

where N is the total number of singularities, ρ is the average density of surrounding singularities and δ the Dirac function. This function is directly related to the probability of finding two entities ($\mathbf{r}_i$ and $\mathbf{r}_j$) at a distance r from each other and is widely used in physics to describe discrete systems of various kinds [105].

Figure 3.3 presents the $g(r)$ calculated from our experimental data, specifically for the full data set of singularities of E_x [1]. The shape of the distribution function is highly similar to what is typically observed for a system of particles in a liquid [105]. After an initial dip, $g(r)$ oscillates around one, with an amplitude that decreases as r is increased. The first peak, representative of a surplus of singularities, emerges at a distance of roughly half a wavelength. The decrease in amplitude of the oscillations describes the loss of correlation of the system. However, one peculiarity that we observe is definitely different compared to the case of a liquid: $g(r)$ approaches a finite value for $r \approx 0$. This means that asymptotically there is a finite probability of finding two vortices at the

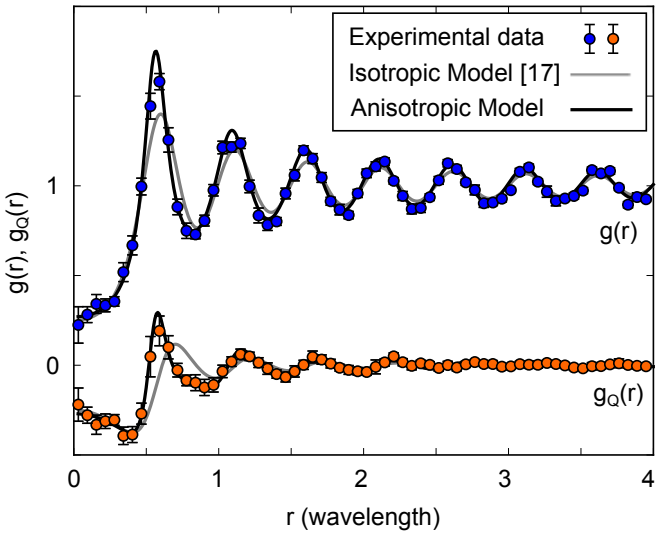

Figure 3.3: Pair (blue) and Charge (orange) correlation function of phase singularities in the measured field E_x. The gray line is the theoretical expectation for a scalar field of isotropic random waves [17]. Our data significantly deviates from such theory, while a perfect agreement is obtained by considering a new model that includes directional anisotropies (black lines).

[1] Similar results are observed for the case of the E_y field.

same location. While unusual this is in fact allowed by the zero-dimensionality of optical vortices.

In analogy to what typically done for ionic liquids [105], it is convenient to introduce a generalized expression of the $g(r)$ for a system of *charged* entities. In the *charge correlation function* $g_Q(r)$ each vortex is weighted with its topological charge q:

$$g_Q(r) = \frac{1}{N\rho}\langle \sum_{i\neq j} \delta(r - |\mathbf{r}_j - \mathbf{r}_i|)\, s_i\, s_j \rangle. \tag{3.3}$$

The experimental result for the $g_Q(r)$ is also reported in Fig. 3.3, providing new information about our system. The main observation here is that $g_Q(r)$ is approximately equal to $-g(r)$ in the region $r \approx 0$, meaning that only singularities with opposite topological charge are likely to be indefinitely close to each other. This behavior is usually interpreted in terms of reciprocal screening among critical points with opposite topological charge [41, 106]. Notably, critical-point screening is related to the reduction of topological charge fluctuations inside a finite region with respect to the prediction for a collection of random charges [17, 41, 107]. A more extensive discussion on this topic will be the focus of Chapter 4.

3.3.2. VECTOR WAVES *vs.* SCALAR WAVES: ANISOTROPY

In an influential paper [17] Berry and Dennis calculated the correlation functions of singularities in a scalar random wave field ψ. This field was modeled as a superposition of plane waves with the same momentum and random phases $\delta_{\mathbf{k}}$, i.e.,

$$\psi(\mathbf{r}) = \sum_{\mathbf{k}} a_k \exp(i\mathbf{k}\cdot\mathbf{r} + i\delta_{\mathbf{k}}). \tag{3.4}$$

The model assumes that the waves amplitudes are isotropically distributed along a circle of radius k_0 in Fourier space. The results of this isotropic model are shown as solid gray lines in Fig. 3.3. Most of the key features of the experimental distribution are qualitatively accounted for by the model, but we clearly observe some deviation from the theory. The biggest difference is in the $g_Q(r)$, where the first peak turns out to be narrower than in theory, as well as significantly shifted towards lower distances. This is in contrast with what was observed for out-of-plane fields in microwaves billiards [102], where excellent agreement was found.

The origin of the observed discrepancies with respect to $g(r)$ and $g_Q(r)$ lies in the vector nature of the light. For the TE modes a direct relation exists between the selected in-plane field component and the direction of propagation: the modes will have no electric field component along the direction of propagation. Therefore the choice of field component to be investigated (e.g. E_x in Fig. 3.2) affects the distribution of propagation directions that contribute to the wave pattern. Whereas the general model in Eq. (3.4) remains valid, the anisotropy of our system violates the assumption of isotropy [17], i.e., that a_k only depends on the magnitude of $\mathbf{k}$. As a consequence, the field correlation function must display an additional dependence on the relative spatial orientation of the points.

3.3.3. ADJUSTED MODEL FOR ANISOTROPIC PROPAGATION

We now calculate the correlation properties of the in-plane components of the field and the corresponding singularities distributions. We do this by including the discussed anisotropy in a modified version of the original model. For a TE mode, the electric field is perpendicular to the wave propagation direction: $\mathbf{E}(\mathbf{k}) \perp \mathbf{k}$. As a consequence, the Fourier coefficients of the in-plane field components are effectively modulated by the sine of the angle $\theta_{\mathbf{k}}$ enclosed by the direction of the considered field component and the in-plane wavevector $\mathbf{k}$. Therefore, we can write

$$E_j(\mathbf{r}) \propto \sum_{\mathbf{k}} \sin(\theta_{\mathbf{k}}) \exp(i\mathbf{k}\cdot\mathbf{r} + i\delta_{\mathbf{k}}), \quad j = x, y. \tag{3.5}$$

Note that the total intensity, $E_x^2 + E_y^2$ remains isotropic.

The additional angular dependence in the Fourier expansion of Eq. (3.5) influences the correlation properties of the wave field. In particular, the spatial autocorrelation function of each field component,

$$C(\mathbf{r}) = \int d\mathbf{r}'\, E_j^*(\mathbf{r}') E_j(\mathbf{r}'+\mathbf{r}) = \frac{1}{2\pi} \int d\mathbf{k}\, \left|E_j(\mathbf{k})\right|^2 e^{-i\mathbf{k}\cdot\mathbf{r}}, \tag{3.6}$$

exhibits a dependence on the orientation φ of vector $\mathbf{r}$:

$$\begin{aligned} C(\mathbf{r}) \doteq C(r,\varphi) = & \quad \frac{1}{2\pi} \int d\theta_{\mathbf{k}} \sin^2(\theta_{\mathbf{k}}) e^{-ik_0 r\cos(\theta_{\mathbf{k}}-\varphi)} \\ = & \quad \frac{1}{2}\left[J_0(k_0 r) + \cos(2\varphi) J_2(k_0 r)\right], \end{aligned} \tag{3.7}$$

where $J_n(x)$ is the Bessel function of order n and k_0 is the wavenumber of the TE mode. This is in contrast with the case of a fully isotropic scalar field, where $C(\mathbf{r}) = J_0(k_0 r)$ [17]. The autocorrelation function of the field contains all the information needed to retrieve pair and charge correlation functions of the phase singularities (see Section 3.5.1 for more details). Analogously to $C(r,\varphi)$, the pair and charge correlation functions $g^{(\mathrm{an})}(r,\varphi)$ and $g_Q^{(\mathrm{an})}(r,\varphi)$ display a dependence on the spatial vector orientation φ. Since in the corresponding experimental quantities in Eqs. (3.2) and (3.3) the average is taken over all reciprocal orientations of the points, to compare the experimental data with the theoretical results, we average the latter over the polar angle:

$$g_Q^{(\mathrm{an})}(r) = \frac{1}{2\pi} \int_0^{2\pi} d\varphi\, g_Q^{(\mathrm{an})}(r,\varphi) \tag{3.8}$$

[and similarly for $g^{(\mathrm{an})}(\mathbf{r})$]. The black solid lines in Fig. 3.3 show the analytic outcome of such calculations (Anisotropic Model). A comparison between experiment and the new model exhibits now an excellent agreement, both qualitative and quantitative. This confirms that the anisotropy in the direction distribution of random waves, intrinsic in the vector nature of optical wave fields, significantly affects the spatial distribution of phase singularities.

3.3.4. ANGULAR DEPENDENCE OF THE CHARGE CORRELATION FUNCTION

A further confirmation of the validity of our model comes from restricting the orientation of the spatial displacement vector **r** to a limited range of values ($\Delta\varphi = \pi/4$) around the directions perpendicular ($\perp$) and parallel ($\parallel$) to the field projection axis. In Fig. 3.4, we compare the results for both the experimentally calculated $g_Q(\mathbf{r})$ and the restricted averages of Eq. (3.8) (Anisotropic Model). The two direction-dependent distribution functions show a completely different behavior. Neither of them is equal to the isotropic $g_Q(r)$ of Ref. [17], which, of course, does not display any orientation dependence. Several differences can be spotted between $g_Q^{\parallel}$ and $g_Q^{\perp}$. First, $g_Q^{\perp}(r)$ vanishes as r approaches

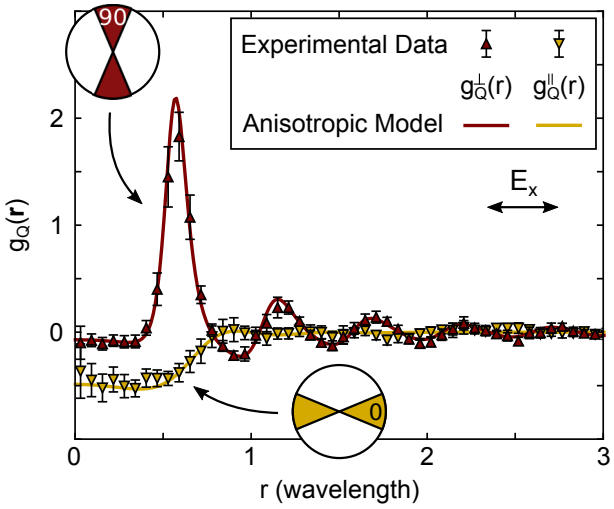

Figure 3.4: Directional charge correlation function. We repoort the two illustrative cases of direction perpendicular (red) or parallel (yellow) to the direction of the considered field component (E_x). The distribution function strongly depends on the direction in the plane. Experimental data is represented by the triangles, while lines show our modified model for anisotropic random waves, which perfectly fits the data.

zero, while $g_Q^{\parallel}(r)$ does not. As a consequence singularities of opposite sign are most likely to be arbitrarily close along the polarization direction. Secondly, in the $g_Q^{\perp}(r)$ there is an evident and positive peak, followed by a number of clear peaks with decreasing height. This trend indicates sequences of same-sign singularities spaced by approximately half a wavelength along the direction perpendicular to the polarization (see also Fig. 3.2). Here, the loss of spatial correlation is slow compared to the direction parallel to the polarization, along which any correlation structure is immediately lost after the initial dip in the $g_Q^{\parallel}(r \approx 0)$.

3.3.5. THE CASE OF A TRULY SCALAR FIELD

It is clear that the vector nature of the optical electric field impacts the spatial distribution of phase singularities. Interestingly, an out-of-plane field component would give us access to a quantity that behaves like a scalar. By Fourier transforming the measured complex fields E_x and E_y, we can calculate the wave-vector space distribution of the

magnetic field $\mathbf{H} \propto \mathbf{k} \times \mathbf{E}$. Fourier transforming back, we can thus construct a spatial map of H_z (up to a constant) [108], in which we identify singularities and perform the same statistical analysis done for E_x and E_y.

The inset in Fig. 3.5 shows the amplitude of $H_z(\mathbf{r})$ as constructed from our measured data. No anisotropy is evident in the resulting amplitude map, in contrast to what we observed for the constituent fields E_x and E_y. Figure 3.5 presents the distribution functions $g(r)$ and $g_Q(r)$ for the phase singularities in H_z together with the theoretical model for isotropic random waves [17]. The agreement is in this case excellent. The direction-dependent distribution functions (not shown) do not exhibit any anisotropy.

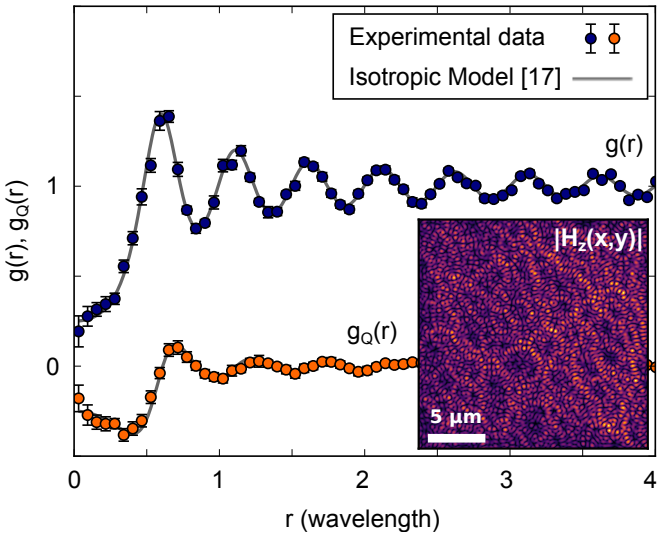

Figure 3.5: Pair and charge correlation function of phase singularities in the constructed out-of-plane magnetic field $H_z(x, y)$. The distribution functions for singularities in this scalar field are in perfect agreement with the model for isotropic random waves [17]. In the inset an amplitude map of $H_z(x, y)$ (a.u.).

3.4. CONCLUSIONS

When considering phase singularities in optical fields, one needs to take into account that light is in general described as a vector wave. We studied the case in which the Cartesian components of an optical random field are considered as separate complex fields. We noticed how considering each field component goes hand in hand with anisotropies in the distribution of propagation direction of random waves. This leads to significant consequences for the spatial distribution of optical vortices. As discussed when analyzing experimental results supported by analytical model, the differences become particularly dramatic when considering the angular dependence of the distribution. We stress that the anisotropic behavior that we analyzed in this chapter is a consequence of the vector nature of light and it is not related to the shape or dielectric constituents of the optical cavity that we used. For this reason, we believe that similar phenomena should arise every time that a truly vectorial electromagnetic field is projected along one of its components.

3.5. SUPPLEMENTARY INFORMATION

3.5.1. SINGULARITY DENSITY AND CORRELATIONS

The following treatment applies to both E_x and E_y; for this reason, even if the variables ξ and η depend on the projection, we omit the x and y subscripts. This choice also avoids a potential notation conflict with Ref. [17], where the same subscripts are used to indicate derivatives. Following the notation of the same Ref. [17], we also define the vorticity associated with the field as $\omega = \partial_x\xi\,\partial_y\eta - \partial_y\xi\,\partial_x\eta$. The charge of phase singularities depends on the local sign of the vorticity.

Given two points $\mathbf{r}_A$ and $\mathbf{r}_B$ in the plane, the density of singularities per unit area, d_2, the pair correlation function, $g(\mathbf{r})$, and the charge correlation function of singularities, $g_Q(\mathbf{r})$, are defined as follows [17]:

$$d_2 = \langle \delta(\xi)\delta(\eta)|\omega|\rangle, \tag{3.9}$$

$$g(\mathbf{r}) = \frac{1}{d_2^2}\langle \delta(\xi_A)\delta(\eta_A)\delta(\xi_B)\delta(\eta_B)|\omega_A||\omega_B|\rangle, \tag{3.10}$$

$$g_Q(\mathbf{r}) = \frac{1}{d_2^2}\langle \delta(\xi_A)\delta(\eta_A)\delta(\xi_B)\delta(\eta_B)\omega_A\omega_B\rangle, \tag{3.11}$$

where $\mathbf{r} = \mathbf{r}_B - \mathbf{r}_A$, $\langle\bullet\rangle$ indicates the average over a statistical ensemble, and we use the compact notation $\xi_A = \xi(\mathbf{r}_A)$, $\xi_B = \xi(\mathbf{r}_B)$, and similarly for η and ω.

In the following, we summarize how the expressions for the quantities in Eqs. (3.9)–(3.11) can be generalized to account for the anisotropy in the Fourier-space distribution of the field components. Starting with the singularity density, we assume that the real and imaginary parts of the field component have equal variance, i.e., $\langle\xi^2\rangle = \langle\eta^2\rangle$. The expression for the density can then be recast into the form

$$d_2 = \frac{1}{2\pi\langle\xi^2\rangle}\left\langle \int \frac{\mathrm{d}t}{t^2}\left(1 - \frac{1}{2}e^{i\omega t} - \frac{1}{2}e^{-i\omega t}\right)\right\rangle, \tag{3.12}$$

where the average reduces to a four-dimensional complex Gaussian integral on the variables $\partial_x\xi$, $\partial_y\xi$, $\partial_x\eta$, and $\partial_y\eta$. The integration is carried out straightforwardly and the final result is:

$$d_2 = \frac{1}{2\pi}\frac{\sqrt{\langle(\partial_x\xi)^2\rangle\langle(\partial_y\xi)^2\rangle}}{\langle\xi^2\rangle}. \tag{3.13}$$

The presence of the sine-modulation term in Eq. (3.5) implies that $\langle(\partial_x\xi)^2\rangle \neq \langle(\partial_y\xi)^2\rangle$, at variance with the isotropic scalar field considered in Ref. [17]. On the other hand, it is possible to show that Eq. (3.13) reduces to the result of Ref. [17] in the assumption that $\langle(\partial_x\xi)^2\rangle = \langle(\partial_y\xi)^2\rangle$.

In order to compute the pair correlation function of the singularities, we introduce the six-dimensional vector

$$\begin{aligned}\mathbf{u} = &\left[\xi(\mathbf{r}_A), \xi(\mathbf{r}_B), \partial_x\xi(\mathbf{r}_A), \partial_x\xi(\mathbf{r}_B), \partial_y\xi(\mathbf{r}_A), \partial_y\xi(\mathbf{r}_B)\right] \\ \doteq &\left[\xi_A, \xi_B, \partial_x\xi_A, \partial_x\xi_B, \partial_y\xi_A, \partial_y\xi_B\right]\end{aligned} \tag{3.14}$$

and the corresponding matrix of correlations

$$\mathbb{M}_{ij} = \langle u_i u_j \rangle. \tag{3.15}$$

As detailed in Ref. [17], the elements of the matrix are obtained from the autocorrelation function $C(\mathbf{r}_B - \mathbf{r}_A) = \langle \xi_A \xi_B \rangle = \langle \eta_A \eta_B \rangle$ and its partial derivatives:

$$\langle \xi_A \partial_\alpha \xi_B \rangle = -\langle \partial_\alpha \xi_A \xi_B \rangle = \partial_\alpha C(\mathbf{r}) \quad \text{and} \quad \langle \partial_\alpha \xi_A \partial_\beta \xi_B \rangle = -\partial_\alpha \partial_\beta C(\mathbf{r}), \tag{3.16}$$

where $\mathbf{r} = \mathbf{r}_B - \mathbf{r}_A$ and $\alpha, \beta = x, y$. The expressions for $C(\mathbf{r})$ in the isotropic and anisotropic cases are discussed in the main text. In addition to the different expressions of the autocorrelation function, there is an important difference between the isotropic and anisotropic cases. In the former case, several assumptions based on isotropy considerations allow to simplify and write in block form the correlation matrix. This is the approach described in Ref. [17]. In the anisotropic case, such assumptions are no longer valid and the derivation of the pair correlation function must be generalized to retain the full correlation matrix at any stage, as we sketch in the following.

According to Eq. (4.33) of Ref. [17], the pair correlation function is expressed as an integral of the characteristic function

$$T(t_A, t_B) = \langle \delta(\xi_A)\delta(\eta_A)\delta(\xi_B)\delta(\eta_B) \exp(i\omega_A t_A - i\omega_B t_B) \rangle. \tag{3.17}$$

In our generalized derivation, we write the characteristic function as the eight-dimensional complex Gaussian integral

$$T(t_A, t_B) = \frac{1}{(2\pi)^6 \det \mathbb{M}} \int \mathrm{d}^8\mathbf{w} \, \exp(-\tfrac{1}{2}\mathbf{w}^T \mathbb{U} \mathbf{w}), \tag{3.18}$$

with the block matrix

$$\mathbb{U} = \begin{bmatrix} \mathbb{N} & i\mathbb{A} \\ i\mathbb{A}^T & \mathbb{N} \end{bmatrix}. \tag{3.19}$$

In the latter equation, matrix $\mathbb{N}$ is obtained from $\mathbb{M}^{-1}$ by removing the first two rows and two columns (this results from the integration of the δ-terms); on the other hand, matrix $\mathbb{A}$ is defined as follows:

$$\mathbb{A} = \begin{bmatrix} 0 & 0 & -t_A & 0 \\ 0 & 0 & 0 & t_B \\ t_A & 0 & 0 & 0 \\ 0 & -t_B & 0 & 0 \end{bmatrix}. \tag{3.20}$$

The Gaussian integral can be carried out with standard techniques and, after some algebraic manipulations, the characteristic function becomes ($\mathbb{1}$ denotes the 4×4 identity matrix)

$$T(t_A, t_B) = 1 \Big/ \left[4\pi^2 \det \mathbb{M} \det \mathbb{N} \sqrt{\det(\mathbb{1} + \mathbb{N}^{-1}\mathbb{A}) \det(\mathbb{1} - \mathbb{N}^{-1}\mathbb{A})} \right]. \tag{3.21}$$

The determinant of $\mathbb{1} + \mathbb{N}^{-1}\mathbb{A}$ is a quartic polynomial in the variables t_A and t_B. In particular, since both $\mathbb{N}^{-1}$ and the cofactor matrix of $\mathbb{N}^{-1}$ are symmetric, it can be shown

that the polynomial contains only even-degree terms. As a further consequence, we observe that $\det(\mathbb{1}+\mathbb{N}^{-1}\mathbb{A}) = \det(\mathbb{1}-\mathbb{N}^{-1}\mathbb{A})$. After explicitly calculating the determinant and rearranging the terms, the correlation function can be written in the form

$$g(\mathbf{r}) = \frac{\Xi^{1/2}}{4\pi^4 d_2^2 \det\mathbb{M}\det\mathbb{N}} \int \frac{\mathrm{d}t_A}{t_A^2}\frac{\mathrm{d}t_B}{t_B^2} I(t_A, t_B, Y, Z), \tag{3.22}$$

with the same integration kernel $I(t_A, t_B, Y, Z)$ defined in Eq. (4.45) of Ref. [17], albeit with a generalized definition of the parameters Y and Z:

$$Y = [\mathbb{N}_{14}^{-1}\mathbb{N}_{23}^{-1} - \mathbb{N}_{12}^{-1}\mathbb{N}_{34}^{-1}]^2/\Xi; \tag{3.23}$$

$$Z = \det\mathbb{N}^{-1}/\Xi; \tag{3.24}$$

$$\Xi = [\mathbb{N}_{33}^{-1}\mathbb{N}_{11}^{-1} - (\mathbb{N}_{13}^{-1})^2][\mathbb{N}_{44}^{-1}\mathbb{N}_{22}^{-1} - (\mathbb{N}_{24}^{-1})^2]. \tag{3.25}$$

Eventually, the t_A integral is carried out as described in Ref. [17], to give the final result

$$g(\mathbf{r}) = \frac{\Xi^{1/2}}{2\pi^3 d_2^2 \det\mathbb{M}\det\mathbb{N}} \int \mathrm{d}t\, \frac{3 - Z + 2Y + (3 + Z - 2Y)t^2 + 2Zt^4}{(1+t^2)^3\sqrt{1 + (1 + Z - Y)t^2 + Zt^4}}, \tag{3.26}$$

which can be easily evaluated by numerical means.

The last quantity under consideration, the sign correlation function of Eq. (3.11), can be computed directly from the characteristic function:

$$g_Q(\mathbf{r}) = \frac{1}{d_2^2}\frac{\partial}{\partial t_A}\frac{\partial}{\partial t_B} T(t_A, t_B)\Big|_{\substack{t_A=0\\t_B=0}} = \frac{\mathbb{N}_{12}^{-1}\mathbb{N}_{34}^{-1} - \mathbb{N}_{14}^{-1}\mathbb{N}_{23}^{-1}}{2\pi^2 d_2^2 \det\mathbb{M}\det\mathbb{N}}. \tag{3.27}$$

4

SCREENING AND FLUCTUATIONS OF THE TOPOLOGICAL CHARGE IN RANDOM WAVES

Nothing exists;
Even if something exists, it cannot be known;
Even if something could be known, it cannot be communicated to others.

[5]Gorgias

Vortices, phase singularities and topological defects of any kind often reflect information that is crucial to understand physical systems in which such entities arise. With near-field experiments supported by numerical calculations, we determine the fluctuations of the topological charge for phase singularities in isotropic random waves, as a function of the size R of the observation window. We demonstrate that for 2D fields such fluctuations increase with a super-linear scaling law, proportional to $R\log R$. Additionally, we show that such scaling remains valid in presence of anisotropy.

Parts of this chapter have been published in Optics Letters **43**, 2740-2743 (2018) [109].

4.1. INTRODUCTION

An accurate knowledge on the statistical fluctuations of a given physical observable is often essential, with an importance on par with the ensemble-averaged value of the observable itself [110]. In fact, fluctuations are ubiquitous in quantum as well as in classical physics. A prime example is the grand canonical ensemble in statistical physics, where the number of particles is only known in average, and its fluctuations have an actual physical meaning, directly linked to the chemical potential of the system [111]. Ensembles of this type are offered by many systems in physics, for example whenever they exhibit topological defects [112, 113], which in the context of optics can be optical singularities [7]. These singularities are point-like entities carrying a topological charge and in random waves they are reminiscent of interacting particles [87]. Oppositely charged pairs can be created and destroyed [53], resulting in a total number of singularities which is not conserved. Although the total topological charge of an ensemble of singularities is always conserved [114], this number can still vary when considering a finite observation window, and its fluctuations are the hallmark for intrinsic properties of the system, such as charge screening [107].

Here we study quantitatively the fluctuations of the total topological charge for phase singularities in random waves and determine the dependence of such fluctuations on the size of the observation window. With near-field experiments we map the optical near-field inside a chaotic cavity [87]. By tuning the excitation wavelength we measure different realizations of the optical random wave pattern inside the cavity [115]. Such phase- and polarization-resolved measurements enable us to pinpoint position and topological charge of the individual phase singularities in all in-plane components of the electric field that we measure, and therefore determine and investigate their total topological charge and its fluctuations. With experimental evidence, corroborated by numerical calculations, we demonstrate that the sum of the topological charges contained in a square region of area R^2 fluctuates as $R \log R$, in agreement with analytical calculations [107].

4.2. EXPERIMENTAL

While our measurements provide access to the two-dimensional random vector field, previous theoretical results on topological screening examined the case of scalar waves [107]. With this regard, it is important to note that our complete information on the in-plane field $\mathbf{E}$ allows us to reconstruct an out-of-plane component $H_z \propto \mathbf{k} \times \mathbf{E}$, which behaves fully as a scalar field (see also Section 3.3.5). Following well established models for random wave fields [28], we can think of H_z as an isotropic superposition of plane waves interfering with random phases $\phi_{\mathbf{k}}$ [17],

$$H_z = \sum_{|\mathbf{k}|=k_0} \exp(i\mathbf{k}\cdot\mathbf{r} + i\phi_{\mathbf{k}}), \tag{4.1}$$

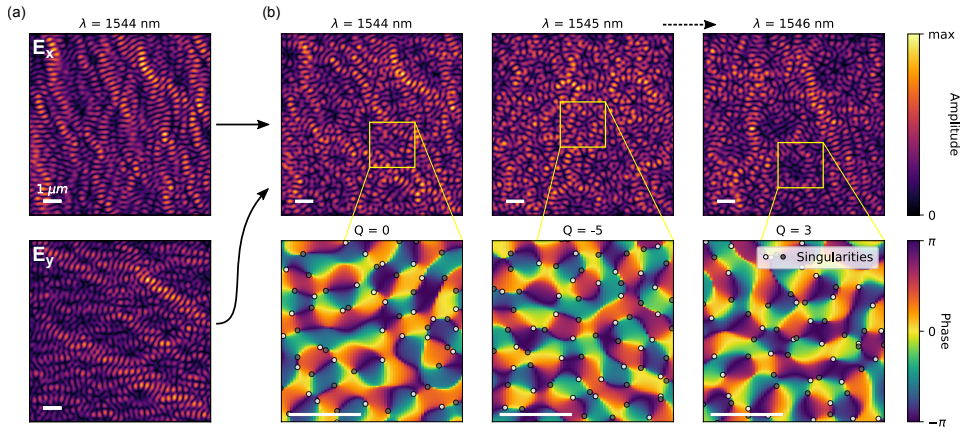

Figure 4.1: Overview of the near-field measurements of the optical field inside the chaotic cavity. (a) Optical micrograph of the cavity used for the generation of the optical random wave field. The dark area is the photonic crystal that confines light inside the cavity. (b) Example of a direct measurement of the in-plane components of the optical random field under investigation. In the upper panel the amplitude of E_x and in the lower pane the amplitude of E_y. (c) Near-field maps of $H_z \propto \mathbf{k} \times \mathbf{E}$. In the upper panels the amplitude of H_z for different excitation wavelength λ, and in the lower panels zoomed-in images of its phase. Phase singularities of positive and negative topological charge are depicted by light-gray and dark-gray circles, respectively.

which is characterized by an autocorrelation

$$C(r) = \int d\mathbf{r}' H_z(\mathbf{r}') H_z(\mathbf{r}+\mathbf{r}') = J_0(kr), \tag{4.2}$$

where $J_0(kr)$ is the Bessel function of order 0.

Figure 4.1 presents a direct measurement of the amplitude of the in-plane field components (E_x, E_y), as well as amplitude and phase of H_z, as obtained from measurements at different excitation wavelengths. From the subwavelength maps of the amplitude we can clearly resolve the interference that results in a speckle-like pattern [116]. Figure 4.1 also displays zoomed-in images for the phase of H_z. Here, the circles indicate the location of phase singularities with their topological charge (color), i.e., the integer number of times that the phase of the field loops from $-\pi$ to π around the singular point (see Section 3.2.2 singularities pinpointing). We always observe the topological charge to be equal to ± 1 (dark/light gray) [7]. The patterns presented in Fig. 4.1 change dramatically with the input wavelength. A wavelength shift of 1 nm already leads to a totally different field configuration. In fact, the spectral correlation width of this random field is of the order of 0.2 nm, as we quantify by computing the wavelength-wavelength correlation of H_z (more details in Chapter 5).

Although the wave field is made up by randomly interfering waves, the distribution of the singularities does contain structure. In fact, as extensively discussed in Chapter 3, the distribution of phase singularities in random waves has a liquid-like correlation. An immediate question that arises at this point, is whether the charges of such distribution of singularities are correlated or not, and, if so, how. In a system of charged particles we would expect such correlation to occur due to charge screening. While it is tempting to

make an analogy straight away, and predict a screening among topological charges, we must remember that the nature of phase singularities is radically different from that of atoms and molecules, and there is no true and measurable physical interaction among these entities. A straightforward analogy between charged particles and singularities with their topological charge is therefore not so trivial.

4.3. SCREENING OF PHASE SINGULARITIES IN RANDOM WAVES

4.3.1. CHARGE SCREENING AND TOPOLOGICAL SCREENING

The easiest test that can be performed to determine the existence of charge screening, is to measure the overall topological charge $Q = \sum_i q_i$ of the singularities q_i contained in an area of dimension $A = R^2$. In complete absence of charge correlation one expects the average $\langle Q \rangle$ of such quantity to be zero, and its variance $\langle Q^2 \rangle$ to scale with the area of the observation window R^2 [107]. A screening among charges would reveal itself by slowing down the dependence of such variance to a sub-quadratic law. In fact, screening neutralizes charges by surrounding them with a cloud of opposite charges, so to prevent fluctuations of the total charge inside an area $\sim R^2$, in favor of fluctuations along the perimeter region $\sim R$ [117]. The existence of screening among topological charges is well established in literature. [41, 106, 107, 117–122]. It starts to play a role when the size of the observation window is bigger than the typical inter-singularity distance, of approximately $\lambda/2$. However, how much this screening slows down the quadratic law $\langle Q^2(R) \rangle \propto R^2$ is yet unclear. Explicitly, a first model of $\langle Q^2(R) \rangle$, in which two assumptions were made on the autocorrelation of the random field, predicted linear scaling [41], whereas further theory developments proved such quantity to scale as $R \log R$ [107]. More recently, also paraxial experiments were performed, supporting the linear dependence [106, 117, 121].

4.3.2. RESULTS

Figure 4.2 presents our results for $\langle Q^2(R) \rangle$. In the main plots the analysis of screening for $R \geq \lambda/2$, in the inset a proof of its absence in the region $R < \lambda/2$. In the left panel we present the experimental data, which is the result of the sampling of 200 experimental scalar field realizations where we randomly pick the position of our observation window. The fields are obtained by varying the excitation wavelength λ over a range $\Delta\lambda = 20\,\text{nm}$ around $\lambda_0 = 1550\,\text{nm}$. In the right panel we show simulation data, realized by sampling 3500 random wave fields which were independently calculated by adding up 250 plane waves with isotropic directions and random phases [(4.1)]. In both cases, we obtain a good agreement only with the $R \log R$ dependence. A quadratic fit cR^2 is clearly inadequate for the data displayed in the main plot. However, this functional behavior perfectly describes the short-distance data in the insets of Fig. 4.2, at which range screening is indeed absent. Less evident, but still significant, is the inconsistency between the data and a linear behavior. Although this is more eye-catching in the region $R/\lambda > 5$, a clear deviation is still present for $R/\lambda < 3$, with even greater significance considering the small errorbars associated with the latter region.

More quantitatively, we fitted our data with $f_1(R) = mR$ (gray lines in Fig. 4.2), and $f_2(R) = a\,bR \log bR$ (red lines in Fig. 4.2). We focus on how well these functions can de-

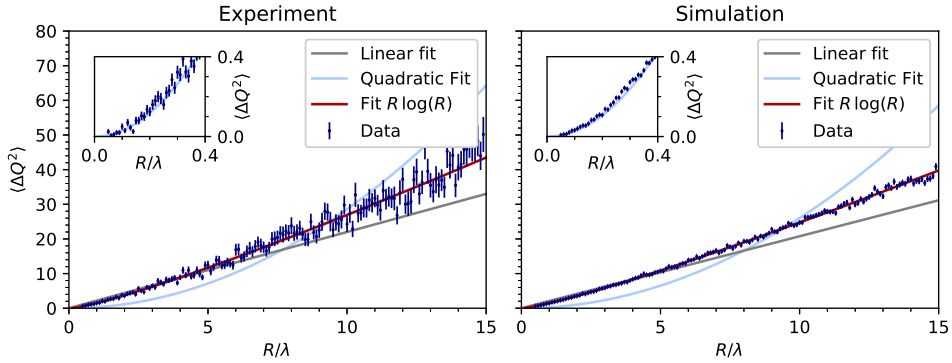

Figure 4.2: Fluctuation of topological charge $\langle \Delta Q^2 \rangle$ as a function of the size R of the observation area R^2, for the experimental scalar field H_z (a) and for a simulated isotropic scalar field (b). The blue errorbars are the respective data points. The gray lines are the best fit with $f_1 = mR$ [$m_{exp} = 2.20(5)$; $m_{sim} = 2.08(4)$]. The red lines are the best fit with $f_2 = a\,bR\log bR$ [$a_{exp} = 0.026(5)$, $b_{exp} = 19(3)$; $a_{sim} = 0.0144(1)$, $b_{sim} = 30(2)$]. The light blue lines are the best fit with $f_3 = cR^2$ [$c_{exp} = 0.286(11)$; $c_{sim} = 0.260(11)$].

scribe our data rather than on the resulting fit parameters, which we found to depend on the shape of the chosen observation window (not shown). We quantified the goodness of such least-square fits by performing a χ^2 test, the results of which are summarized in Table 4.1. In both experiment and simulation we are performing the fit on 145 equally spaced data points, resulting in 144 degrees of freedom (DOF) for the linear fit (1 free parameter) and in 143 DOF for f_2 (2 free parameters). The χ^2 is a stochastic variable, with expectation value equal to the DOF [123]. The values of the χ^2 for the fittings with $f_2(R)$ are consistent with their expectation value, whereas the case of f_1 leads to χ^2 values that are too high to be mere statistical fluctuations. After this quantitative analysis of our fits we can most certainly conclude that the $R\log R$ scaling law is describing the behavior of $\langle Q^2(R)\rangle$ better than a linear function.

Fit function	$\chi^2{}_{exp}$	$\chi^2{}_{sim}$	DOF
$f_1(R) = mR$	954	10^4	144
$f_2(R) = a\,bR\log bR$	125	147	143

Table 4.1: Summary of the χ^2 tests for the least-square fits presented in Fig. 4.2 (isotropic case). From left to right: fit function, sum of the residuals for the experimental case, sum of the residuals for the simualtion, and number of degrees of freedom.

Certainly, the studied cases are not exhaustive of all the possible functional behaviors one could think of. For instance, an alternative trade-off between the linear and quadratic scalings could be given by a generic power law βR^α. Interestingly, such a function can be effectively used to fit both experimental and simulated data, with $\alpha \approx 1.2$. However, the result of such fits (not shown) are found to be less reliable, since they lead to different optimal fit parameters when varying fitting range. In the absence of existing theories, they remain difficult to interpret.

4.4. SCREENING IN THE PRESENCE OF ANISOTROPY

Going back to screening and its nature, we now investigate its functioning in presence of anisotropy. In fact, in case of anisotropic wave propagation also the spatial arrangement of phase singularities becomes anisotropic [87], and it does not resemble the distribution of a simple liquid anymore. Actually, along particular directions the resulting distribution is more reminiscent of an ordered structure. Thus, it is interesting to check whether or not this anisotropy influences the topological screening here discussed.

Anisotropic wave propagation naturally takes place in the single vector components of the measured in-plane electric field. This is caused by the strict relation between polarization and propagation direction set by transverse electric propagation [87]. Figure 4.1(b) presents an example of our direct measurement of amplitude E_x and E_y inside the chaotic cavity. By comparing this figures to the maps for the scalar field H_z presented in Fig. 4.1(c), we can see a pronounced anisotropy. For example, in the amplitude map of E_x we easily distinguish a stripy pattern, given by a fast modulation of the amplitude along the y-axis, opposed to a modulation along the x-axis which is slower by at least a factor two. This anisotropy results in a spatial arrangement of dislocations where many singularities with the same topological charge are displaced along the y-axis, while the first neighbor in the x-direction is often oppositely charged [87].

Figure 4.3 presents the fluctuation of topological charge $\langle \Delta Q^2 \rangle$ for the case of E_x, in both experiment and simulation. The analysis of its behavior is carried in complete analogy to what already described for H_z. Again, we can conclude that the scaling law given by $R \log R$ is more successful than a linear function [$\chi^2_{exp}(mR) = 2098$, whereas $\chi^2_{exp}(a\,bR \log bR) = 187$]. However, we do observe that the growth rate of $\langle \Delta Q^2 \rangle$ is faster than in the case of the scalar field H_z (Fig. 4.2). This suggests that an anisotropic distribution of topological charges results in a screening that on average is less effective with respect to its isotropic counterpart. This of course only holds when considering the average over all the possible directions along which singularities are displaced, whereas it is very likely for this form of screening to strongly depend on the considered direction. Still, considering these qualitative differences with the isotropic scalar case, it is remarkable how the $R \log R$ law can still describe the data.

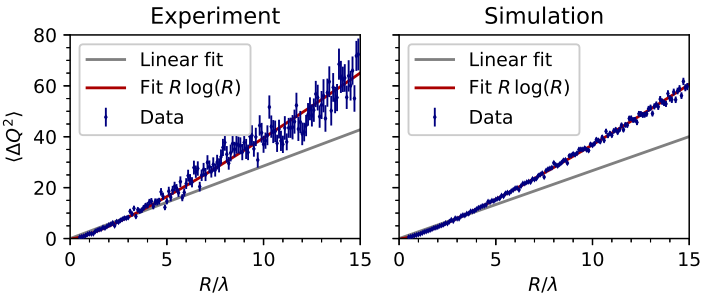

Figure 4.3: Fluctuation of the topological charge $\langle \Delta Q^2 \rangle$ vs. R, as in Fig. 4.2. These results are for the anisotropic case of a Cartesian component (E_x) of a trasverse vector field **E**. Gray lines $f_1 = mR$ [$m_{exp} = 2.85(9)$; $m_{sim} = 2.08(4)$]. Red lines $f_2 = a\,bR \log bR$ [$a_{exp} = 0.15(2)$, $b_{exp} = 6.5(5)$; $a_{sim} = 0.126(3)$, $b_{sim} = 6.9(1)$].

4.5. CONCLUSIONS

To conclude, we presented a quantitative study on the screening of topological charges for singularities in random waves. With near-field experiments and numerical calculations we demonstrated that while the average topological charge remains zero independently of the size R of the observation window, the fluctuation of this quantity increases with a dependence which is consistent with a $R \log R$ law. This result validates previous analytical theory [107]. Additionally, we extended our study to the case of anisotropic wave propagation. Even though the nature of screening drastically changes in presence of anisotropy, we showed that the functional dependence of topological charge fluctuations is still well described by the $R \log R$ scaling law.

5

WAVELENGTH-DEPENDENT EVOLUTION OF PHASE SINGULARITIES IN RANDOM WAVES

Theories were clean and convincing and comprehensible.
Life was messy and full of nonsense.

[6]Julian Barnes

Phase singularities are locations where light is twisted like a corkscrew, with positive or negative topological charge, depending on the twisting direction. Among the multitude of singularities arising in random wave fields, some of them can be found at the same location, but only when they exhibit opposite topological charge, which results in their mutual annihilation. New pairs can be created as well. With near-field experiments supported by theory and numerical simulations we study persistence and pairing statistics of phase singularities in random optical fields as a function of the excitation wavelength. We demonstrate how such entities can encrypt fundamental properties of the random fields in which they arise.

Parts of this chapter have been published in Physical Review Letters **119**, 203903 (2017) [115].

5.1. INTRODUCTION

A wide variety of physical systems exhibit vortices: locations around which an observable rotates while being undetermined in the middle [124–132]. It is exceptionally fascinating when the properties and evolution of such singular entities can comprehensively describe complex phenomena such as the Kosterlitz-Thouless transition [133]. But vortices are not a peculiarity of superconductors: light's phase swirls around optical vortices, where it is singular [7]. A multitude of these phase singularities arises in random optical fields, one half swirling in opposite direction to the other, so that they can approach respectively to an arbitrarily small distance [17, 52, 87]. It is by letting them move that one can observe creation and/or annihilation of such pairs [53, 134–136].

With near-field experiments we track phase singularities in a random optical field from *birth* to *death*. We map the singularities' trajectories as a function of the excitation wavelength and quantitatively determine properties such as their persistence in the field and the retention of creation and annihilation partners of a singularity, known as *lifelong fidelity* [137]. We observe two populations of singularities, neatly differentiated by their typical persistence in the varying wave field: short-lived pairs that are predominantly *faithful* to their creation partner, and a more promiscuous population.

5.2. CREATION, EVOLUTION AND ANNIHILATION OF PHASE SINGULARITIES

To study the evolution of singularities, we perform near-field measurements of the optical field in the chaotic cavity while slowly tuning the input wavelength. Figure 5.1 presents a typical example of our measurements of amplitude and phase of E_x. The optical field inside the cavity is a random superposition of light waves [28] with transverse electric (TE) polarization [87]. Only the behavior of E_x is presented here, without loss of generality, as it is representative of the behavior of all in-plane field components [87].

Figure 5.1(b) is a full-size measurement: a square map $17\,\mu m \times 17\,\mu m$ with a pixel size of about 17 nm. In this map we distinguish a multitude of *dark* and *bright* spots, the results of destructive and constructive interference. Figures 5.1(c)-(f) are $2\,\mu m \times 2\,\mu m$ zoom-ins of the full measurements taken at different wavelengths of the input light. Here, we can observe how a small change of the wavelength ($\delta = 0.02$ nm), hardly produces any change in the spatial pattern of the amplitude. Figures 5.1(g)-(j) depict the measured phase, and reveal the phase singularities which take place at every zero in the amplitude (gray circles). We pinpoint the position of these singularities with deep subwavelength resolution (see Section 3.2.2), and simultaneously determine their topological charge, which is always observed to be +1 (light circles) or -1 (dark circles), corresponding to a $\pm 2\pi$ change of the phase around the singular point [114].

In the panels (g)-(j) of Fig. 5.1, we observe that the singularities move as a function of wavelength. More eye-catching than their tiny movements are the annihilation and creation events of pairs of singularities, which can be both observed between the panels (h) and (i) (Fig. 5.1), highlighted by black circles. Indeed, singularities can be created and annihilated, but only in processes that conserve the total topological charge of the system, i.e., in pairs of opposite topological charge. Thus, as we tune the wavelength,

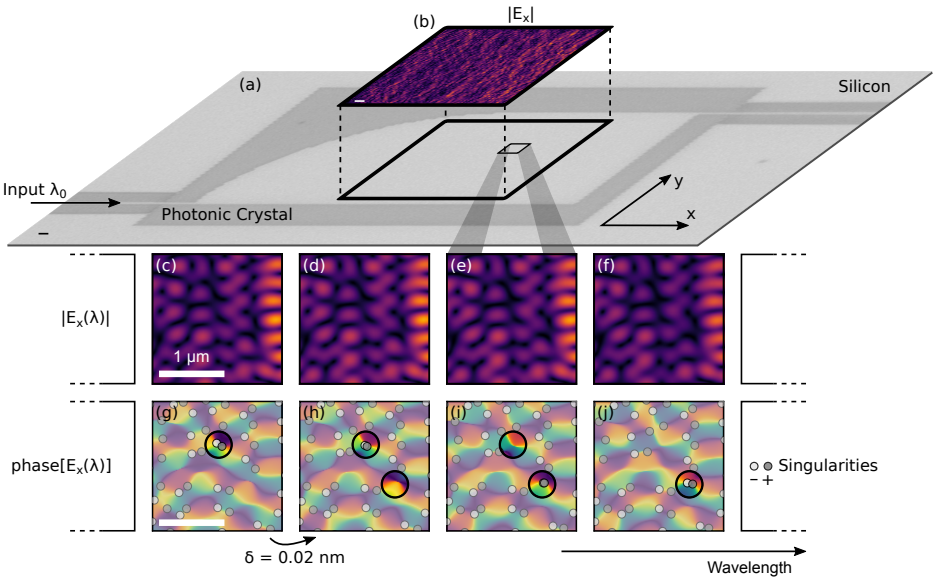

Figure 5.1: Near-field measurements of the optical field in the chaotic cavity. (a) Optical micro-graph of the chaotic cavity: the dark area is a photonic crystal that confines light inside the cavity. (b) 17μm × 17μm near-field map of the amplitude of the x component of the electric field in the cavity. (c-f) Zoom-in of panel b for different input wavelength λ. (g-j) False-color map of the measured phase for different input wavelength λ; in such maps we pinpoint phase singularities with positive (dark spots) or negative (light spots) topological charge. The black circles highlight annihilation and creation events.

singularities exhibit a transitory persistence in the random field over the span of a finite wavelength shift $\Delta\lambda$ between their creation and annihilation. We track the singularities as a function of wavelength shift with a heuristic algorithm based on the vicinity of singularities in two consecutive frames. In particular, singularities existing in the field have two options: propagation or annihilation (creation). Therefore, all the singularities need to be connected to their propagation in the next frame or to their annihilation/creation partner in the same frame. We establish such connection within an error < 1%. A small amount of trajectories is truncated at the edges of the measured map (~ 1%). We simply do not consider this trajectories, with no relevant consequences on our statistics. A significant amount of trajectories is truncated at the beginning and end of our wavelength sweep. We do not consider these trajectories as well, but we need to take this fact into account, as it will be discussed in Section 5.3. In Fig. 5.2 we present a 3D representation of the trajectories followed in space and wavelength by a small subset of all the singularities that we measure. Among all the trajectories, the red ones represent *lifelong faithful* singularities: *special* cases where the singularities have the same partner for both creation and annihilation. In contrast, the green trajectories are *unfaithful* singularities.

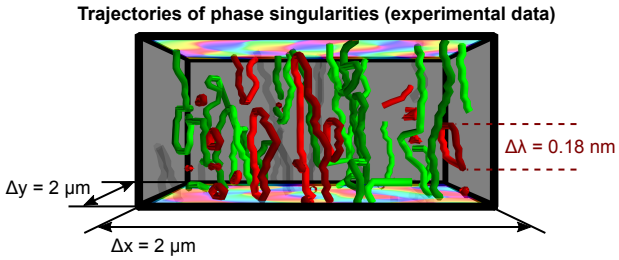

Figure 5.2: 3D representation of the trajectories of singularities that propagate through a 2μm × 2μm × 0.64nm observation volume. The red and green trajectories are of faithful and unfaithful singularities, respectively. In both cases bright and dark colors differentiate oppositely charged singularities. Please note that the parts of the trajectories that continue outside of the observation volume are not shown. The semi-transparent trajectories are of singularities that propagate outside of the total wavelength range: these are not taken into account in our statistics.

5.3. PERSISTENCE AND LIFELONG FIDELITY

5

5.3.1. EXPERIMENTAL OBSERVATIONS

Figure 5.3(a) presents the number $\mathcal{N}$ of singularities as a function of their persistence $\Delta\lambda$ in the measured field. The main plot illustrates the results obtained from a dataset in which we tuned the wavelength with a step $\delta = 0.02\,\text{nm}$ for a total range $\mathscr{L} = 1.2\,\text{nm}$. In such a plot, we distinguish two persistence regimes separated by a cutoff wavelength shift $\lambda^* \approx 0.15\,\text{nm}$. In the region $\Delta\lambda > \lambda^*$, the number of singularities exponentially decays versus their persistence in the field, with a characteristic persistence $\lambda_d = 0.6\,\text{nm}$. Such exponential behavior is even clearer from the the inset, representative of a measurement in which the total range of the wavelength sweep is $\mathscr{L} = 8\,\text{nm}$ ($\delta = 0.1\,\text{nm}$). Please note that the finite size of the wavelength scans has non-negligible effects on the measured statistics, mainly for the longest trajectories, thus slightly distorting the exponential behavior. This is because singularities that are created and/or annihilated outside the measured wavelength range need to be excluded from the persistence statistics. Intuitively, we estimate the fraction of such singularities to be of the order of the ratio $\Delta\lambda/\mathscr{L}$, resulting in a correction factor for $\mathcal{N}(\Delta\lambda)$ proportional to $(1-\Delta\lambda/\mathscr{L})$.

The exponential behavior that we observe could be interpreted in a straightforward way as the result of a memoryless Poisson process. However, we discover a physics richer than that. From the main plot of Fig. 5.3(a) we notice that $\mathcal{N}(\Delta\lambda)$ is not purely exponential: it clearly deviates from such a distribution for $\Delta\lambda$ smaller than λ^*. This spectral region contains an excess of singularities compared to what the asymptotic exponential distribution would predict. Their characteristic persistence in the field is much smaller than λ_d. In fact, by fitting $\mathcal{N}(\Delta\lambda)$ with a bi-exponential distribution, we can estimate the characteristic persistence for such short-living population to be approximately 0.03 nm. Please note that the cutoff wavelength shift λ^* does not depend on the absolute starting wavelength as the trajectories of the singularities in excess are uniformly distributed along the measured wavelength range."

Interestingly, when considering only the *faithful* singularities (the red trajectories in Fig. 5.2), a different behavior is observed than for the full ensemble of all singularities. It

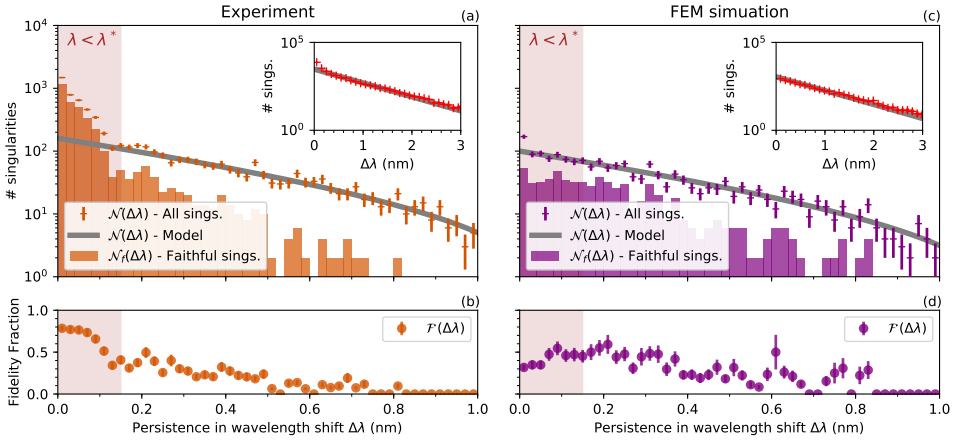

Figure 5.3: Overview of the statistics for the persistence and fidelity of singularities in random waves, in experiment (a,b) and FEM simulation (c,d). In the upper panels the dashes indicate the number of singularities $\mathcal{N}$ which persisted in the field for a given wavelength shift $\Delta\lambda$. The main figures refer to experiment/simulation where the wavelength was sweeped over a range $\mathcal{L} = 1.2\,\text{nm}$ with a step $\delta = 0.02\,\text{nm}$, whereas the insets show the results of wider scans ($\mathcal{L} = 8\,\text{nm}$, $\delta = 0.1\,\text{nm}$). The gray lines are representative of the prediction for the persistence histogram given by our model. In the same panels, the boxes are still a persistence histogram, but in which only the $\mathcal{N}_f$ singularities that were faithful to each other are taken into account. In the lower panels we report the fidelity fraction $\mathcal{F}$ of phase singularities, again as a function of their persistence in the field $[\mathcal{F}(\Delta\lambda) = \mathcal{N}_f(\Delta\lambda)/\mathcal{N}(\Delta\lambda)]$.

is clear from Fig. 5.3(a) that in the region where deviation from a single exponential takes place ($\Delta\lambda < \lambda^*$), we have an over-representation of faithful singularities (yellow boxes). This is reflected explicitly in the fidelity fraction $\mathcal{F}(\Delta\lambda) = \mathcal{N}_f(\Delta\lambda)/\mathcal{N}(\Delta\lambda)$ represented in Fig. 5.3(b): while a majority of the *short-living* singularities is faithful to each other, the opposite is true for *long-living* ones.

5.3.2. WAVELENGTH-WAVELENGTH CORRELATION OF THE FIELD

The origin of the cutoff λ^* which discriminates the population of faithful and short-living singularities from that of unfaithful and long-living ones must be sought in the evolution properties of the field. Figure 5.4 displays the correlation coefficient of the considered experimental field at wavelengths λ_1 and λ_2:

$$\rho(\lambda_1,\lambda_2) = \frac{|\int \mathrm{d}\mathbf{r}\, \tilde{E}_x^*(\lambda_1)\tilde{E}_x(\lambda_2)|}{\sqrt{\int \mathrm{d}\mathbf{r}\,|\tilde{E}_x(\lambda_1)|^2 \int \mathrm{d}\mathbf{r}\,|\tilde{E}_x(\lambda_2)|^2}}, \tag{5.1}$$

where $\tilde{E}_x = E_x - \langle E_x \rangle$. It is interesting to note that the correlation coefficient $\rho(\lambda_1,\lambda_2)$ decays over a finite wavelength shift $\lambda_c \approx \lambda^*$. Such a close relation between λ_c and λ^* may suggest that those singularities which spend their entire existence in the region of spectral correlation of the field exhibit persistence and pairing properties that are different from those of singularities over-living this region.

Although seemingly intuitive, this simple interpretation cannot be the whole story.

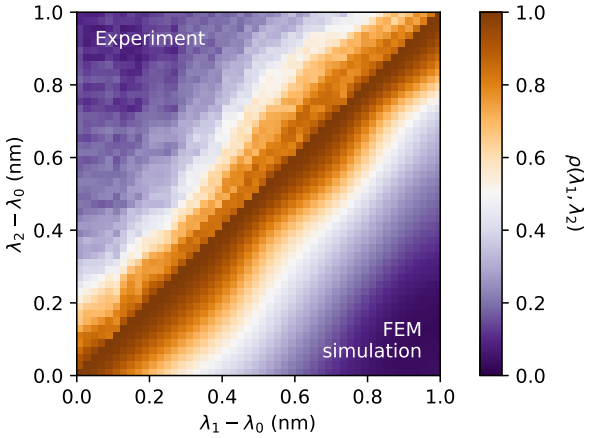

Figure 5.4: Correlation coefficient $\rho(\lambda_1, \lambda_2)$ of the measured (upper left) and FEM simulated (lower right) optical random field, at wavelengths λ_1 and λ_2 ($\lambda_0 = 1550\,\text{nm}$).

We can firmly state this, having developed a model that creates a field with correlation properties analogous to those of our measured field, which in fact does not contain any excess of *faithful* singularities for small persistences.

5.3.3. POISSONIAN MODEL AND FEM SIMULATIONS

We model the frequency-dependent field as a superposition of the cavity eigenstates $\mathscr{E}_x^j$, centered at frequencies $\tilde{\omega}_j = \omega_j + i\gamma_j$ [28]:

$$E_x(\mathbf{r}, \omega) = \sum_j \frac{\alpha_j \mathscr{E}_x^j(\mathbf{r}, \omega_j)}{\omega - (\omega_j + i\gamma_j)}. \tag{5.2}$$

Based on the size of our cavity we can estimate the average spectral separation between two consecutive eigenstates $\Delta = \langle \omega_{j+1} - \omega_j \rangle_j$ to be approximately 0.08 nm [28]. In the simplest model field, we assume the eigenstates to be equidistant in frequency (spacing Δ), with a constant width γ and a unitary weight ($\alpha_j = 1$). We set $\gamma = 0.16\,\text{nm}$, equal to the average loss rate of our system, which we determine from a finite difference time domain (FDTD) simulation of the entire three-dimensional chaotic cavity. Finally, following Berry's hypothesis [138], we consider every eigenstate to be a random superposition of monochromatic plane waves:

$$\mathscr{E}_x^j(\mathbf{r}, \omega_j) = \sum_{|\mathbf{k}| = n\omega_j/c} a_{x,\mathbf{k}} \exp(i\mathbf{k}\cdot\mathbf{r} + i\delta_{\mathbf{k}}), \tag{5.3}$$

where $\delta_{\mathbf{k}}$ is a random variable uniformly distributed in $[0, 2\pi]$ and $a_{x,\mathbf{k}} \propto |\mathbf{k} \times \hat{x}|$ is the polarization coefficient for the TE mode [87]. With these assumptions, we construct the wavelength-dependent field of Eq. (5.2) and determine the statistics of its singularities. We find that the persistence of singularities is exponentially distributed, with a characteristic decay rate that depends on the ratio between the eigenstates' width and spacing

γ/Δ. For our estimated parameters ($\gamma/\Delta \approx 2$) this results in $\lambda_d^{th} = 0.6\,\text{nm}$. The persistence calculated with our model is presented in Fig. 5.3(a) (gray line). In the region $\Delta\lambda > \lambda^*$ we obtain perfect matching between experiment and theory.

These theoretical results are confirmed by a 2D finite element method (FEM) simulation. The FEM simulation produces a direct expression of $\mathbf{E}(\mathbf{r},\omega)$, free of the previous model assumptions. The statistics for the singularities obtained from these simulations are reported in Fig. 5.3(c)-(d). Comparing the simulated persistence histogram to our model calculation we notice perfect agreement at every wavelength shift. No deviation from a single-exponential distribution in the region $\Delta\lambda < \lambda^*$ is present, and in the same region the fidelity fraction is lower than exeperimentally observed [Fig. 5.3(b),(d)]. It is interesting that we find a close correspondence between the correlation properties of measured and simulated fields: in both cases the correlation coefficient $\rho(\lambda_1,\lambda_2)$ decays over a finite wavelength shift of (Fig. 5.4), measurable in a half-width-half-max value $\text{HWHM}_e = 0.22(3)\,\text{nm}$ for the experiment and $\text{HWHM}_s = 0.26(3)\,\text{nm}$ for the simulation. We can therefore exclude the different behavior of the *short-living* population of singularities to originate merely as a consequence of the finite spectral correlation of the random wave field.

We note that we ruled out the eventuality in which the *short-living* population of singularities is generated by experimental artifacts such as noise in the measurements, temperature fluctuations or phase drifts. With this regard, independent measurements realized with different wavelength sweeps showed perfect consistency, demonstrating that variables which are not the wavelength shift cannot affect the final results [115]. Moreover, we introduced these as well as other possible measurement artifacts (i.e., perturbation from the near-field probe, frequency instabilities) in our models, in order to check if they could in any case lead to an enhanced population of faithful singularities at small $\Delta\lambda$: they did not show any.

5.4. A MODEL BASED ON TWO FAMILIES OF EIGENSTATES

Interestingly, we did find a modeling that reproduces the observed enhanced population. When a second family of eigenstates with a spectral width γ' different from the one of the original eigenstates is added to the decomposition of Eq. (5.2), two populations of singularities start to appear. Such an additional family of modes could be provided by resonances which due to polarization or physical separation would ideally remain orthogonal to the chaotic modes, but which get coupled to them in the real-life system.

In this model, the second family is characterized by eigenstates with a spectral width γ', which lie in between the eigenstates of the first family (spectral width γ), i.e.,

$$E_x(\mathbf{r},\omega) = \sum_j \frac{\mathscr{E}_x^j(\mathbf{r},\omega_j)}{\omega - (\omega_j + i\gamma)} + \sum_l \frac{\gamma'/\gamma\,\mathscr{E}_x^l(\mathbf{r},\omega_l)}{\omega - (\omega_l + \Delta/2 + i\gamma')}. \tag{5.4}$$

Coherently to what done in the previous model, the eigenstates of both families are equally spaced ($\omega_{j+1} - \omega_j = \Delta$), and their weight α_j has been set to unity. In this particular example we use $\gamma \approx 4\gamma'$.

In Fig. 5.5(a) we show the persistence histogram for the singularities of the field described in Eq. (5.4). We see that a deviation from a single exponential distribution takes

place in the region $\Delta\lambda < 0.2\,\text{nm}$. Moreover, from the same figure we notice that the number of faithful singularities increases when $\Delta\lambda$ approaches zero, as observed in the experiment. Figure 5.5(b) presents the wavelength-wavelength correlation coefficient of the field calculated according to Eq. (5.4). This is also qualitatively comparable with what found experimentally.

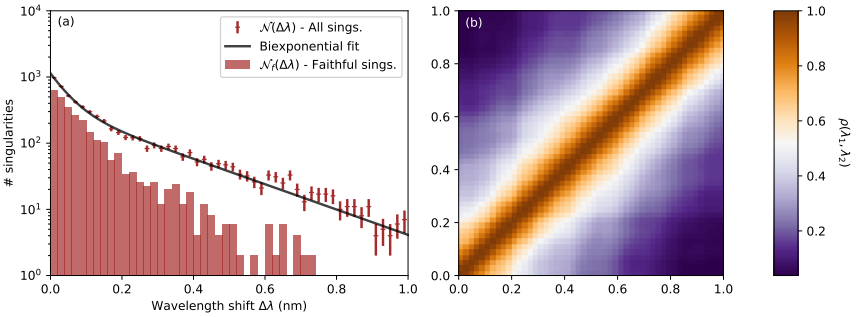

Figure 5.5: (a). Persistence histogram with fidelity for the field modeled according to Eq. (5.4), with $\gamma = 4\gamma'$. The plot is analogous to those reported in Fig. 5.3(a) and (b). Here, a biexponential fit (black line) highlights the deviation from single exponential distribution. (b). Wavelength-wavelength correlation function for the same field used in the panel (a). The correlation coefficient is calculated as explained in the main text.

To give a more comprehensive overview on this new model, we studied its behavior for different values of γ'. Figure 5.6 presents the persistence histogram for such proposed model case, at varying the ratio γ/γ'. For some choices of γ' a bi-exponential behavior appears. Specifically, we observed that such choices satisfy $\Delta \simeq \gamma \gg \gamma'$, in which cases an excess of faithful singularities living within the spectral correlation region of the field is again found.

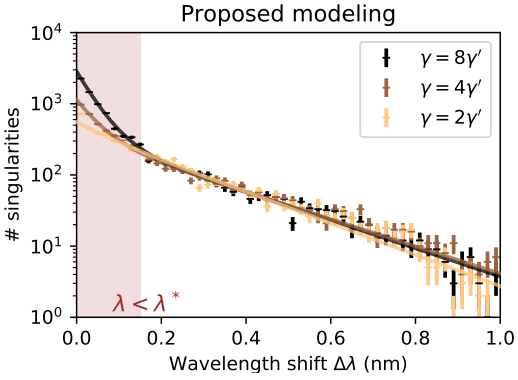

Figure 5.6: Persistence histograms for singularities arising in numerically generated random fields in which two families of eigenstates with different spectral width γ and γ' coexist. The lines are bi-exponential fits to the data points.

5.5. CONCLUSIONS

To conclude, we studied the persistence and pairing statistics of phase singularities in optical random waves. For singularities with a persistence longer than the spectral correlation of the random field, we find perfect agreement between experiment, simulation and theory. It is striking that, for singularities with a persistence that falls within the spectral correlation of the random field, we experimentally observe an excess of singularities compared to theoretical prediction, and these are more faithful than expected. With this regard, we propose a mechanism based on the coexistence of different families of eigenstates, which could lead to a full explanation of our experimental observation.

5.6. SUPPLEMENTARY INFORMATION

5.6.1. DETAILS ON THE NUMERICAL SIMULATIONS

We determine the average loss rate of the system from a three-dimensional FDTD simulation of the chaotic cavity, including the surrounding photonic crystal. The electromagnetic field is excited with a current source located inside the cavity and the loss rate is estimated from the relation

$$\gamma \simeq \frac{\int_{\partial D} d^2\mathbf{r}\,\mathrm{Re}[\mathbf{E}(\mathbf{r})\times\mathbf{H}^*(\mathbf{r})]}{\int_D d^3\mathbf{r}\,\varepsilon_0\varepsilon(\mathbf{r})|\mathbf{E}(\mathbf{r})|^2+\mu_0|\mathbf{H}(\mathbf{r})|^2}, \tag{5.5}$$

where the numerator and denominator represent the time-averaged energy flux leaving the computational domain D and the total electromagnetic energy inside the domain, respectively. This rate includes both losses due to light escaping into the coupling waveguides and scattering at the photonic-crystal edge.

The value of the electric field $\mathbf{E}(\mathbf{r},\omega)$ inside the cavity with varying frequency is calculated with a simplified two-dimensional geometry. We assume that the field can be factorized into the form

$$\mathbf{E}(\mathbf{r}) = \mathbf{E}^{(2D)}(x,y)\,\mathscr{E}_{\mathrm{TE}}(z), \tag{5.6}$$

where $\mathscr{E}_{\mathrm{TE}}(z)$ is the z-profile of the TE guided mode of a 220 nm silicon-on-insulator slab ($\hat{\mathbf{z}}$ is the out-of-plane direction) and $\mathbf{E}^{(2D)}(x,y)$ is a two-dimensional in-plane polarized field that satisfies the Helmholtz equation with the effective wavenumber $k_{\mathrm{TE}}(\omega)$, which can be obtained by inverting the dispersion relation of the TE guided mode. We simulate $\mathbf{E}^{(2D)}$ by the finite element method on a two-dimensional domain with the same shape as the chaotic cavity. On the boundary of the cavity, we set impedance boundary conditions for an effective band-gap optical material with the dielectric constant $\varepsilon = \varepsilon' + i\varepsilon''$ ($\varepsilon' < 0$), where ε'' is chosen so as to reproduce the loss rate of the three-dimensional FDTD simulations. Please note that such three-dimensional FDTD calculations were computationally very demanding, and not suitable for efficient wavelength-resolved simulations, which, with the required spectral resolution, required few weeks to be completed. However, we did perform a preliminary FDTD simulation of the full wavelength sweep, and this did not show any qualitative difference with the correspondent FEM simulation. For this reason we then used the FEM simulations, which were by about two orders of magnitude more efficient and gave us more flexibility in tuning different parameters.

III

POLARIZATION SINGULARITIES

6

SPATIAL BUNCHING OF SAME-INDEX C POINTS IN 2D RANDOM LIGHT

Two is not the double but the opposite of one, of its loneliness.
Two is an alliance, a double thread that is not broken.

[7] Erri De Luca

Topological singularities are ubiquitous in many areas of physics. Polarization singularities are locations at which an aspect of the polarization ellipse of light becomes undetermined or degenerate. At C points the orientation of the ellipse becomes degenerate and light's electric field vector describes a perfect circle in time. In 2D slices of 3D random fields the distribution in space of the C points is reminiscent of that of interacting particles. With near-field experiments we show that when light becomes truly 2D, this has severe consequences for the distribution of C points in space. The most notable change is that the probability of finding two C points with the same topological index at a vanishing distance is enhanced in a 2D field. This is an unusual finding for any system that exhibits topological singularities as same-index repulsion is typically observed. All of our experimental findings are supported with theory and excellent agreement is found between theory and experiment.

Parts of this chapter have been published in Physical Review X **8**, 041012 (2018) [139].

6.1. INTRODUCTION

LIGHT-BASED technology has transformed our society and will continue to do so, with applications that range from energy harvesting to telecommunications and quantum informatics [140–142]. Increasing control over light's polarization is one key capability inspiring new developments. For instance, optical fields near nanostructures can be engineered to exhibit locations of circular polarization [61, 98, 143], allowing applications such as spin-dependent directional coupling [20], also with local solid-state spin into optical information conversion [27]. Interestingly, points of circular polarization are singularities of the light field, also known as C points [6, 19], widely studied in structured light beams [25, 26, 114] and representative of the transverse spin momentum of light [21–24].

More in general, C points are topological defects of the vector field which describes light's polarization. The study and understanding of topological defects goes way beyond optics. Currently, dislocations of the local magnetization known as Skirmions are being intensively investigated [144–146]. In nematic systems, topological defects have continuously attracted interest because of their fascinating behavior [147, 148]. In addition, these kinds of defects can even govern the physics of biological system [149], and their spatial arrangement is representative of intrinsic properties of the system in which they are found [150].

Interestingly, the large ensemble of C points which naturally arises in random light fields also exhibits an emblematic and rigorous spatial distribution [42, 50, 151, 152], which resembles that of particles in a simple liquid and only scales with the wavelength of the interfering waves [151]. However, a random wave field can be realized in several ways [52, 153–158]. So far, the work has concentrated on the investigation of polarization singularities in two-dimensional (2D) slices through random three-dimensional (3D) fields in the paraxial limit. The question now arises as to how limiting the propagation of light to a truly 2D situation, e.g., by confining it on a flat optical chip, would be to the spatial distribution of its polarization singularities. In such a case, transverse propagation would set a one-to-one relation between the wave propagation direction and the direction of the electric field. Moreover, this would create correlations between right-handed and left-handed polarization that are absent in the three-dimensional fields.

With near-field experiments we investigate the spatial distribution of C points in a planar random light field and reveal crucial differences with respect to existing paraxial theory [151]. We demonstrate that confining light propagation in two dimensions leads to a large increase in the probability of finding, at close proximity, C points with the same topological charge, i.e., their index. This is an exotic behavior for topological singularities, which usually exhibit same-charge repulsion. We relate our experimental findings to light's handedness and excellently describe them with a new theoretical model developed for the two-dimensional case.

6.2. EXPERIMENT AND METHODS

6.2.1. NEAR-FIELD OPTICAL MEASUREMENTS

In our experiments, we map the near field of light waves propagating in the planar chaotic cavity sketched in Fig. 6.1(a). This is a photonic crystal cavity realized in a silicon-on-insulator platform (220-nm silicon slab) designed to provide random wave propagation [55]. With a monochromatic laser at the telecom frequencies ($\lambda_0 \simeq 1550\,$nm) we excite a transverse electric (TE) slab mode which results in a random superposition of monochromatic TE waves inside the cavity [87, 115]. With a custom-built near-field scanning optical microscope (NSOM) we probe the light field approximately 20 nm above the surface of the cavity. The measurement of the amplitude and phase of both the in-plane components (E_x, E_y) allows the full characterization of its polarization state at every point in the measured plane. For simplicity, we only consider the TE light propagating in the sample, which has its electric field entirely in the plane of propagation. We do not investigate TM light, as our cavity was not designed to confine [55].

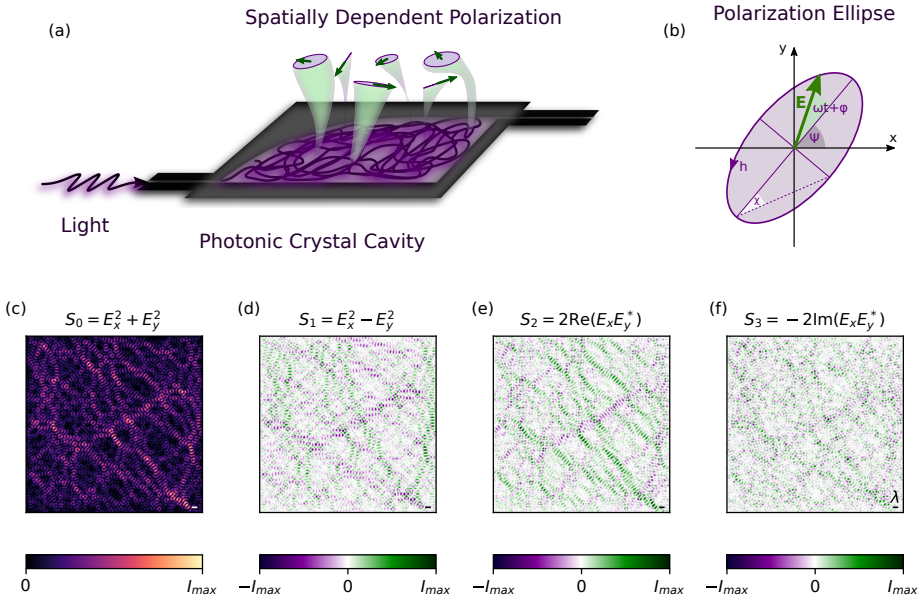

Figure 6.1: Overview of the near-field measurements of light's polarization in a chaotic cavity. (a) Schematic of the experimental realization of random light waves in the planar photonic crystal cavity (black). Inside the cavity, light exhibits a spatially dependent polarization. This is illustrated by a few different polarization ellipses (purple ellipses) observed at different points in the cavity (indicated by the green shadows). (b) Parametrization of the polarization ellipse, describing the local polarization state of light. (c)-(f) Near-field maps of the Stokes parameters of the optical random field in a square region of 17 µm × 17 µm inside the chaotic cavity. Note that $S_0 = E_x^2 + E_y^2$ is the total intensity of the vector field. This is displayed with a false-color map ranging from 0 to $I_{\max}$, where $I_{\max}$ is the maximum measured intensity. The parameters S_i ($i = 1,2,3$) describe the polarization state of light, with respect to linear (horizontal-vertical), linear (±45 deg) and circular (right-left) polarizations, respectively. These Stokes parameters are also represented with false-color maps, which this time range from $-I_{\max}$ to $I_{\max}$.

A comprehensive description of light's polarization is provided by its Stokes parameters [18]. These parameters are often used to characterize the polarization state of light in the far field, ranging from a simple laser beam to the polarized emission of exotic structures [159], but they can be used for a local analysis of the near field as well. Figures 6.1(c)-(f) present the near-field maps of the Stokes parameters for the optical random field inside the chaotic cavity. As result of vector light waves randomly interfering, these patterns are quite difficult to interpret. However, we can spot a few specific features in the morphology of each map. Note that S_1 exhibits patterns of spatial modulation approximately half a wavelength wide and several wavelengths long. Depending on their color (sign), these stripy patterns are either oriented along the x or the y axis. The same observation is valid for S_2, but here the modulations are oriented at ± 45 deg with respect to the horizontal axis. No clear preferential direction stands out from the map of S_3. In fact, S_1 is representative of light linearly polarized along x ($S_1 > 0$) or y ($S_1 < 0$), and since light propagates as a transverse vector wave, the observed stripy patterns are reminiscent of x-polarized waves mainly propagating along y and vice versa [87]. A totally analogous argument holds for S_2, while S_3 does not exhibit any pattern that bears a resemblance to any specific in-plane direction since it is the parameter representative of circular polarization.

6.2.2. LIGHT'S POLARIZATION AND C POINTS

A more concise yet comprehensive summary on the complex polarization pattern illustrated in Fig. 6.1 can be obtained from the analysis of its singularities [50]. In general, light's polarization is elliptical and thus parametrized with the orientation ψ of the polarization ellipse, the ellipticity angle χ and the handedness h [Fig. 6.1(b)]. However, there are special cases in which the polarization ellipse degenerates into a circle or a line, and some of these parameters are not well defined anymore. In two dimensions, such singularities of the vector field are, respectively, points of circular polarization (C points) and lines of linearly polarized light (L lines) [160].

Figure 6.2 is a map of the orientation of the polarization ellipse for a small subsection of the measurement presented in Fig. 6.1.The position of C points is highlighted by circles and triangles, whose color represents their topological index I. This is defined as the half-integer number of times that the axis of the polarization ellipse rotates around the singularity, clockwise (positive index) or anticlockwise (negative index), i.e.,

$$I = \frac{1}{2\pi} \int_{\mathscr{C}} d\psi \tag{6.1}$$

where $\mathscr{C}$ is a closed path enclosing one singularity. In Fig. 6.2, we only observe topological indices of $\pm 1/2$.

Strictly related to their topological index is the so-called line classification of C points, which differentiates them in three types: lemons, stars and monstars [161, 162]. The line classification can be understood by looking at the orientation of the polarization ellipse around the singularity, highlighted by the black directors in Fig. 6.2 and in the zoomed-in images of Fig. 6.3. For lemon-type singularities (lemons) there is only one direction along which the orientation of the polarization ellipse is directed towards the singularity, whereas the possible directions are always three for star-type singularities

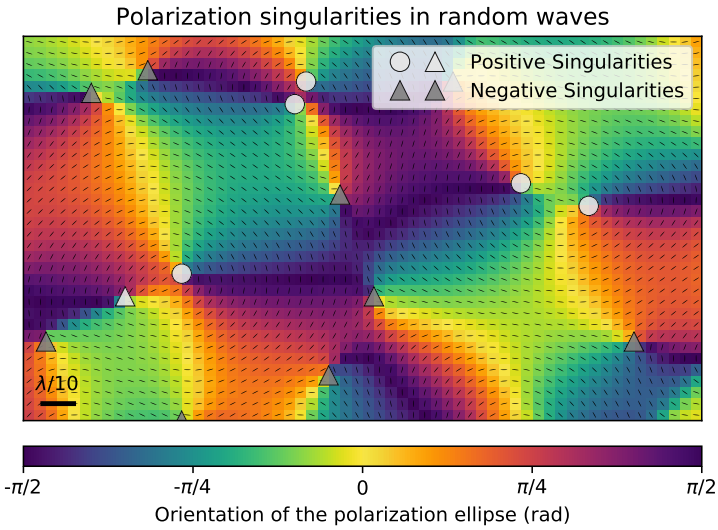

Figure 6.2: False-color map for the orientation of the major axis of the polarization ellipse. The black directors indicate the orientation of such an axis, too. The plot is representative of a subsection of the measured optical random field. Circles and triangles are C points. The white and gray symbols denote positive and negative topological indices, respectively. The shape of the symbols, triangles or circles, denotes a star-type or lemon-type classification, respectively.

(stars and monstars). To determine the line classification of all the C points in our data set in a deterministic way, we apply the method illustrated by Dennis for computing the number of directors pointing towards each singularity [161]. In our figures, we indicate stars and monstars with triangles, and lemons with circles.

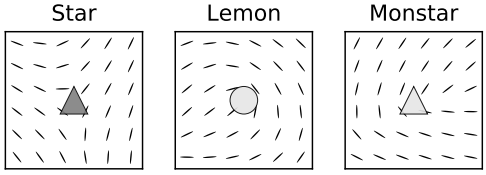

Figure 6.3: An overview of the three kinds of C points based on their line classification [161]. The lines are the orientation of the polarization ellipse at each pixel around the C point (circle or triangle), as determined from experimental data.

Already a quick glance at Fig. 6.2 illustrates the clear relation between the topological index (marker color) and the line classification (marker shape) of C points. In fact, negative-index singularities are always stars, whereas both lemons and monstars are characterized by a positive index, as expected, in general, for C points [161]. Table 6.1 lists the fraction of C points for each kind observed in our experimental data set. Note that 50% of the total number of C points are stars, and they all carry a negative topo-

logical index. Approximately 45% of the singularities are lemons, and only 5% monstars, both types exhibiting a positive index. In the same table, we directly compare our experimental outcome with the results from previous paraxial theory [151] and experiments [152]. All of these examined statistics are perfectly consistent with each other. In summary, the abundance of C points with a particular line classification is the same for C points in truly two-dimensional light and two-dimensional slices through a three-dimensional field.

Singularity	2D field	2D slice of a 3D field	
Type	Experiment	Experiment [152]	Theory [151]
Star	0.4997 ± 0.0002	0.506 ± 0.003	0.500
Lemon	0.4493 ± 0.0013	0.443 ± 0.002	0.447
Monstar	0.0503 ± 0.0013	0.050 ± 0.003	0.053

Table 6.1: Fraction of C points with different line classification. The results of our 2D experiment are compared with a previous experiments [152] and theory [151].

6.3. SPATIAL DISTRIBUTION OF C POINTS

6.3.1. PAIR AND CHARGE CORRELATION FUNCTION

Having established that there is no difference between the abundances of the various types of singularities observed in 2D slices of 3D light fields and truly 2D fields, the question now arises as to whether their distribution in space is also the same. The natural way of investigating the spatial distribution of pointlike singularities is by determining their pair correlation function $g(r)$. Given a C point, this function describes how the density of the surrounding C points varies as a function of distance. This method is widely used to describe the physics of discrete systems [163–168], it can be directly related to the structure factor [169], and it represents a spatial analogous of the degree of second-order coherence $g^{(2)}(\tau)$, commonly used to determine photon bunching and antibunching [170].

Figure 6.4 presents the pair correlation function for C points in two-dimensional random light, as obtained from our experimental data. With the position of each singularity known, we can compute their pairwise distances $|\mathbf{r}_i - \mathbf{r}_j|$, and eventually the pair correlation function

$$g(r) = \frac{1}{N\rho} \langle \sum_{i \neq j} \delta(r - |\mathbf{r}_i - \mathbf{r}_j|) \rangle, \tag{6.2}$$

where N is the total number of singularities, ρ is the average density of surrounding singularities, and δ is the Dirac function. We compute the average and uncertainty of such a correlation function by combining the outcome of 20 near-field measurements of the optical random field under investigation. In each of these maps, we precisely pinpoint the location and topological index of approximately 6500 C points, with a spatial accuracy that is limited by the pixel size of the experiment ($\approx 20\,$nm).

Note that $g(r)$ is not flat, indicating that C points in random light exhibit spatial correlation. At first glance, this $g(r)$ seems similar to the one of phase singularities in scalar random waves [17, 87] and therefore also reminiscent of that of particles in a simple liquid. In fact, $g(r)$ displays a damped oscillatory behavior around unity as a function of r, with a maximum, representative of a surplus of singularities, at approximately half a wavelength of distance. Surprisingly, the pair correlation of C points in 2D actually increases as r approaches 0. In principle, the zero dimensionality of optical singularities allows for a finite probability of having two at the same location. However, an increase of $g(r)$ towards zero has never been observed, neither for phase singularities in scalar or vector random waves [17, 87] nor for C points in a 2D slice of a 3D random field (Ref. [151] and gray lines in Fig. 6.4).

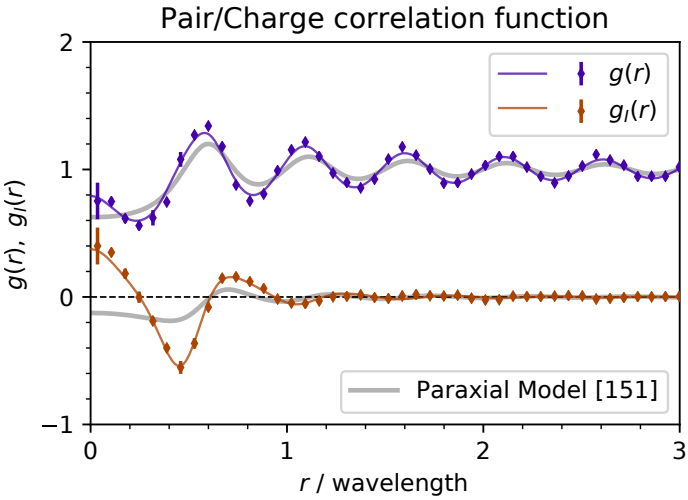

Figure 6.4: Pair and charge correlation function (g, g_I) for C points in random vector waves. The data points with errorbars are the results from our experiment, blue and orange solid lines show our model for 2D vector fields, and gray lines are the paraxial model [151].

To understand the unexpected behavior at small distances and to obtain an overview of the spatial distribution of the C points, it is useful to also consider the charge correlation function $g_I(r)$: a more general expression of the pair correlation function in which each singularity is weighted with its topological index [17]. The orange data points in Fig. 6.4 display our experimental results for $g_I(r)$. The most striking observation here is that the charge correlation function is positive near $r = 0$. This means that when singularities are found at a close distance from each other they most often carry the same topological index. Then, at $r \approx \lambda/4$ the charge correlation function flips sign, indicating the beginning of a displacement range where two singularities are more likely to have opposite sign. The zero crossing roughly coincides with the distance at which $g(r)$ exhibits the unexpected increase towards small r. This increase can therefore be attributed to the surplus of same-sign singularities in such a displacement range.

The reason why C points in 2D tend to rearrange to form closely spaced pairs with the same topological index is at this stage still unclear. The origin of the clustering should

be sought in correlations among different field components set by the modal properties of the field. However, the topological index is not the only intrinsic property carried by C points. We could gain more insight by analyzing their behavior with respect to light's handedness.

6.3.2. C POINTS AND LIGHT'S HANDEDNESS

The correlation functions displayed in Fig. 6.4 provide an extensive description of the distribution of C points but still not the full picture. This is because the information carried by C points is not limited to their topological index. In fact, light's polarization is purely circular at every C point; however, it can be left- or right-handed, independent of the topological index. In Fig. 6.5 we show a spatial map of the degree of circular polarization $s_3 = S_3/S_0$, together with the position, topological index and handedness of the C points therein. We notice how C points fall in domains of a given handedness. Of course, s_3 equals exactly $+1$ or -1 at every C point, with a sign that determines the handedness of the C point itself. Each domain is delimited by L lines (white lines), where polarization is purely linear ($s_3 = 0$), and light's handedness is undetermined. L lines have to separate C points of opposite handedness. Contrarily, several co-handed singularities can occur within the same domain. Furthermore, from Fig. 6.5 one immediately realizes how handedness and topological index of a C point are not directly related, as every combination of these quantities is possible.

The handedness of C points provides an additional degree of freedom to be accounted for in their spatial distribution. It is illuminating to include this degree of freedom

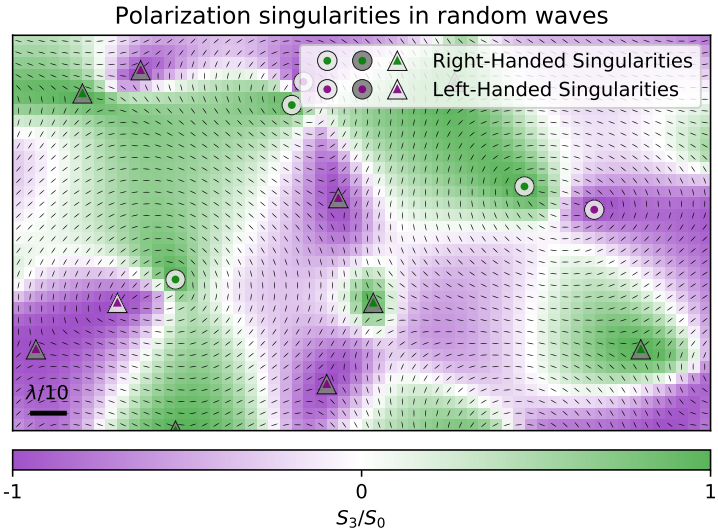

Figure 6.5: False-color map for the degree of circular polarization $s_3 = S_3/S_0$, as obtained from our experimental data. The plot corresponds to the same subsection of the measured optical random field displayed in Fig 6.2. The black directors indicate the orientation of the polarization ellipse. Circles and triangles are C points, and their inner color (purple or green) represents their handedness (left or right, respectively.

in the computation of a new set of pair correlation functions. In general, $g(r)$ can be expressed as the average of all possible partial correlation functions for C points with the same or opposite handedness and the same or opposite topological index:

$$g(r) = \frac{1}{16} \sum_{i,j} \sum_{\alpha,\beta} g_{i,j}^{\alpha,\beta}(r), \tag{6.3}$$

where $i, j \in [+,-]$ are indices for topological index and $\alpha, \beta \in [l,r]$ indicate handedness. Following the notation of Dennis [151], Eq. (6.3) can be simplified with the definitions

$$g_{\text{same}}^{C} \equiv g_{i,i}^{\alpha,\alpha} \quad \text{and} \quad g_{opp}^{C} \equiv g_{i,-i}^{\alpha,\alpha}, \tag{6.4}$$

both corresponding to co-handed singularities, for the cases of same and opposite topological indices, respectively. Analogously, for anti-handed C points we have

$$g_{\text{same}}^{A} \equiv g_{i,i}^{\alpha,\bar{\alpha}} \quad \text{and} \quad g_{\text{opp}}^{A} \equiv g_{i,-i}^{\alpha,\bar{\alpha}}. \tag{6.5}$$

Thus, we can express Eq. (6.3) as a function of these four correlation functions:

$$g(r) = \frac{1}{4} \left[g_{\text{same}}^{C} + g_{\text{opp}}^{C} + g_{\text{same}}^{A} + g_{\text{opp}}^{A} \right]. \tag{6.6}$$

Figure 6.6 presents our experimental results for the four pair correlation functions of the decomposition in Eq. (6.6), taking both the topological index and handedness of the C points into account. In the distribution functions depicted in Fig. 6.6(a), we only consider co-handed C points, either with the same (green) or opposite (purple) topological indices. In this case, the experimentally determined functions describe the standard characteristic properties exhibited by phase singularities in random waves. In fact, $g_{\text{same}}^{C}(r \to 0) = 0$ for singularities with the same topological index, and a monotone decrease towards finite value at $r \to 0$ in g_{opp}^{C}. The experimental results displayed in Fig. 6.6(a) perfectly match the prediction of the model for polarization singularities in a 2D slice of a 3D field in the paraxial regime [151], which is equivalent to the model for phase singularities in scalar random waves [17].

In fact, we can interpret C points as phase singularities in either the left- or right-handed circular components of **E**:

$$\psi_l = E_x + iE_y, \quad \psi_r = E_x - iE_y. \tag{6.7}$$

This is because a phase singularity in ψ_l corresponds to a zero in ψ_l, resulting in a point where **E** only has contributions from its circular-right component ψ_r, i.e., a right-handed C point, and vice versa. Therefore, the spatial distribution of co-handed C points is exactly equivalent to that of phase singularities arising in a single circular field component $\psi_{l/r}$, i.e., of phase singularities in a scalar random wave field [151].

Our experiment confirms that also in 2D the distribution of co-handed C points is the same as that of phase singularities in a scalar random field. Therefore, the origin of the unusual behavior of the global distribution of C points must necessarily lie in anti-handed singularities. Figure 6.6(b) presents the correlation functions for singularities with opposite handedness. Here, $g_{\text{same}}^{A}(r)$ reaches its maximum values at $r \approx 0$. Singularities of opposite handedness and the same topological index are often found at close

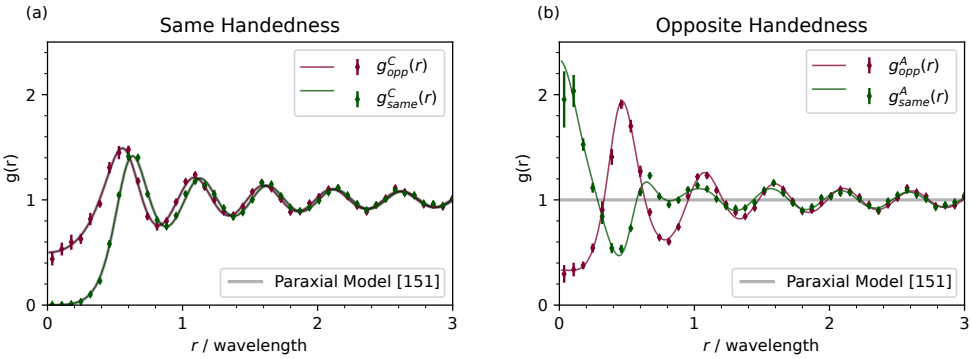

Figure 6.6: Pair correlation function $g(r)$ for C points with the same (a) or opposite (b) handedness, and the same (g_{same}) or opposite (g_{opp}) topological index. Data points represent our experimental results, colored solid lines show our model for an isotropic 2D random field, and solid gray lines are the 3D paraxial model [151]. The solid gray lines in panel (a) overlap exactly with the colored solid lines.

distances from each other, confined in an extremely subwavelength regime. Regarding pairs of C points with opposite topological index, the distribution g^A_{opp} exhibits a behavior that is qualitatively very similar to that of g^C_{opp}. This result creates two clearly distinct behaviors for the four combinations of index and handedness. On the one hand, the impact of the handedness of C points on their spatial correlations seems to be only minor for singularities with opposite topological indices, for which we do not observe big qualitative differences between g^C_{opp} and g^A_{opp} (purple data in Fig. 6.6). On the other hand, considering the same or opposite handedness is crucial in the same-index case, since the behaviors of g^C_{same} and g^A_{same} are evidently different, eventually with an opposite gradient for $r \to 0$ (green data in Fig. 6.6).

As a matter of fact, the data displayed in Fig. 6.6(b) offer a clear illustration of the novel behavior registered for C points in 2D random light compared to the case of a 2D slice of a 3D field. In particular, it clarifies that, in the 2D case, C points of opposite handedness are far from being independent and so must be for the left- and right-handed field projections from which they arise.

6.4. CORRELATION AMONG LIGHT'S VECTOR COMPONENTS

The overall spatial correlation of C points in 2D random light (Fig. 6.4) and, more specifically, the correlation of singularities with opposite handedness [Fig. 6.6(b)], exhibit a number of features that were not accounted for in a previous paraxial theory [151]. In that theory, an assumption was made, consisting of the absence of any correlation between oppositely handed C points, i.e., $g^A_{\text{same}} = g^A_{\text{opp}} = 1$. This assumption corresponds to a situation in which ψ_l and ψ_r are completely uncorrelated.

In fact, in three dimensions there are no restrictions that would imply a correlation among the circular components ψ_l and ψ_r of a paraxial random field. The same holds true for a two-dimensional slice of such a three-dimensional field [152]. In this circumstance, transversality can be fulfilled out of the plane in which the field is observed,

meaning that the vector components of such a field can even be independently generated. Contrarily, in a truly two-dimensional vector field transverse propagation must be fulfilled in the same plane in which the waves are actually propagating. Dismissing the third dimension while obeying transversality then results in a correlation among the vector components of the field, eventually its left- and right-handed projections.

We now adapt the paraxial model of Dennis [151] in order to account for the correlations intrinsic to a 2D light field. The key for explaining our results is that in our system the electric field can be modeled as a superposition of TE waves only. Note that we would find completely equivalent results considering the in-plane component of a field composed only of TM waves (see Section 6.6.1). Contrarily, the coexistence of two independent TE and TM fields would add one extra degree of freedom to the system. In the unlikely scenario in which those two contributions have equal wavelength and amplitude for a given optical frequency, the results for the spatial correlation of C points would revert back to those observed in a 2D slice of a 3D field [139]. A TE mode in 2D can be expressed starting from a scalar field H_z:

$$\begin{cases} E_x = & k_y H_z \\ E_y = & -k_x H_z, \end{cases} \tag{6.8}$$

which, by default, satisfies the transverse condition.

For a random wave field, we follow Berry's hypothesis and assume that H_z is an isotropic superposition of monochromatic plane waves, each of them with a random phase $\delta_{\mathbf{k}}$ [17],

$$H_z = \sum_{|\mathbf{k}|=k_0} \exp(i\mathbf{k}\cdot\mathbf{r} + i\delta_{\mathbf{k}}), \tag{6.9}$$

where $\delta_{\mathbf{k}}$ is a random variable uniformly distributed in $[0, 2\pi]$. The autocorrelation of such a scalar, random, wave field is well known [17]: It is a Bessel function of order zero,

$$C_{zz}(\mathbf{r}) = \int d\mathbf{r}_0\, H_z^*(\mathbf{r}_0) H_z(\mathbf{r}_0 + \mathbf{r}) = J_0(k_0 r). \tag{6.10}$$

The autocorrelations of E_x and E_y are also known [87], the main difference with $C_{zz}(\mathbf{r})$ being an anisotropic term dependent on the orientation φ of $\mathbf{r}$:

$$\begin{aligned} C_{xx}(\mathbf{r}) = & \frac{1}{2}\left[J_0(k_0 r) + \cos(2\varphi)\, J_2(k_0 r)\right], \\ C_{yy}(\mathbf{r}) = & \frac{1}{2}\left[J_0(k_0 r) - \cos(2\varphi)\, J_2(k_0 r)\right]. \end{aligned} \tag{6.11}$$

Also highly relevant to our study is the cross term among E_x and E_y, which exhibits the following correlation:

$$\begin{aligned} C_{xy}(\mathbf{r}) = & \int d\mathbf{r}_0\, E_x^*(\mathbf{r}_0) E_y(\mathbf{r}_0 + \mathbf{r}) \\ = & \frac{1}{2}\sin(2\varphi)\, J_2(k_0 r). \end{aligned} \tag{6.12}$$

This equation can be easily proven by carrying out the integral in Fourier space and substituting the relations $E_x(\mathbf{k}) \propto \sin(\theta_{\mathbf{k}})\,\delta(|\mathbf{k}| - k_0)$ and $E_y(\mathbf{k}) \propto -\cos(\theta_{\mathbf{k}})\,\delta(|\mathbf{k}| - k_0)$ [87]. It

is interesting to note that E_x and E_y only exhibit correlation when displaced since $C_{xy}(\mathbf{r})$ lacks the term proportional to J_0, and $J_2(0) = 0$.

Known these correlation functions, and given the expression of ψ_l and ψ_r [Eq. (6.7)], we have all the ingredients to compute the correlations among the circular components of a TE random vector field. The autocorrelation of the left-handed component is

$$\begin{aligned} C_{ll}(\mathbf{r}) = & \int d\mathbf{r}_0\, \psi_l^*(\mathbf{r}_0)\, \psi_l(\mathbf{r}_0+\mathbf{r}) \\ = & \quad C_{xx}(\mathbf{r}) + C_{yy}^*(\mathbf{r}) = \quad J_0(k_0 r), \end{aligned} \tag{6.13}$$

and similarly for $C_{rr}(\mathbf{r})$. The result of Eq. (6.13) is also identical to what we obtained in Eq. (6.10) for H_z, proving that each separate circular component behaves as a random scalar field. Similarly to Eq. (6.13), we can finally determine the correlation among left and right circular components:

$$C_{lr}(\mathbf{r}) = \left[\cos(2\varphi) - i\,\sin(2\varphi)\right] J_2(k_0 r) \tag{6.14}$$

and

$$C_{rl}(\mathbf{r}) = \left[\cos(2\varphi) + i\,\sin(2\varphi)\right] J_2(k_0 r). \tag{6.15}$$

As elegantly explained by Berry and Dennis [17], the autocorrelation function of a complex field contains all the information needed to retrieve the pair and charge correlation function of its phase singularities. In the case of C points, i.e., phase singularities in the right- or left-handed field component, the cross terms (C_{rl} and C_{lr}) are also necessary. Following the same procedure of Berry and Dennis, we first calculate the point density of singularities in a scalar complex field, e.g., $\psi_l \equiv \psi_l' + i\psi_l''$, which is defined as

$$\rho[\mathbf{u}_l] = \delta(\psi_l')\delta(\psi_l'') \left| \frac{\partial\psi_l'}{\partial x}\frac{\partial\psi_l''}{\partial y} - \frac{\partial\psi_l'}{\partial y}\frac{\partial\psi_l''}{\partial x} \right|, \tag{6.16}$$

where δ indicates the one-dimensional Dirac delta function, and where, for compactness, we have introduced the real vector $\mathbf{u}_l = [\psi_l', \psi_l'', \partial_x\psi_l', \partial_y\psi_l', \partial_x\psi_l'', \partial_y\psi_l'']^T$. An analogous density can be defined for ψ_r.

The pair correlation function between C points at two different space points $\mathbf{r}_A$ and $\mathbf{r}_B$ and with opposite handedness can now be written in a straightforward way as

$$g^A(\mathbf{r}_B - \mathbf{r}_A) = \frac{\langle \rho[\mathbf{u}_l(\mathbf{r}_A)]\, \rho[\mathbf{u}_r(\mathbf{r}_B)] \rangle}{\langle \rho[\mathbf{u}_l(\mathbf{r}_A)] \rangle \langle \rho[\mathbf{u}_r(\mathbf{r}_B)] \rangle}. \tag{6.17}$$

In this equation, the notation $\langle f[\mathbf{u}_l(\mathbf{r}_A), \mathbf{u}_r(\mathbf{r}_B)] \rangle$ indicates the statistical average of a generic f, the functional of the field components and of their derivatives at different points in space. Introducing the combined vector $\mathbf{u} = [\mathbf{u}_l(\mathbf{r}_A), \mathbf{u}_r(\mathbf{r}_B)]^T$, the average can be explicitly written in the form

$$\langle f[\mathbf{u}] \rangle = \frac{1}{(2\pi)^{D/2}\sqrt{\det M}} \int d^D\mathbf{u}\, f[\mathbf{u}] \exp(-\tfrac{1}{2}\mathbf{u}^T M^{-1}\mathbf{u}), \tag{6.18}$$

where D is the dimension of the vector $\mathbf{u}$ and M is the matrix of the correlations between the various components of $\mathbf{u}$, i.e., $M_{ij} = \langle u_i u_j \rangle$. These elements correspond to the correlations between the different components of the left- and right-handed fields that we

have summarized above, as well as their spatial derivatives. Similar expressions for different combinations of the fields ψ_l and ψ_r and for specific choices of the index of the singularities can be obtained from Eq. (6.17) with intuitive modifications.

In some particular cases [17, 87, 151], it is possible to derive a closed analytical expression for averages of the form in Eq. (6.17) by reducing the integrand to a quadratic form and integrating with standard mathematical techniques [171]. However, the specific form of the correlation matrix in our model does not lend itself easily to applying the formalism of Ref. [171]. This is because of the additional correlations between the real and imaginary parts of the field components, corresponding to the imaginary terms in C_{lr} and C_{rl} [Eqs. (6.14) and (6.15)]. Nevertheless, the average in Eq. (6.17) is particularly suited to numerical integration with Monte Carlo techniques [172]. We therefore calculate the pair correlation functions of C points and polarization vortices in two steps. First, we analytically perform the integral over the terms containing the Dirac delta functions in the integrand of Eq. (6.17). Subsequently, numerically we carry out the integration over the remaining variables, using the multidimensional Monte Carlo method [172]. We also validate our theoretical results by numerically simulating the superposition of random plane waves with TE polarization. The simulation results were all found in excellent agreement with the theoretical ones and are therefore not shown here.

We plot the theoretical expectations for the pair and charge correlation functions in direct comparison with the experimental data. In Fig. 6.4, we show the pair and charge correlation function for C points in 2D random vector waves and, in Fig. 6.6, the pair correlation functions for C points with the same or opposite handedness, respectively. For each of these curves we find an excellent agreement with the experiment. In particular, the pair correlation functions displayed in Fig. 6.6(b) for C points with opposite handedness represent the major novelty introduced by the model for 2D light. Among these functions, g^A_{same} exhibits a behavior that is extremely unusual for pair correlations of this kind. Although this behavior is perfectly consistent with the experimental observation, it might conceal further interesting properties of random light confined in 2D.

6.5. CONCLUSIONS

In this work, we investigated the spatial correlation of C points in 2D random light. We compared it to existing theory and experiments for 2D slices through a 3D random field in the paraxial regime. We demonstrated that confining the optical field to propagate in two dimensions induces severe changes in the spatial distribution of its C points. The shortage of degrees of freedom caused by the removal of one dimension results in a correlation among the vector components of the 2D light field. In the circular basis, this results in a correlation among the oppositely handed optical-spin components of light. One of the key consequences was the observation that the chance of finding C points with same topological index actually increases as their mutual distance goes to zero. This is an unusual finding for dislocations of any kind. We quantify the correlation between left- and right-handed spin for the case of a TE field and incorporate it in a newly developed theoretical model. Our results are general for in-plane fields, including those of a TM mode as well. The outcome of the 2D model is found to be in perfect agreement with our experimental results. Given the unusual properties of the ensemble of

C points in 2D random vector waves, our findings may trigger a reevaluation of concepts that are considered pillars of singular optics and topological defects, i.e., the sign principle [37] and topological screening [41]. Moreover, we anticipate that our results will trigger investigations of the evolution of C points as a function of external parameters, in order to explore phenomena such as same-index attraction and the formation of bound states among pairs of C points, which would be compatible with our observed correlation functions. Finally, the behavior at short distances might lead to more unexplored features such as polarization vortices and higher-order singularities.

6.6. SUPPLEMENTARY INFORMATION

6.6.1. ANALOGY BETWEEN TE AND TM MODES

As introduced in Eq. (6.8), we can express a TE mode in 2D starting from a scalar field H_z:

$$\mathbf{E}^{TE} = \begin{pmatrix} k_y \\ -k_x \\ 0 \end{pmatrix} H_z \tag{6.19}$$

which satisfies transverse propagation in the $x-y$ plane for the electric field:

$$\mathbf{k}\cdot\mathbf{E} = 0. \tag{6.20}$$

In Eq. (6.7), H_z is actually the out-of-plane component of the magnetic field, up to a normalization constant. However, this is not the only components of the magnetic field, which also has (imaginary) in-plane components

$$\mathbf{H}^{TE} \propto \begin{pmatrix} k_z k_x \\ k_z k_y \\ k_0^2 \end{pmatrix} H_z. \tag{6.21}$$

This expression can be easily verified by using the divergence equation for the magnetic field ($\nabla\cdot\mathbf{H} = 0$) and the z component of the rotation equation for the magnetic field ($\nabla\times\mathbf{H}|_z \propto E_z = 0$). In this formula, k_x and k_y are the x and y Cartesian components of the wavevector $\mathbf{k}$, k_0 is the amplitude of such an in-plane wavevector ($k_0^2 = k_x^2 + k_y^2$), and k_z is the out-of-plane wavevector component, which is purely imaginary and describes the decay of the evanescent field away from the 2D structure.

It is very easy to relate TE fields to TM fields. In fact, electric and magnetic fields of a TM mode are analogous to magnetic and electric fields of a TE mode, respectively. This results in the following TM fields

$$\mathbf{E}^{TM} \propto \begin{pmatrix} k_z k_x \\ k_z k_y \\ k_0^2 \end{pmatrix} E_z, \qquad \mathbf{H}^{TM} \propto \begin{pmatrix} k_y \\ -k_x \\ 0 \end{pmatrix} E_z, \tag{6.22}$$

Where it appears E_z as the out-of-plane component of the electric field, up to a normalization constant. In our work we study the case of a TE mode, where H_z is a scalar random field. In general a TM mode will correspond to another random field E_z. For simplicity we now consider the case in which $E_z = H_z$, which allows us to conveniently express the in-plane components of the electric field for a TM mode as a function of the electric field of a TE mode:

$$\begin{pmatrix} E_x \\ E_y \end{pmatrix}_{TM} \propto \begin{pmatrix} 0 & -1 \\ 1 & 0 \end{pmatrix} \begin{pmatrix} E_x \\ E_y \end{pmatrix}_{TE}. \tag{6.23}$$

We now demonstrate that the relation of Eq. (6.23) leads to equivalent C points for the two-dimensional TE or TM fields. The more general situation in which $E_z \neq H_z$ will simply correspond to a different realization of the starting random field, leading to a different set of C points, but with no consequences on their spatial correlation.

In Eq. (6) of the main text we introduced the circular components of the vector field **E**:

$$\psi_l = E_x + iE_y, \quad \psi_r = E_x - iE_y. \tag{6.24}$$

If we calculate such circular field components for a TM mode, we find that we can express them as a function of the same component for the TE mode:

$$\psi_l^{TM} = E_x^{TM} + iE_y^{TM} = -E_y^{TE} + iE_x^{TE} = i\psi_l^{TE},$$

and similarly for the right-handed component ψ_r. The only difference among the TE and TM circular fields consists in a global phase-shift of $\psi_{l/r}$. Such a phase shift does not influence existence and position of the phase singularities arising in $\psi_{l/r}$. As explained in the main text, every C point in the in-plane field **E** corresponds to a phase singularity in either ψ_l or ψ_r. So we can conclude that when $E_z = H_z$ the C points of the in-plane electric field of a TM mode are exactly the same as those of a TE mode. In general, when $E_z \neq H_z$ are arbitrary scalar random wave fields, the C points of the corresponding TE/TM mode will follow exactly the same statistics, both in index and handedness, as described in the main text.

7

POLARIZATION VORTICES

Tiger got to hunt, bird got to fly;
Man got to sit and wonder "why, why, why?"
Tiger got to sleep, bird got to land;
Man got to tell himself he understand.

[8]Kurt Vonnegut

When the position of two singularities of equal topological index coincides, a higher order singularity with twice the index is created. In general this is not an event that takes place spontaneously, especially when it involves point-like entities like phase or polarization singularities in 2D. Here, we present the observation and the spatial correlation of polarization vortices in 2D random vector waves. These are higher-order singularities resulting from the overlap of two C points with the same topological index. We discover that polarization vortices of positive index are observed to spontaneously occur more frequently than their negative counterpart, which results in a symmetry breaking with unprecedented equals. We expand on this finding by analyzing the spatial correlation of C points, which is indeed found to exhibit different behavior for $++$ and $--$ pairs.

7.1. INTRODUCTION

Measurable quantities circulate around their singularities and whether they do it clockwise or anticlockwise determines their topological charges, or indices [7]. In the case of polarization singularities, the rotating quantity is the orientation of the polarization ellipse. This orientation, or director, rotates over an angle $\pm\pi$ around ordinary C points [160]. In principle, one can also have a $\pm n\pi$ angular variation around the singularities, where n can be any integer number, so to avoid discontinuities in the ellipse's orientation [173]. For n bigger than 1, these are nth-oder singularities of the field [174]. High-order singularities can be designed to emerge in the central axis of vortex beams of arbitrary angular momentum [175], as for radially and azimuthally polarized beams [176–179]. In these cases, the optical fields are purposely engineered to exhibit these exceptional points. Instead, a lot more peculiar is the case in which high-order singularities are spontaneously formed, for example starting from a disordered ensemble of single-order ones. This typically is not allowed, as in the case of phase singularities in a random wave field, which exhibit mutual repulsion when they share the same topological charge (Chapter 3). But as demonstrated in Chapter 6, the story is different for polarization singularities in 2D random light, where the vicinity of same-index C points is enhanced with respect to opposite-index ones. This suggests that two C points of half-integer index can approach to a separation of zero and thereby give rise to a higher-order singularity of integer index, around which the polarization ellipse rotates by $\pm 2\pi$. Analogous higher-order singularities have also been observed in a few different frameworks, such as spinorial quantum fluids [180], or in correspondence of a bound state in the continuum [181, 182], and they are known as polarization vortices. In this chapter, we show that we are able to experimentally observe polarization vortices in 2D random fields. We demonstrate that these high-order singularities obey strict spatial correlation rules. Most surprisingly, polarization vortices in random waves do not satisfy charge neutrality, as an excess of positive vortices is found with respect to negative ones. This imbalance of topological indices concerns the ensemble polarization vortices only, since considering all the singularities of the field will still lead to index neutrality. We trace our findings back to the correlation of pairs of same-index C points in random light, which helps understanding the asymmetry in vortex creations. Finally, we employ the model for 2D random fields described in Chapter 6 to underpin the index imbalance as a consequence of confining the propagation of light in a 2D plane, finding a good agreement between experiment and theory.

7.2. INDENTIFICATION OF POLARIZATION VORTICES

Finding the polarization vortices in the near-field of two-dimensional random waves requires a dedicated analysis method. In principle, the detection of a polarization vortex is equivalent to that of single-order singularities, except that a double index must be observed. In practice, this requires some modifications to the algorithm described in Section 3.2.2. In that case, an integration path of 2×2 pixels was used. Such a path would not be enough to detect a phase circulation of 4π. To avoid confusion, we reiterate that C points (index $I = \pm 1/2$) are phase singularities (charge $q = \pm 1$) in the constructed

field $\Psi = S_1 + iS_2$ (see Chapter 6). Polarization vortices (index $I = \pm 1$) therefore appear as phase vortices of charge $q = \pm 2$ in Ψ. For practical convenience, we always detect C points and polarization singularities as phase singularities in Ψ. For this reason we need to be able to detect a phase circulation of $\pm 4\pi$ in order to determine the location of polarization vortices.

Such a phase change is too fast to be encoded by only four pixels. Thus, the algorithm described in Chapter 3 will always indicate the existence of a pair of single-order singularities displaced by a single pixel. At this point two approaches can be pursued. In a first approach one could still use the existing algorithm, and establish that when two C points are displaced by a single pixel they actually correspond to a polarization vortex. Alternatively, a new detection algorithm can be designed to perform phase integrals over 3×3 pixels loops. This larger integration path indeed allows for the direct visualization of second order singularities. After verifying that both approaches yield the same results, we only applied the second method for the data presented in this chapter.

Figure 7.1 presents an illustrating set of 24 of the polarization vortices detected in our measured random field. Depending on their topological index ($I = \pm 1$), the polarization vortices exhibit different topologies that also differ from the three classes of C points described in Chapter 6. Considering the orientation of the major axis of the polarization ellipse around the vortices (Fig. 7.1), we identify two possibilities. In the case of negative vortices (-1) the directors point towards the singularity along four directions, forming a four-pointed star. For positive vortices ($+1$) there is no direction along which the ellipse axes point towards the singularity, resulting in a circular pattern around the vortex.

With a pixel size of 17 nm, corresponding to integration loops with approximately 50 nm per side, we detect on the order of 80 polarization vortices per measured field map ($17\,\mu\text{m} \times 17\,\mu\text{m}$). This number is a lot smaller than the number of C points detected in the same field map (≈ 6500). The fact that only a small fraction of the total amount of C points leads to polarization vortices is justified by the high-order nature of the latter. It is important to stress that the experimental determination of a polarization vortex is a complicated task to be achieved with an experimental approach. In fact, resolution as well as pixel size are necessarily finite. Instead, polarization vortices are the result of the perfect overlap of two point-like entities, and are therefore impossible to observe with a finite resolution. What we have done here is to set an effective threshold below which two same-index C points are considered as one single polarization vortex. Pragmatically, we set this distance to be the pixel size of our experiment. Changing this threshold would change the number of vortices detected as such, and therefore their density. Still, with a pixel size of less than 20 nm we are in the regime where the pair correlation function of C points is rather flat (Fig. 6.4, Chapter 6), so we can reasonably expect that the number of detected vortices would simply scale linearly with the threshold distance.

Especially after these considerations, the study of spatial correlations among polarization vortices becomes a lot more insightful and insightful than their bare observation. The observation of a clear spatial correlation would unveil the presence of an underlying physical mechanism governing their collective behavior rather than them being positioned at random.

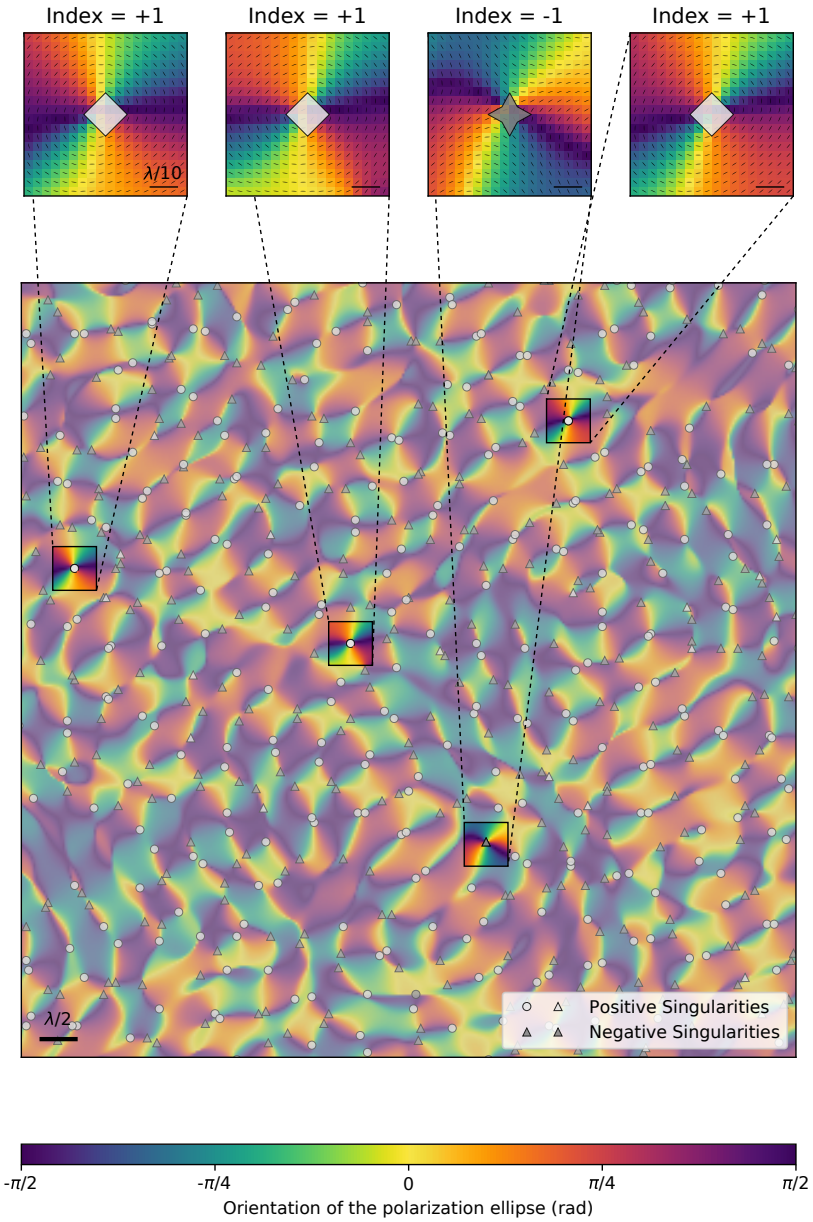

Figure 7.1: False-color map for the orientation of the major axis of the polarization ellipse in a 2D random light field (main plot). The black directors indicate the orientation of such an axis, too. The plot is a 8.5µm × 8.5µm subsection of the total measured map. Circles and triangles are C points. The color of the symbols, white or black, denotes a topological index $I = +1/2$ or $I = -1/2$, respectively. The shape of the symbols, triangles or circles, denotes a star-type or lemon-type classification, respectively. In the observed map, four occurrences of the formation of polarization vortices are highlighted (zoomed-in figures in the panels above the main plot). These are depicted by white (index $I = +1$) or black (index $I = -1$) symbols.

7.3. SPATIAL CORRELATION OF POLARIZATION VORTICES

To characterize the spatial correlation of the polarization vortices we compute their pair and charge correlation function. This is done in analogy to what presented for phase singularities in Chapter 3 and for C points in Chapter 6. However, the statistics offered by a single measurement is strongly reduced for the case of polarization vortices (~ 80 vortices $vs \sim 6500$ C points). For this reason, we combine the statistics from 150 different measurements of the random light field in order to calculate the pair correlations discussed in this section.

7.3.1. PAIR AND CHARGE CORRELATION FUNCTIONS

Interestingly, polarization vortices do exhibit a clear spatial correlation. Figure 7.2 presents the pair and charge correlation function for polarization vortices in 2D random vector waves. In these correlation functions we can identify several characteristic features. Firstly, $g(r)$ clearly tends to zero when $r \approx 0$, indicating that polarization vortices of any sign are never to be found in complete overlap. Secondly, the oscillations of this

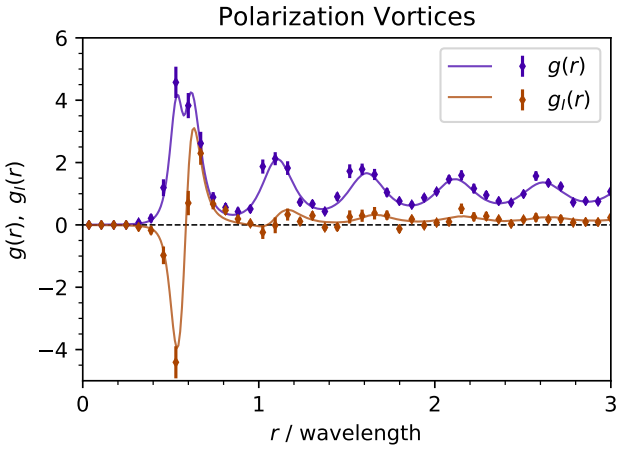

Figure 7.2: Pair (g) and charge (g_I) correlation function for polarization vortices in random waves. The data points are representative of the experimental results, while solid lines are the result of the theory for polarization vortices in 2D random light.

correlation function show a much stronger contrast compared to the one displayed by C points (Fig. 6.4) and phase singularities (Figs. 3.3 and 3.5). The first peak reaches values ≥ 4, more than twice as high as the values observed in the pair correlation function for C points. Additionally, this first peak in the $g(r)$ actually consists of two peaks. It is revealing to combine this observation with the information contained in the charge correlation function $g_I(r)$. In fact, in the displacement range contained within the double peak of the $g(r)$, the $g_I(r)$ exhibits a zero crossing, going approximately from -4 to 2.5 over a distance less than one fifth of the wavelength of light. Not only is it clear that the average nearest-neighbor distance for pairs of same-sign vortices is 20% bigger than that

of opposite-sign vortices, but the statistical distribution around these average values is narrow enough to resolve it as a double peak in the $g(r)$.

This is the first hint that polarization vortices of opposite topological index are displaying different statistical properties. Another observation that must be made at this point, is that $g_I(r)$ does not display a damped oscillatory behavior about zero as r increases, but it approaches a finite, positive, value. The charge distribution function is a measure of the number of vortices displaced by a distance r and weighted with their topological index. Therefore, a positive asymptotic value indicates an imbalance in the index distribution. In fact, if more positive than negative indices are present, the number of same-sign pairs will necessarily be higher than that of opposite-signed pairs, yielding a positive value of the charge correlation function g_I at large distances. We can express this in formulas, with N_+ as the number of positive vortices and N_- as the number of negative ones. Then, if $N_+ = fN_-$, we have that the number of pairs of same-index singularities is

$$N_{\text{same}} = N_+(N_+ - 1) + N_-(N_- - 1) = (1 + f^2)N_+^2 + \mathcal{O}(N_+), \tag{7.1}$$

whereas the number of pairs with opposite index is

$$N_{\text{opp}} = N_+N_- + N_-N_+ = 2fN_+^2. \tag{7.2}$$

When $r \to \infty$, we can neglect the term $\mathcal{O}(N_+)$, resulting in

$$g_I(r \to \infty) \propto N_{\text{same}} - N_{\text{opp}} \propto 1 + f^2 - 2f = (1 - f)^2 > 0 \qquad \forall f \neq 1. \tag{7.3}$$

The imbalance in the indices is evident already when counting the number of positive and negative polarization vortices found in our measurements. In a total of 150 measurements, we find an average ratio of vortices $f = N_+/N_- \approx 2.3$. Such an imbalance in topological index is quite an unusual result for singularities in random fields. The statistical properties of the singularities with positive topological charge (index) are usually completely analogous to those of the ones with negative charge (index) [151]. To understand the origin of the asymmetry that we find, it is useful to take one step back and reconsider the entities of which polarization vortices are constituted: pairs of C points. An imbalance in the index of vortices must hence originate from a different spatial correlation for pairs of positive C points with respect to their negative counterparts, at least when their mutual distance approaches zero, i.e., when they collapse into a vortex.

7.3.2. INDEX IMBALANCE: + + AND − − PAIR CORRELATIONS

Figure 7.3 presents the pair correlation function of C points for the cases in which both the singularities that constitute the pair have either positive (g^A_{++}, orange data) or negative (g^A_{--}, purple data) topological index. Note that in both cases only singularities with opposite handedness are taken into account, as the correlation of co-handed pairs is identical for ++ and −− pairs, and equivalent to that of phase singularities in scalar random waves (see Section 6.3.2). The two functions of Fig. 7.3 equally contribute to the pair correlation of C points with the same topological index and opposite handedness, as described in equation (6.5), with

$$g^A_{\text{same}}(r) = \frac{1}{2}\left[g^A_{++}(r) + g^A_{--}(r)\right]. \tag{7.4}$$

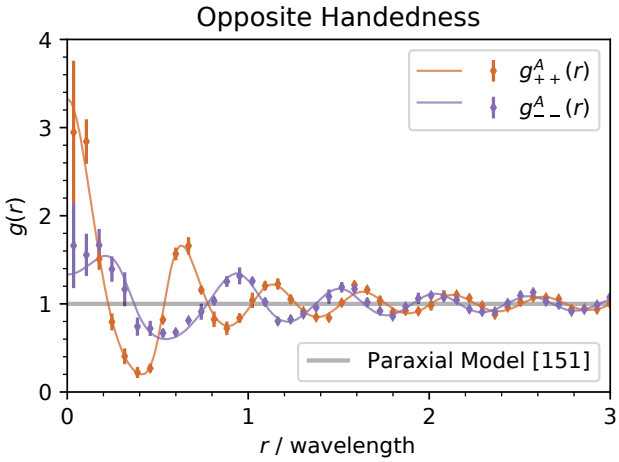

Figure 7.3: Pair correlation functions: $g^A_{++}(r)$ for pairs of C points with positive topological index (orange) and $g^A_{--}(r)$ for negative index pairs (purple). The data points with errorbars show our experimental data, the solid lines are our model for 2D random light fields. The solid gray line is the model for a paraxial random field [151].

Evidently, it makes a difference for pairs of C points to have positive or negative index, as it strongly influences their spatial arrangement. At very short distances ($r < \lambda/5$), g_{++} is significantly higher than g_{--}, by about a factor 2. This is consistent with the observation of a larger number of polarization vortices with positive rather than negative index. In the range where the displacement r among C points is between $\lambda/2$ and λ the behaviors of g^A_{++} and g^A_{--} are anticorrelated (correlation coefficient in that range ≈ -0.85). As the displacement is increased towards values of $r > 2\lambda$ the two correlation function start to coincide, as they will eventually do for $r \to \infty$.

A symmetry breaking in the behavior of topological singularities with opposite index is not common. From bare intuition there is no reason why a pair of entities with index -1 should behave differently from a pair of index $+1$. Similarly to what was shown in Chapter 6, this breaking of symmetry is a change in the behavior of C points that stems from confining a random field to propagate in 2D only. With this regard, it is important to recall that in a 2D slice of a 3D field, C points of opposite handedness would not exhibit any correlation, i.e., $g^A_{++} = g^A_{--} = 1$. Confining the random field in two dimensions breaks this degeneracy, encouraging pairs of positive C points to approach each other more than negative ones, and resulting in the observed imbalance in the total index of polarization vortices. We verify that this is the case by computing the theoretical expectations for g^A_{++} and g^A_{--} with the model described in Chapter 6 for a 2D transverse electric random field. The outcome of the model is plotted together with the experimental data in Fig. 7.3, represented by solid lines. The agreement between model and data is excellent. All the essential features discussed in the previous paragraph are accounted for by the model, and no additional ones are revealed.

7.3.3. SPATIAL TOPOLOGY OF STAR-STAR AND LEMON-LEMON PAIRS

Especially in relation to their index-dependent behavior, it is interesting to include the line classification of C points in the discussion. As detailed in Chapter 6, the index of C points is related to the topological properties of the director field around these singularities, with negative index singularities always being star-type, and positive index ones primarily being lemon-type. This line classification is related to the broken rotational invariance of the field topology around C points. Thus, we can associate a set of special directions around a C point. These are the directions along which the director of the polarization ellipse points towards the singularity core: three directions for star type and one for lemon type (see also schematic in Fig. 7.1). The question naturally arises whether these special directions play a role in the spatial arrangement of C points. If so, this could be one cause to the different behavior unveiled in the spatial correlations of $++$ and $--$ pairs of C points (Fig. 7.3). To answer this question we compute a new set of pair correlation functions, including a dependence on the displacement direction with respect to C point's directors.

Figure 7.4 presents the pair correlation $g(r,\theta)$ of C points as a function of the displacement direction θ. In computing a pair correlation function, the singularities displaced by a distance between r and $r+dr$ from a reference one are counted, averaging among all possible choices of the reference singularity (see also Chapter 3). In the case of the direction-dependent pair correlation functions in Fig. 7.4, we restrict the counting to the singularities contained in a circular sector of width $\pi/3$ around θ, where θ is the orientation of the displacement vector of a pair calculated with respect to the direction of the director of the reference singularity. For lemons (one director) the choice of this reference frame is unambiguous. For stars and monstars (three directors), we choose as a reference one of their three directors, at random.

The lemon-lemon correlation function in Fig. 7.4(a) displays a strong dependence on the displacement angle θ. Near $r = 0$, the data correspondent to small displacement angles (brown) is approximately 8 times as high as the one correspondent to $\theta \approx \pi$ (light orange). This means that among these closely spaced lemon-lemon pairs, a clear majority is oriented along the direction pointed by the singularity directors. Quantitatively, approximately 50% of of the pairs of lemons with displacement $r < \lambda/10$ are aligned within an angle $\pi/6$ with respect to the director of the reference singularity. Then, 35% of the pairs have either orientation $\theta = \pi/3$ or $\theta = 5\pi/3$. Finally, the remaining 15% are equally partitioned among $\theta = 2\pi/3$, $\theta = \pi$ and $\theta = 4\pi/3$. This analysis explains the circular pattern of the director field that surrounds positive polarization vortices (Fig. 7.1). For C point separations larger than λ the angular dependence vanishes, and all the correlation functions correspondent to different values of θ tend to coincide.

The analysis of the star-star correlation function [Fig. 7.4(b)] shows a much less clear dependence on the angle θ than the one displayed by the lemon-lemon pair correlation. Intuitively, given the fact that star-type C points have three directors instead of one, the dependence on θ of their pair correlation $g(r,\theta)$ could be expected to have a periodicity of $2\pi/3$, i.e., to the angle between the three directors of a perfectly symmetric star. We test this hypothesis by computing the correlations $g(r,\theta)$ for $\theta = n\pi/3$ ($n = 0,1,\ldots,5$) and plotting all the functions obtained for even values of n with the same color (dark purple), in contrast to that used for odd values of n (light purple). Figure 7.4 shows that

all the pair correlation functions correspondent to angles $\theta' = \theta + 2n\pi/3$ are indeed consistent with each other. On the contrary, some difference exists between the functions computed at $\theta_e = 2n\pi/3$ and those correspondent to $\theta_o = \theta_e + (2n+1)\pi/3$. This is especially visible in the region $r < \lambda$. The most evident observation here is that $g(r,\theta_o)$ almost vanishes at $r = 0.4\lambda$, while $g(r,\theta_e)$ stays close to unity. This indicates that at this particular separation stars tend to stay aligned to the direction of one of their directors rather than to avoid it. For $r < \lambda/10$ the differences among the correlation functions calculated for different values of θ have rather similar values. This means that stars, unlike

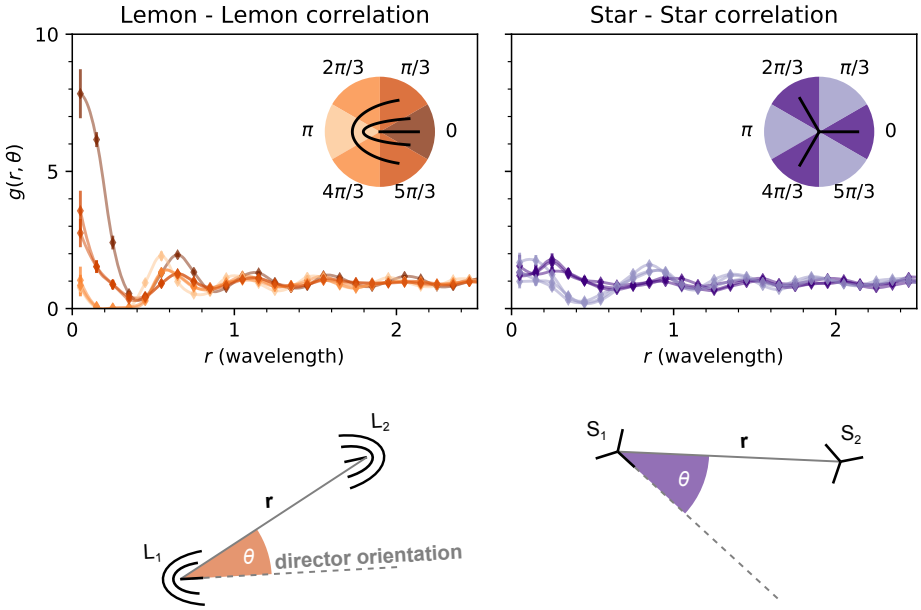

Figure 7.4: Pair correlation functions for positive index C points (upper left panel) and negative index C points (upper right panel), as a function of the displacement angle among the C points. The data points with different colors are the pair correlations for C points displaced within a given angular range with respect to the orientation of one (the) director associated to each singularity (see schematics below the main plots, and inset in the main plots for the color code). In the main plots, the lines are a guide for the eyes.

lemons, do not have a precise preferential alignment for their directors when their mutual distance approaches $r = 0$. In this regard, it is important to notice that a pair of stars superimposed while pointing at each other with one of their directors, or not, would in both cases lead to a four-pointed star shape for the director field which surrounds negative-index polarization vortices (Fig. 7.1).

Overall, the study presented in this Section for the pair correlation of C points in relation to their line classification, shows that the differences found between $g^A_{++}(r)$ and $g^A_{--}(r)$ also include a dependence on the topology of the director field around each singularity. For a C point to be a lemon (or a star) it influences its spatial correlation towards other lemons (or stars), in the way exemplified in Fig. 7.4. One might think that such topological properties could then be the reason of the imbalance between positive- and

negative-index vortices. One hypothesis is that it is easier for lemons pairs to approach at distance $r = 0$ than it is for stars pairs. However, we stress that the imbalance of vortices has to come from the fact that the random field in which all these singularities live is two-dimensional. In a 2D slice of a 3D field, C points would still be divided in stars and lemons, with the exact same topologies, and even with the exact same occurrence of each type as in the 2D field (see Chapter 6). But in the 3D case, pairs of C points with different handedness do not exhibit any correlation with respect to each other, turning all the curves in Figs. 7.3 and 7.4 into flat lines $g^A_{++}(r) = g^A_{--}(r) = 1$ (gray line in Fig. 7.3). Consequently, this fact undermines any argument intended to explain the imbalance of polarization vortices starting from the line classification of the pairs of C points from which they are generated.

Another interesting comparison is that of a TM field, still in 2D. As described in Section 6.6.1, the statistics of the C points in a TM field are completely equivalent to those of a TE field, both in index and handedness. However this is not the case for the absolute orientation of the C point directors, which is slightly rotated. This results in different topologies for the polarization vortices of a TM mode, especially for those with positive index, originating from lemons pairs. For a TM mode, these pairs tend to have their directors anti-aligned ($\theta \approx \pi$) when approaching mutual distances $r = 0$. Again, the fact that the different pairing topology found for the TM mode still maintains the same index imbalance for the polarization vortices as in the TE mode, confirms that the topology of the director field around C points does not have a direct relation with the index imbalance in polarization vortices, which must be sought in the two-dimensional nature of the field only.

7.4. CONCLUSIONS

In this chapter, we presented the experimental observation of higher order singularities of the polarization state of a random light field, known as polarization vortices. We discovered that polarization vortices in random waves exhibit a strong spatial correlation, with measured values for their pair correlation function reaching values larger than 4. Most interestingly, we discovered an imbalance in the total topological index of the detected vortices: about twice as many positive vortices were found than negative ones. We traced this observation back to the fact that C points with positive index are more prone to be found at a vanishing mutual distances than negative ones. Moreover, we found that at short distances positive C points (mostly lemons) prefer to align along the direction defined by the director of the singularity, while negative C points (stars) do not exhibit a clear preferential direction. As in Chapter 6, these observations find their explanation in the fact that a truly 2D (TE) random field is investigated, as no index imbalance is to be expected for a 2D slice of a 3D field. In fact, the model developed in Chapter 6 for 2D random fields perfectly describes our experimental findings. It is important to stress that the lower dimensionality and its resulting correlations among the vector field components is the underlying cause of the observations made in this chapter, in particular with respect to the analysis described in Section 7.3.3, which could inspire the development of a more universal description of the behavior of C points. Finally, we note that these results are quite general for the 2D case, as they apply to both TE and TM in-plane fields, with no relevant differences.

8

WAVELENGTH-DEPENDENT EVOLUTION OF C POINTS IN 2D RANDOM LIGHT

Second star to the right, this is the way
and then straight on, till morning
then you find the road by yourself
it leads to Neverland

[9]Edoardo Bennato

In this chapter, we study persistence and pairing statistics of C points in random optical waves as a function of the excitation wavelength, and compare them to the case of phase singularities. Even though C points of different handedness are correlated in space, anti-handed singularities do not appear to influence each other's evolution as a function of wavelength. We underpin this observation by computing the persistence statistics of C points, which behavior is highly similar to that observed for phase singularities in a single scalar component.

8.1. INTRODUCTION

In Chapter 6 we showed how the C points of a vector wave field can be considered as phase singularities in the projections of this field on a circular basis [139]. This suggests that the evolution of C points in random light might be understood by considering that of phase singularities in scalar random fields. In a situation in which the two circular components of the field ψ_l and ψ_r are independent [50, 151], also the two corresponding ensembles of phase singularities will have an independent evolution, exerting no influence on each other. Hence, in this case one expects the statistics of the evolution of C points to be exactly equivalent to those of these equivalent ensembles of phase singularities [51, 115]. However, as we demonstrated in Chapter 6, in two-dimensional random light ψ_r and ψ_l do exhibit correlations [139]. In particular we found spatial correlations between C points of different handedness, especially pronounced for singularities with the same topological index, but also present for opposite-index singularities.

In this chapter, we investigate the evolution of C points in two-dimensional random light when the wavelength of the wave field is varied. Regarding the persistence of these singularities in the light field we obtain statistics that follow the behavior found for phase singularities (Chapter 5). Moreover, we analyze the evolution of C points near the observation of a polarization vortex. We find that before and after being superimposed, C points with the same index typically diverge from each other, suggesting that polarization vortices are unstable in random waves.

8.2. EVOLUTION OF C POINTS AND THEIR STATISTICS

To study the evolution of C points in random light as a function of wavelength, we couple monochromatic light in the chaotic cavity and map amplitude, phase and polarization of the optical field in a square region 17 µm × 17 µm above its surface (see Chapter 6). We then repeat the measurement at different wavelengths of the input radiation with a step $\delta\lambda = 0.01$ nm (see Chapter 5). As in the case of phase singularities, the displacements of each C point are small enough to allow us to track them throughout their entire evolution. To perform the tracking computationally we exploit the same heuristic algorithm that was used in Chapter 5 [115].

Figure 8.1 presents three subsections of the total field maps for three different wavelengths ($\delta\lambda$ between each presented measurement is 0.02 nm). In the upper row of plots, we present the degree of circular polarization S_3/S_0, whereas the lower row displays maps of the orientation of the polarization ellipse. In all the plots, C points are highlighted by light-gray circles and dark-gray triangles, indicative of positive and negative topological indices, respectively. Green and purple insets inside the markers represent right/left handedness, respectively. By comparing the polarization maps measured at different wavelengths, we can appreciate how C points move with the tuning of this parameter. A quick analysis of the figure allows us to spot immediately one of the main differences with respect to the case of phase singularities: a pair of positive-index singularities that are able to approach each other when at very small separations. We record a total of approximately 25000 full trajectories, from creation to annihilation. The information contained in these trajectories allows us to investigate persistence and pairing statistics of C points with a good statistical significance.

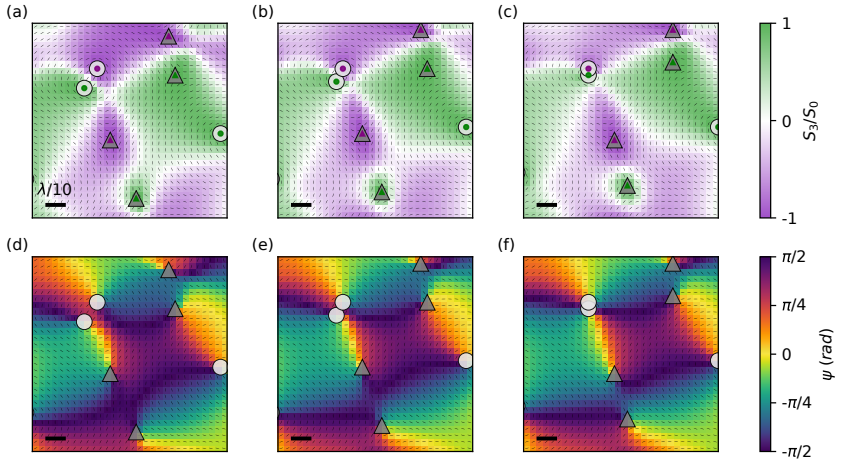

Figure 8.1: Evolution of C points as a function of light's wavelength ($\delta\lambda$ between the presented measurements is 0.02 nm). The first row of panels (a)-(c) displays a false-color map for the degree of circular polarization (s_3), at each input wavelength. The second row of panels (d)-(f) shows a false-color map for the orientation of the polarization ellipse (ψ), for each input wavelength. The black lines display this orientation angle, too. In all the figures positive-index singularities are depicted by white light-gray circles and negative-index ones by dark-gray triangles. A purple or green color in the marker is used to indicate left- or right-handedness, respectively.

8.2.1. PERSISTENCE AND LIFELONG FIDELITY

Figure 8.2 presents the histograms for the persistence of C points in the measured random field. The data points in the upper plot represent the number $\mathcal{N}$ of C points measured to persist in the field for a wavelength shift $\Delta\lambda$. At a first glance, the behavior is qualitatively highly similar to that observed for phase singularities. Indeed $\mathcal{N}(\Delta\lambda)$ exhibits an exponential behavior for $\Delta\lambda$ bigger than a cutoff wavelength shift λ^*. In chapter 5 we modeled this part of the behavior with an exponential decay $\sim e^{-\Delta\lambda/\lambda_c}$, with $\lambda_c = 0.6$ nm. In that case we performed measurements covering a wavelength range $\mathscr{L} = 1.2$ nm with a step $\delta = 0.02$ nm. The measurements presented in this chapter are instead for a range $\mathscr{L} = 1.5$ nm, with a step $\delta = 0.01$ nm. The difference in $\mathscr{L}$ slightly affects the finite-size effects due to the finite range of the wavelength scan, as $\mathscr{L}$ is contained in the correction factor $(1-\Delta\lambda/\mathscr{L})$ in front of the exponential (see Chapter 5). Additionally, this change influences the quality of the statistics, since the total number of measured trajectories increases for a larger range $\mathscr{L}$. When we plot the model discussed in Chapter 5 including the factors which are appropriate for this new set of measurements, we observe that it perfectly describes the trend corresponding to the long-living population of C points, but with $\mathcal{N}(0)$ twice as big as the one used for phase singularities. This finding suggests that C points of a given handedness are hardly influenced by the evolution of oppositely handed singularities. In fact, we find that the persistence histogram of C points in random light is equivalent that of two sets of independent phase

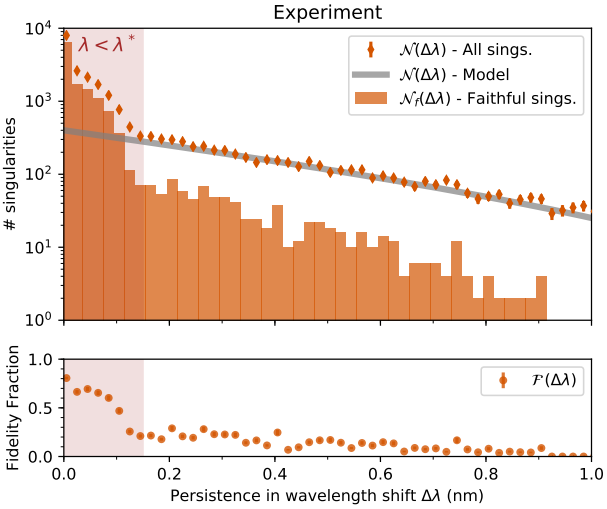

Figure 8.2: Histogram for the persistence of C points in random light. The errorbars in the upper plot represent the number $\mathcal{N}$ of singularities versus their persistence in the random field in wavelength shift $\Delta\lambda$. The boxes are the number $\mathcal{N}_f$ of faithful C points. These are C points that preserve their partner for both their creation and annihilation. In the lower plot we show the fidelity fraction $\mathcal{F} = \mathcal{N}/\mathcal{N}_f$

singularities in scalar random fields added together. These two sets, are the ensemble of phase singularities in ψ_r (left-handed C points) and that of ψ_l (right-handed C points). When considering their evolution as a function of wavelength, these two ensembles of oppositely-handed dislocations do not seem to affect each other's persistence. This independent behavior is expected for C points in 3D fields, where ψ_r and ψ_l can be completely independent from each other, but it is surprising in a 2D field, as in Chapter 6 we demonstrated how the spatial distribution of C points with different handedness exhibits a strong correlation. Clearly, this correlation in space does not have significant implications on the evolution of C points as a function of wavelength.

8.2.2. MIXING OF ANTI-HANDED C POINTS

In principle, C points with opposite topological index and handedness can be created and/or annihilated together, as two singularities with these characteristics can approach each other until their separation is zero [see Fig. 6.6(b)]. However, having observed that the evolution of C points is compatible with that of two independent sets of oppositely handed singularities, such a pairing seems to be discouraged. It is therefore interesting to investigate whether these events, that originate from singularities existing in oppositely handed projections of light's vector field, are actually taking place. Their occurrence can be checked by including the information on C points' handedness in their trajectories. In Fig. 8.3 we display the persistence histogram for C points in 2D random light, and directly compare it with the histogram for singularities that are created and

annihilated with anti-handed partners. In the upper plot, in orange the total number of singularities $\mathcal{N}$ as a function of their persistence in the field. In purple the number of singularities $\mathcal{N}_m$ which during creation and/or annihilation mix with a anti-handed C point. In general, we observe that $\mathcal{N}_m \ll \mathcal{N}$, at every wavelength shift $\Delta\lambda$. Moreover, the trend of $\mathcal{N}_m$ is highly similar to that of $\mathcal{N}$. In fact, when we compute the ratio between these two quantities (lower plot), this does not show any significant dependence on $\Delta\lambda$. The ratio $\mathcal{N}_m/\mathcal{N}$ is approximately 1.9% for all $\Delta\lambda$. This number can be interpreted as an upper limit for the number of singularities which can act as connections between the ensembles of right-handed and left-handed C points. It is an upper bound

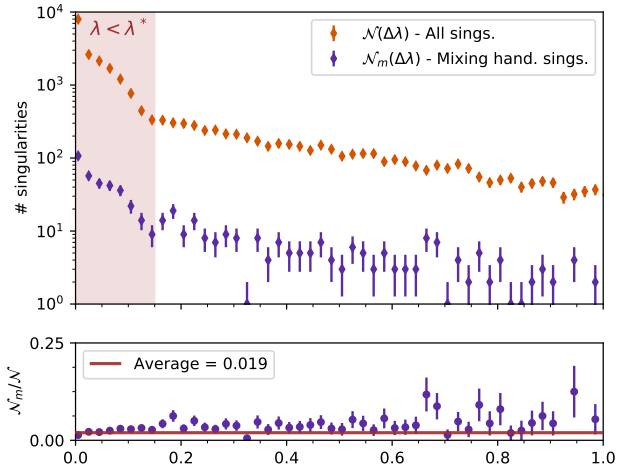

Figure 8.3: Histogram for the persistence of C points in random light. The data points in the upper plot represent the number of singularities versus their persistence in the random field in wavelength shift $\Delta\lambda$, for all the measured C points (orange) and for the subset of C points which are created and/or annihilated with a C points of opposite handedness (purple). In the lower plot the fraction of singularities which are created or annihilated with an oppositely handed partner ($\mathcal{N}_m/\mathcal{N}$), versus persistence in wavelength shift $\Delta\lambda$. The red line is the weighted average of these fractions.

due to our finite resolution. This can cause an overestimation of the number of events in which singularities of different handedness are created or annihilated. In fact, a pair that we detect to be created or annihilated could just be displaced by a distance smaller than our pixel size, without actually being involved in a creation or annihilation process. Nevertheless, this overestimation can not contradict the main outcome of the observations made in this section. The data presented Fig. 8.3 confirms that the vast majority of singularities with opposite handedness do not influence their mutual evolution.

Considering the creation/annihilation events of pairs of anti-handed C points opens an interesting line of reasoning in relation to the polarization vortices studied in Chapter 7. As a matter of fact, polarization vortices are also pairs of C points with opposite handedness. Here, we are considering events of similar nature, where instead of having two

dislocations with the same topological index, we consider the annihilation or creation among two opposite indices. Even though this event is not visualized as a higher order singularity with twice the index, it will still be a non-trivial location of the field, since two points of opposite handedness, therefore separated by an L line [6, 15], collapse onto the the same location.

8.2.3. C POINTS' TRAJECTORIES BEFORE AND AFTER VORTICES FORMATION

As we mentioned the case in which two C points with opposite handedness and same index lead to a polarization vortex, the question that arises naturally is how do these C points move just before and after creating the vortex. In Chapter 7, we illustrated how in 2D random light the occurrence of polarization vortices is enhanced with respect to a 2D slice of a 3D field. In two dimensions, pairs of same-index C points are found at a vanishing mutual distance with significant probability [139]. By varying the wavelength of the light field, we are now able to investigate the actual formation process of vortices as a function of an external parameter. In Fig. 8.4 we display in a 3D rendering two typical examples of the trajectory followed by two C points which merge into a polarization vortex. In theses images, the color of the trajectories indicates handedness (green for right-handed C points and purple for left-handed ones) and topological index (light colors for positive index, dark colors for negative). Only the two singularities which take part into vortex formation, with their creation and annihilation partners, are plotted with full opacity. All the other singularities passing through the observation window are plotted with a transparency of 0.9.

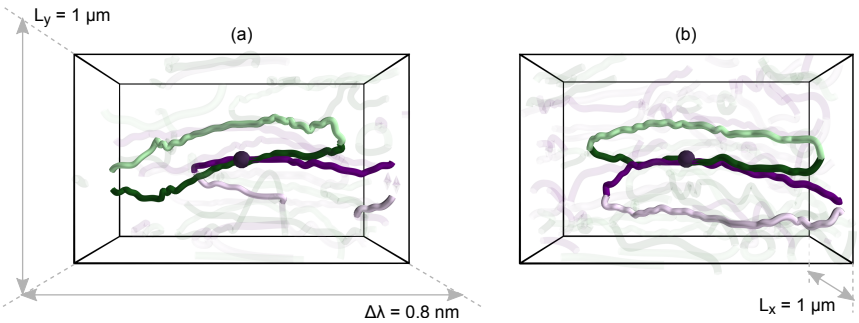

Figure 8.4: Example of the trajectories of C points in random light in correspondence of the observation of a polarization vortex. The black sphere highlights the formation of a polarization vortex. The color of the trajectories encodes topological index and handedness of C points: green is used for right-handed C points, and purple for left handed ones. Among these, light colors indicate positive topological index, while light colors are used for negative indices. We consider an observation window of 1 µm × 1 µm × 1 nm. The trajectories which are involved in the creation of the polarization vortex, with their creation/annihilation partners, are plotted in solid colors. All the other singularities propagating through the window are plotted with a transparency of 0.9.

Figure 8.4(a) presents a clear example in which the two C points that generate a vortex at the particular point in wavelength λ_v (black circle), are unbound from each other shortly after the vortex formation, and continue their trajectory independently. Instead, Fig. 8.4(b) illustrates the case in which the two same-index C points stay close to each other (distance $\ll \lambda/2$) as the wavelength is varied, intersecting their trajectories few

more times. An interesting observation to be made on Fig. 8.4(b), is that both C points terminate their existence as their trajectories diverge, after a wavelength shift that is smaller than the one for which the two C points remained at close proximity. This observation could suggest a sort of threshold behavior, which keeps the C points together until they are at a distance larger than a certain value l^*.

Seeking statistical significance, we now combine the information on the trajectories of C points in correspondence of every polarization vortex formation in our database (approximately 10'000 events). Figure 8.5 represents with a false-color map a 2D histogram for the C points displacement density around polarization vortices. To real-

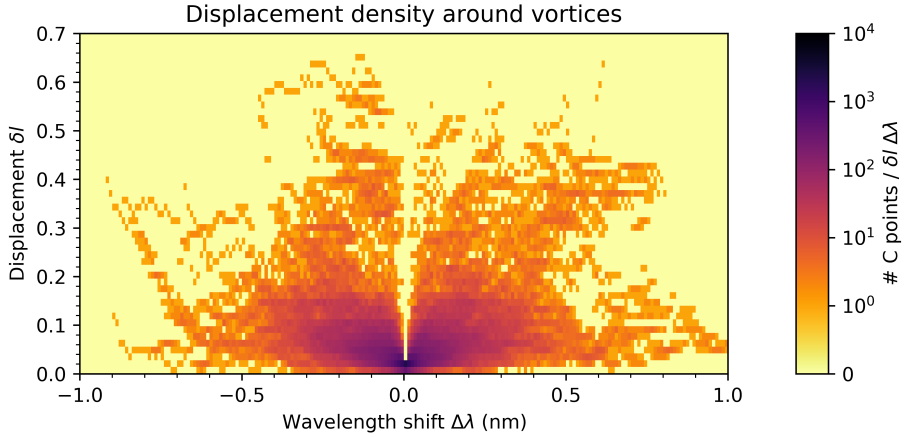

Figure 8.5: 2D histogram for the displacement of same-index C points, before and after they generate an optical vortex. On the x axis the wavelength shift is with respect to the one at which the two C points meet to form a vortex (wavelength shift = 0).

ize this two-dimensional histogram, we calculate the displacement δl between the two C points as a function of wavelength shift $\Delta\lambda$. We set the origin of the wavelength shift ($\Delta\lambda = 0$) to be the value λ_v at which the C points pair into a vortex. Subsequently, we combine in the histogram all the computed displacements $\delta l(\Delta\lambda)$. The color of each pixel of the false-color map represents the number of C points that at a wavelength shift $\Delta\lambda$ after vortex formation were displaced by a distance δl. We used a logarithmic scale for the color map to accommodate the large dynamic range in the measured number of C point displacements. In this figure we can see how our statistics degrade as the wavelength shift $\Delta\lambda$ or the displacement δl is increased, since fewer and fewer trajectories with those characteristics can be observed. While from a first analysis of Fig. 8.4 it is difficult to draw a definitive conclusion, it suggests that on average C points tend to diverge from each other before/after generating a vortex. This would again be consistent with a picture in which anti-handed C points undergo an independent evolution as the parameter is varied. Such a conclusion would be totally expected for a field in which the

right- and left-handed components exhibit no correlation, as it can be possible in a 2D slice of a 3D field. In truly 2D light, the independent behavior that we have observed appears surprising. In fact, in the two-dimensional case, anti-handed C points exhibit a strong spatial correlation, especially when they have opposite index (see Chapter 6). Concluding the analysis of Fig. 8.5, we note that a small asymmetry can be glimpsed in the histogram. This is that the cone-shapes that start from $\delta l = \Delta\lambda = 0$ seem to exhibit two lobes, suggesting two distinct behaviors of $\Delta\lambda$ *vs.* δl. However, at this stage the observation is not significant enough to exceed pure speculation.

8.3. CONCLUSIONS

In this chapter we analyzed the evolution of C points in random light, as a function of the wavelength. We compared this evolution to that of phase singularities in a scalar random field, and highlighted a one-to-one correspondence. As a matter of fact, the evolution of C points is equivalent to that of two sets of independent phase singularities: those of the right- and left-handed polarized fields. From a conceptual point of view this is in contrast with what found in Chapter 6 for the static distribution of C points in 2D random waves. In that case, a strong correlation among the differently handed polarization singularities was uncovered. Furthermore, we studied the case of the evolution of C points near the formation of a polarization vortex, which again emphasized the independent behavior of differently handed C points. It is an intriguing conclusion that C points of different handedness seem to ignore each other during their evolution, even though they have to keep satisfying the strict spatial correlation described in Chapter 6.

IV

Outlook and Conclusions

9

TIME EVOLUTION, EFFECTIVE INTERACTION AND PHASE TRANSITIONS

"In that direction," the Cat said, waving its right paw round, "lives a Hatter:
and in that direction," waving the other paw, "lives a March Hare.
Visit either you like: they're both mad."
"But I don't want to go among mad people," Alice remarked.
"Oh, you can't help that," said the Cat: "we're all mad here. I'm mad. You're mad"
"How do you know I'm mad?" said Alice.
"You must be," said the Cat, "or you wouldn't have come here."

[10]Lewis Carroll

Here we report a quick overview of some preliminary studies on singularities in random light of interesting new avenues of research. This involves how time-dependent fields can be related to monochromatic wave fields, and therefore how the time-evolution of singularities can be observed. Additionally, given the direct relation that exists in statistical physics among the pair correlation function $g(r)$ and the effective interaction potential $V(r)$, we set the stage for the definition of an effective interaction among phase singularities in random waves using a reverse-engineering method which takes the $g(r)$ as input. Finally, we address the fundamental question of how many waves are required to obtain a random wave ensemble, and show for the singularities different regimes which are reminiscent of the solid, liquid and gaseous state of matter.

9.1. TIME-DEPENDENT EVOLUTION OF PHASE SINGULARITIES IN RANDOM WAVES

In this thesis we have studied the evolution of phase and polarization singularities as an external parameter – the wavelength – was varied. One could wonder about the time evolution of singularities, but in monochromatic waves they are stationary. For instance, if we consider the case of phase singularities, the time-evolution operator simply acts as an additive phase factor. Clearly, adding any value to a point where the phase is undetermined does not change anything, and while their surroundings rotate in a vortical flow, phase singularities remain pinned to their locations. The key to visualize time evolution is the use of transients. The most natural example is a light pulse, of finite temporal width, which therefore contains more than a single frequency component. Creating a superposition of the different frequency components of such a pulse leads to a non-stationary field, and to the motion of phase singularities. Here, we pursue two different approaches in order to visualize this type of time evolution. The first approach is purely experimental, involving time-dependent near-field measurement in which a light pulse is coupled into the chaotic cavity instead of monochromatic light. The second method consists in reconstructing the time-dependent field starting from its frequency components. The direct measurement offers an intuitive picture of what the time evolution of the optical field in the chaotic cavity means, whereas the reconstructed frequency data offers more freedom in the tuning of relevant parameters.

9.1.1. DIRECT TIME-DEPENDENT MEASUREMENTS

Time-resolved near-field measurements are performed in complete analogy to frequency-resolved ones, except that light pulses are used. The signal measured in the cavity by the near-field probe is then combined with a fraction of the original pulse which was sent to the reference branch of our setup, and their interference is measured (see also Section 2.2.1). By varying the delay of the reference pulse with respect to the signal, it is possible to monitor the time evolution of the measured field [81, 183–185].

Figure 9.1 presents the near-field maps measured for the optical field H_z at different delay times t. At time $t = 0$ the light pulse is located approximately at the input waveguide of the chaotic cavity. Figure 9.1(a) displays the build up of random waves in the inner region of the cavity. In the first frame ($t = 750\,\text{fs}$) the light pulse has been reflected only few times by the edges of the cavity. The resulting field pattern is extremely anisotropic, qualitatively very different from what we typically observed for random waves (for several examples see Part II of this thesis). In fact this time range corresponds to the transient in which a random wave ensemble is being constructed by the pulse being multiply reflected. As the delay t between reference and signal is increased, we access time regions for which the input pulse has been reflected more and more times inside the cavity, and the resulting field pattern starts exhibit the typical features of a random wave field. These consist in the speckle-like pattern of alternating locations of high and low intensity, concealing a multitude of phase singularities. If we compute the density of singularities from the measured maps, and compare it to the value expected for a random wave ensemble, we can conclude that the random regime is reached at $t \approx 1200\,\text{fs}$. Figure 9.1(b) shows four consecutive frames ($\delta t = 25\,\text{fs}$) in the

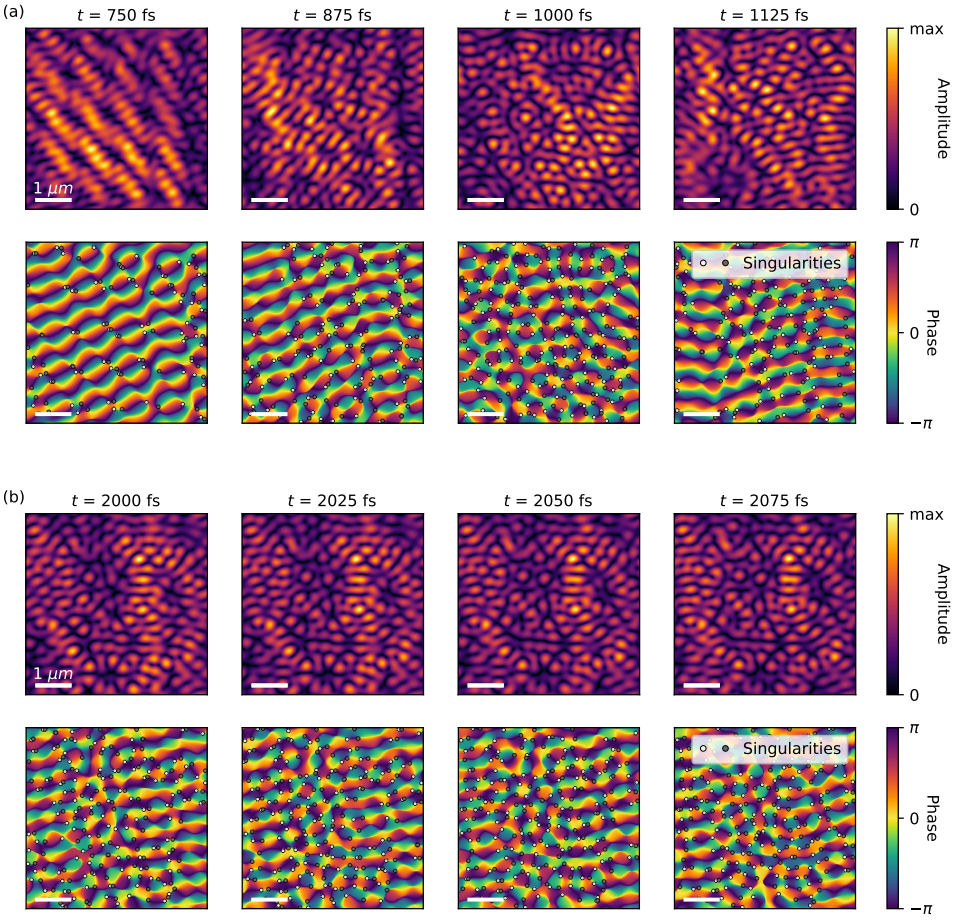

Figure 9.1: Evolution of the optical field in the chaotic cavity as a function of the time delay between the pulse input in the cavity and the reference pulse. These plots show the transient non fully random dynamics which takes place as soon as the pulse enters the cavity. The upper row of plots displays the amplitude of the optical field in a square region in the center of the chaotic cavity. The lower row exhibits the phase for the same square region above. Phase singularities are pinpointed by dark/light gray circle for negative/positive topological charge. The figure aims at giving an overview of the transient, so we only show one every five of the measured frames, resulting in a time step of 125 fs. (b) Evolution of the optical field in the chaotic cavity as a function of the time delay between the pulse input in the cavity and the reference pulse. These plots illustrate the evolution after the transient dynamic of Fig. 9.1(a), and are structured in the same way. This figure aims at illustrating the fine dynamics of the field and its singularities once the random regime is reached. Therefore we show consecutively measured frames, with a time step of 25 fs.

random regime. In the zoomed-in maps of the phase of the field we observe that its singularities move as time progresses. Creation and annihilation events are observed as well. On this data, we can use the same tracking procedure as the one used in Chapters 5 and 8 for the wavelength-dependent evolution and describe the dynamics of phase singularities in random waves.

9.1.2. CONSTRUCTING THE TIME DEPENDENCE FROM SINGLE-FREQUENCY MEASUREMENTS

A second useful way of obtaining a time-dependent representation of the optical field in the chaotic cavity, is to exploit the Fourier relation which connects such time-varying field to its single frequency components [186]. In general, we can write

$$\mathbf{E}(\mathbf{r},t)=\int_{-\infty}^{+\infty}d\omega\,\tilde{\mathbf{E}}(\mathbf{r},\omega)e^{i\omega t}, \tag{9.1}$$

where $\mathbf{E}(\mathbf{r},t)$ and $\tilde{\mathbf{E}}(\mathbf{r},\omega)$ are the electric field at position $\mathbf{r}$ and at time t or frequency ω, and the integral spans all possible frequencies. For an adequate comparison to the direct measurements of the light pulse propagating in the cavity discussed in Section 9.1.1, we need to include the spectral shape of the pulse in Eq. (9.1). We can assume the shape of the pulse to be a Gaussian,

$$\mathscr{P}(\omega)=\exp\left[-\frac{(\omega-\omega_0)^2}{2\,\sigma_{\mathscr{P}}^2}\right], \tag{9.2}$$

where ω_0 is the central frequency of the pulse and $\sigma_{\mathscr{P}}$ its spectral width. Including this term in Eq. (9.1), we obtain the expression of the time evolution of the random field generated by a pulse with spectral shape $\mathscr{P}(\omega)$:

$$\mathbf{E}^{\mathscr{P}}(\mathbf{r},t)=\int_{-\infty}^{+\infty}d\omega\,\mathscr{P}(\omega)\mathbf{E}(\mathbf{r},\omega)e^{i\omega t}. \tag{9.3}$$

This ideally requires the knowledge of $\mathbf{E}(\mathbf{r},\omega)$ for every value of ω. Since we will use our single-frequency measurements to construct $\mathbf{E}^{\mathscr{P}}$, we have to rewrite the formula in its discrete approximation [172],

$$\mathbf{E}_{\Delta}^{\mathscr{P}}(\mathbf{r},t)=\sum_n \Delta\omega\,\mathscr{P}(\omega_n)\mathbf{E}(\mathbf{r},\omega_n)e^{i\omega_n t}, \tag{9.4}$$

and given that we performed the near-field measurements by performing a wavelength sweep, we express the formula as a function of wavelength,

$$\mathbf{E}_{\Delta}^{\mathscr{P}}(\mathbf{r},t)=\sum_n |J(\lambda_n)|\Delta\lambda\,\mathscr{P}(\lambda_n)\mathbf{E}(\mathbf{r},\lambda_n)e^{i2\pi ct/\lambda_n}, \tag{9.5}$$

where $J(\lambda_n)=-2\pi c/\lambda_n^2$ is the Jacobian for the variable transformation from ω to λ. The discretization of the integral given in Eqs. (9.4) and (9.5) has consequences on the maximum time span T for which we are able to determine the reconstructed field. This will be inversely proportional to the wavelength step: $T=2\pi/\Delta\omega\propto 1/\Delta\lambda$. In fact,

$$\mathbf{E}_{\Delta}^{\mathscr{P}}(\mathbf{r},t+2\pi/\Delta\omega)=\sum_n \Delta\omega\,\mathscr{P}(\omega_n)\mathbf{E}(\mathbf{r},\omega_n)e^{i\omega_n t}e^{i\omega_n 2\pi/\Delta\omega}=\mathbf{E}_{\Delta}^{\mathscr{P}}(\mathbf{r},t), \tag{9.6}$$

which is easily verified by substituting $\omega_n = n\Delta\omega$ in Eq. (9.6), and exploiting the relation $\exp(2\pi i n) = 1$ for every integer n.

Another substantial fact to account for in our Fourier decomposition of the time-dependent field, is that we can measure a limited wavelength range rather than $[-\infty, +\infty]$. This limits our choice of pulse spectral widths, which cannot be larger than the measured wavelength range. The results presented in this chapter are obtained from two datasets of wavelength-dependent measurements. The first dataset contains measurements with a wavelength step $\Delta\lambda = 0.1\,\text{nm}$ which span a range $\mathscr{L} = 20\,\text{nm}$ ($10\,\mu\text{m} \times 10\,\mu\text{m}$ maps). The second dataset provides measurements with $\Delta\lambda = 0.01\,\text{nm}$ and $\mathscr{L} = 1.5\,\text{nm}$ ($17\,\mu\text{m} \times 17\,\mu\text{m}$ maps). The first dataset, with a longer wavelength range $\mathscr{L}$, enables us to simulate shorter pulses (pulse duration > 500 fs). This will come at the cost of a constraint on the total time T, limited by the larger wavelength step $\Delta\lambda$ ($T < 10^4\,\text{fs}$). Conversely, with the second dataset we are able to reconstruct the time dependent field for a longer time T ($T < 10^5\,\text{fs}$), but only for long pulses (pulse duration > 5000 fs). After constructing the time-dependent fields we pinpoint the singularities and track them in the same way as in Chapters 5 and 8 for the wavelength-dependent evolution.

9.1.3. LIFETIME OF PHASE SINGULARITIES AND CREATION RATE

So far in this thesis we considered the persistence of phase singularities in random waves as the wavelength was varied. Here, we will investigate their lifetime in a time-dependent random field. Figure 9.2 shows as an example two lifetime histograms which were obtained from our two different approaches. On the left, the result of the direct time-dependent measurements, on the right the result from the reconstructed field. Interestingly, in both cases the lifetime histograms exhibit an exponential distribution, as opposed to the biexponential trend observed for phase and polarization singularities (Figs. 5.3 and 8.2). By fitting the histogram of the direct time-dependent measurement, we obtain a typical lifetime $\tau = 250 \pm 20\,\text{fs}$. This number is comparable in magnitude to both the pulse width (FMHW $\approx 150\,\text{fs}$), and to the time that the pulse takes to travel across the cavity ($t_f \approx 400\,\text{fs}$). Usefully, we can combine the information of the time-

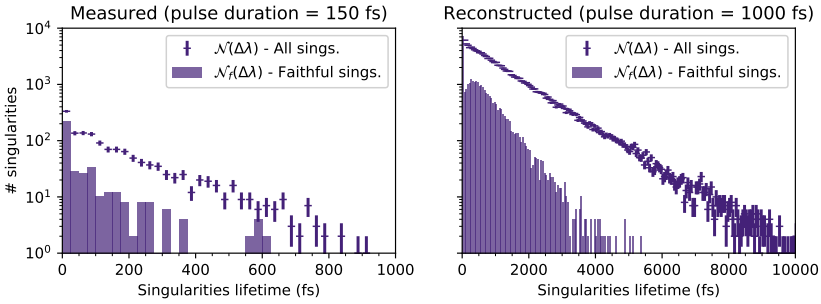

Figure 9.2: Lifetime histograms for phase singularities in time-dependent random waves. On the left, the case of a direct time-dependent measurement. On the right, one example resulting from the reconstructed time-dependence. The dashes are the measured number of singularities with a given lifetime in the field. The boxes are the number of lifelong-faithful singularities. Both plots derive from the analysis of the x component of the electric field.

dependent measurement with that of the time-reconstructed field, where we can study the lifetime of singularities for different pulse durations

Figure 9.3 presents the characteristic lifetime of the phase singularities arising in time-dependent random waves. This is computed as a function of the duration of the pulse used to compute the field in Eq. (9.5) (squares), or coupled in the cavity (star). The analysis is carried out for singularities arising in each of the Cartesian components of the in-plane electric field E_x (left panel) and E_y (right). In both cases, a clear correlation between lifetime of singularities and pulse duration is observed. The straight line in the plots is a linear fit [$l(x) = mx + q$] that we compute on the data, which results in slopes close to unity [$m_x = 1.00(2)$, $q_x = 140(20)$, $m_y = 1.14(2)$, $q_y = 150(20)$]. These fits give as result a non-zero intercept at zero pulse duration. This could be for a few different reasons. One possible explanation is that even if we consider an extremely short pulse, with extremely broad spectrum, still the eigenstates supported by the cavity will exist within a limited bandwidth. This bandwidth could be the result of the extrapolation performed in Fig. 9.3. However, at this stage we also cannot exclude the dependence to become non-linear in the range where the pulse duration is smaller than 500 fs, that we cannot access with our wavelength-dependent measurements. Nevertheless, it is evident that in the studied range the temporal width of the pulse is a strong contributor to the lifetime of singularities in the field.

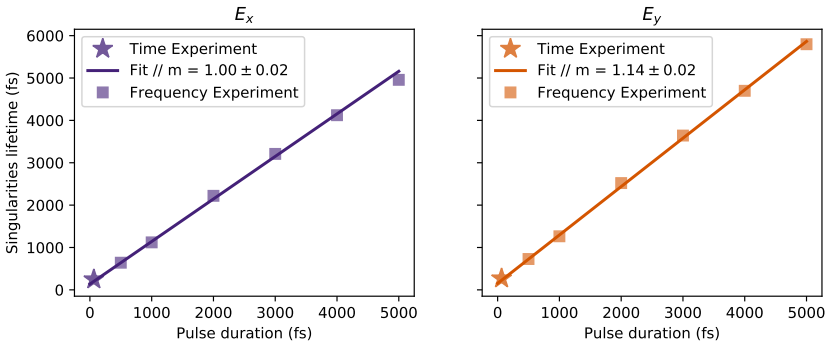

Figure 9.3: Lifetime of phase singularities in time-dependent random waves as a function of the time duration of the pulse that generates the wave pattern. The left panel presents the result corresponding to the x component of the field, and the right panel for the y component. The squares represent the data corresponding to the field reconstructed from the measured frequency-dependent field. The stars are the result from the direct time-dependent measurements. The solid lines are linear fit through te data.

Another observable, in principle related to the lifetime, is the event rate. This is the number of creations (or annihilations) of pairs of phase singularities that are observed during the time evolution of the field. Figure 9.4 presents the number of creations per unit time and per unit area visualized as a function of pulse duration. Clearly, the trend here is opposite to the one observed for the lifetime: the number of detected events decreases as the pulse duration increases. The analysis contains data combined from the two datasets used to reconstruct the time-dependent field starting from the frequency-dependent one (dark and light colors). The trend of event rates versus pulse width is linear in a log-log representation, indicating a power law dependence. We find the power

to be approximately equal to -1 [fitting with $f(x) = mx^{\alpha}$ yields $\alpha = -0.93(3)$]. The data corresponding to the two datasets are both well described by the same power law trend. When the pulse duration approaches 5000 fs the dataset with the smaller wavelength range and with finer wavelength resolution (S1fine) hits its limit of usability, and indeed we see that it starts to deviate from the fitted trend.

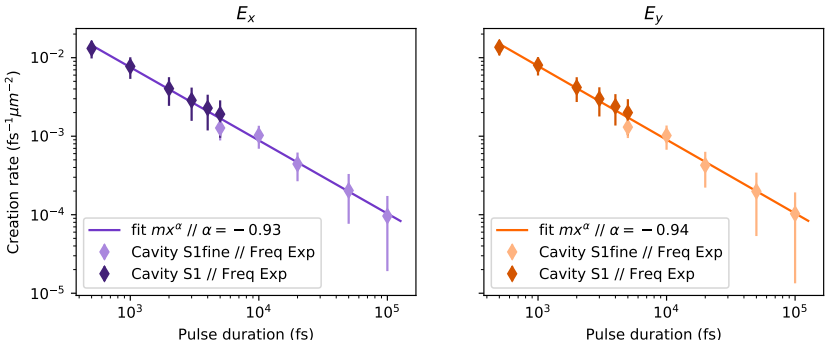

Figure 9.4: Event rates for phase singularities in time-dependent random waves as a function of the time duration of the pulse that generates the wave pattern. The plot is in log-log scale. The left panel presents the result corresponding to the x component of the field, and the right panel for the y component. The light-colored data points correspond to the field constructed starting from the measurements with the smallest wavelength step ($\delta\lambda = 0.01$ nm). The dark-colored ones correspond to the measurements with larger wavelength step ($\delta\lambda = 0.1$ nm). The solid lines are the best fit with a generic power law mx^{α}.

9.1.4. SOME REASONING ON EIGENSTATES AND PULSE DURATION

One interesting relation that can be made between this work and that presented in Chapter 5 is related to the eigenstate decomposition of the random field. In Chapter 5 we explained how the frequency-dependent field can be expressed as a superposition of the random eigenstates of the chaotic cavity, with a given central frequency and width. Such eigenstate properties were determining the persistence of phase singularities in the field as the wavelength was tuned. Particularly relevant to those studies, was the observation of two families of singularities with two different characteristic persistences, which we could trace back to two families of eigenstates contributing to the random pattern. It is interesting that we do not find an immediate equivalent of these two families in the time evolution of the singularities.

As described in Eq. (9.4), one single frame t in the time-evolution of the field, corresponds to the superposition of several states at different frequencies ω_n, weighted with the pulse spectrum $\mathscr{P}(\omega_n)$ and interfering with a phase term $e^{i\omega_n t}$. The sketch in Fig. 9.5 represents the typical scenarios that we considered in this Section, consisting of pulse durations of 150 fs, 500 fs and 5000 fs (from top to bottom). We compare these spectra to the eigenstates configurations discussed in Chapter 5, with two families of eigenstates with spacing $\Delta = 0.08$ nm, and spectral widths $\gamma = 0.16$ nm and $\gamma' = 0.04$ nm. From the figure, we can see that one single time frame contains contributions from several eigenstates of both families. As time progresses the coefficients with which such contributions are combined varies, but not their weights. The copious mixture might be the reason

why the consequences of having two families of eigenstates are not so evident in the time evolution of the field, and its singularities. The effects of the two populations might be concealed by the mixing of different frequency states that takes place in the time-dependent field. However, at this stage we cannot exclude that such effects might be disclosed by further analysis.

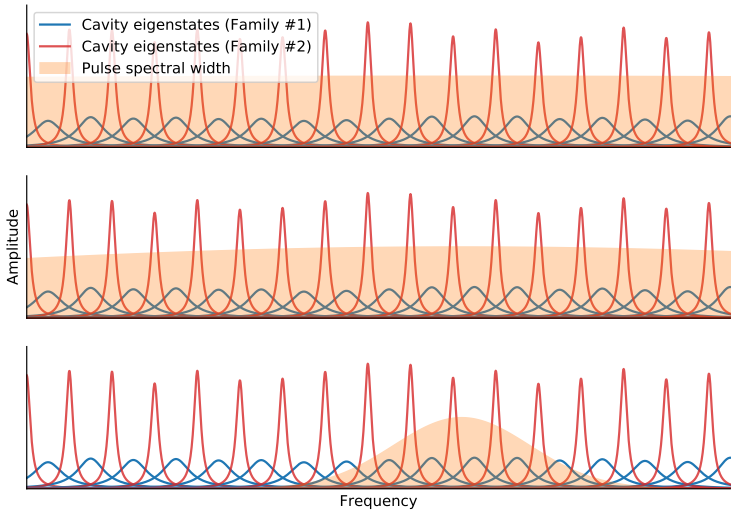

Figure 9.5: Graphical representation of the overlap between the pulse spectral width and the frequency eigenstates of the chaotic cavity. The three cases sketched in the figure are for pulse durations of 150 fs, 500 fs and 5000 fs (from top to bottom).

9.2. EFFECTIVE INTERACTION OF PHASE SINGULARITIES IN RANDOM WAVES

Throughout this thesis we have characterized the spatial distribution of optical singularities in random waves by using pair correlation functions (see Chapters 3, 6 and 7). This is, in fact, the natural way to characterize the spatial arrangement of ensembles of discrete entities [105]. While describing the properties of the measured pair correlations, we often drew analogies to those of systems of interacting particles, such as particles in a simple liquid [105]. The pair correlation function of a system is indeed directly related to the pair interaction in the same system. Known the pair interaction, one can easily predict the pair correlation with Monte Carlo simulations or even analytical calculations [105]. The opposite procedure is more difficult, since the relation between pair interaction and correlation is highly nonlinear [105].

Here, we use a reverse-engineering approach [164] to compute an effective pair-interaction for phase singularities in scalar random waves. Starting from their known pair correlation, we can in this way generate a fictive pair-interaction potential, which would generate an equilibrium configuration consistent with the input pair correlation. We perform this procedure in the canonical ensemble, i.e., for a fixed number of singularities in a given observation area. With this approximation, we are able to converge to a stable solution for the effective interaction among pairs of singularities, taking into account their charge. Performing a final Monte Carlo simulation using these pair interaction as an input we are able to reproduce the pair correlation expected for phase singularities in random waves, with excellent consistency.

9.2.1. DEFINITION OF THE PROBLEM

As point-like entities with a topological charge, it is tempting to think of phase singularities as of virtual particles with an effective interaction. Figure 9.6 shows how we can map a random wave field — with its amplitude and phase — onto a distribution of interacting particles through a set of discrete points, which are its phase singularities. Of course, in

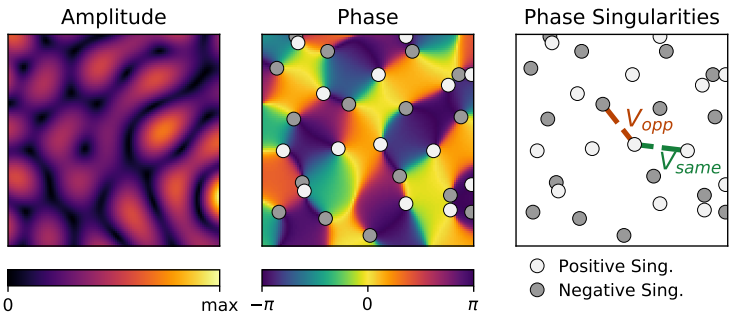

Figure 9.6: Amplitude, phase and singularities for a section of a calculated random wave field. The schematics in the third panel illustrates the effective pair interaction among singularities with the same (V_{same}) or opposite (V_{opp}) topological charge.

order for this to be true, the correct interaction needs to be provided. In this Section, we will retrieve such an interaction by exploiting the knowledge on the pair correlation of phase singularities in random waves. In particular, we will consider the model case of phase singularities in isotropic scalar waves [17].

9.2.2. REVERSE MONTE CARLO FOR POTENTIAL RETRIEVAL

Given the pair correlation function $g(r)$ of an ensemble of particles at their thermodynamic equilibrium, one can use various approximations to guess the underlying pair interaction. In a mean-field approximation for instance [105], the interaction would simply be given by

$$V^{\mathrm{mf}}(r) = -kT \log[g(r)]. \tag{9.7}$$

Note that as we do not have access to a parameter such as the temperature T, all the energies and interaction potentials that we compute will be expressed in units of kT, i.e., $kT = 1$. Although mean-field approximation can represent a good first step for a qualitative idea of the interaction in a system, it is a quite brutal approximation. Using it as the pair interaction to simulate the evolution of a system in a Monte Carlo simulation does typically not reproduce the expected equilibrium state, which should be consistent with the initial pair correlation $g(r)$.

One interesting approach to obtain the actual pair interaction $V(r)$ starting from a known pair correlation $g^{\mathrm{th}}(r)$, is to reverse engineer the problem of the Monte Carlo simulation. This procedure was already illustrated by Lyubartsev and Laaksonen [164] in the context of ionic liquids physics, and it consists of three main steps. As a first step, one needs to start a preliminary Monte Carlo simulation with a guessed interaction $V^{(0)}(r)$. Subsequently, when the final equilibrium configuration is reached, one can measure its pair correlation function $\langle g^{(0)} \rangle(r)$ and compare it to the known $g^{\mathrm{th}}(r)$. Based on the deviation $\Delta\langle g^{(0)} \rangle$ between the two distributions, the interaction potential $V^{(0)}(r)$ can then be corrected, to obtain $V^{(1)}(r) = V^{(0)}(r) + \Delta V^{(0)}(r)$. By iterating this process one can then calculate

$$V^{(j+1)}(r) = V^{(j)}(r) + \Delta V^{(j)}(r), \tag{9.8}$$

until $\Delta V^{(j)}(r)$ becomes negligible, and convergence is reached. The key step in this procedure is finding the correction $\Delta V^{(j)}(r)$, which was elegantly described to depend on the covariance of the measured pair correlation function [164]. Explicitly, it is convenient to introduce the function $S(r) = 2\pi r g(r)$ (valid for the 2D case), and expand it in its Taylor series,

$$\Delta\langle S^{(j)} \rangle(r_\alpha) = \sum_{r_\beta} \frac{\partial \langle S^{(j)} \rangle(r_\alpha)}{\partial V^{(j)}(r_\beta)} \Delta V^{(j)}(r_\beta) + O(\Delta V^2), \tag{9.9}$$

which omitting the terms of order $O(\Delta V^2)$ is a system of linear equations in $\Delta V^{(j)}(r_\beta)$,

with

$$\frac{\partial\langle S^{(j)}\rangle(r_\alpha)}{\partial V^{(j)}(r_\beta)} = \frac{\partial(r_\alpha)}{\partial V^{(j)}(r_\beta)}\left[\frac{\int dq\, S_q^{(j)}(r_\alpha)\exp\left[-\sum_{r_\gamma} V^{(j)}(r_\gamma)S_q^{(j)}(r_\gamma)\right]}{\int dq\exp\left[-\sum_{r_\gamma} V^{(j)}(r_\gamma)S_q^{(j)}(r_\gamma)\right]}\right] \tag{9.10}$$

$$= -\left[\langle S^{(j)}(r_\alpha)\, S^{(j)}(r_\beta)\rangle - \langle S^{(j)}(r_\alpha)\rangle\langle S^{(j)}(r_\beta)\rangle\right].$$

This procedure was validated for systems of particles in three dimensions, with and without the presence of a charge [164]. In presence of charge, it is convenient to split the problem in two subproblems. Firstly, particles with the same charge, pair correlation $g_{\text{same}}(r)$ and pair interaction $V_{\text{same}}(r)$. Secondly, particles with opposite charge, described by $g_{\text{opp}}(r)$ and $V_{\text{opp}}(r)$ [164]. This will be the case for a system of phase singularities in random waves, where the topological charge is relevant to the spatial distribution, and $g_{\text{same}}(r) \neq g_{\text{opp}}(r)$.

9.2.3. RETRIEVAL OF EFFECTIVE INTERACTION FOR PHASE SINGULARITIES IN RANDOM WAVES

With the recipe for the iterative procedure, we use the theoretical pair correlation function of phase singularities in random waves [17] to retrieve their effective interaction. We perform the retrieval considering in parallel both cases of same and opposite topological charge interaction. Typically the mean-field potential is a good choice as a starting guess of the interaction potential $[V^{(0)}(r)]$ [164]. Including the topological charge, there would be two mean-field potentials:

$$V^{\text{mf}}_{\text{same}}(r) = -\log[g_{\text{same}}(r)] \quad \text{and} \quad V^{\text{mf}}_{\text{opp}}(r) = -\log[g_{\text{opp}}(r)], \tag{9.11}$$

for same and oppositely charged pairs, respectively. However, for the case of phase singularities, this choice of using mean-field approximation does not lead to stable Monte Carlo simulations. We find that the main reason for this is the long-range correlations in the pair correlation functions, which result in long-range oscillations in the mean-field potentials $V_{\text{same}}(r)$ and $V^{\text{mf}}_{\text{opp}}(r)$. Truncating these oscillations by setting $V(r > r_c) = 0$ dramatically improves the convergence. Note that in our simulations we do not allow creation and annihilation of phase singularities with opposite topological charge, and therefore not allow for fluctuations of their density. Practically, we set the density of singularities to be equal to its theoretical average value [17]: $d = \pi/\lambda^2$, where λ is the wavelength of the wave field, which we set to unity for convenience.

Figure 9.7 presents an overview of the outcome of our iterative procedure for the retrieval of the effective interaction among phase singularities in random waves. The green and orange lines are the resulting potentials after each iteration j, changing from light to dark colors as j is increased (only one in every ten iteration is shown). On the left we depict the interaction potential among same-charge singularities, while on the right the interaction among oppositely charged ones is displayed. From both plots, we can observe how after a few tens of iterations the algorithm starts converging to a stable solution. Interestingly, the oscillations in $V(r)$ that we forcefully suppressed in the starting potential $V^{(0)}$, re-appeared as a result of the potential retrieval. In Fig. 9.7 we can

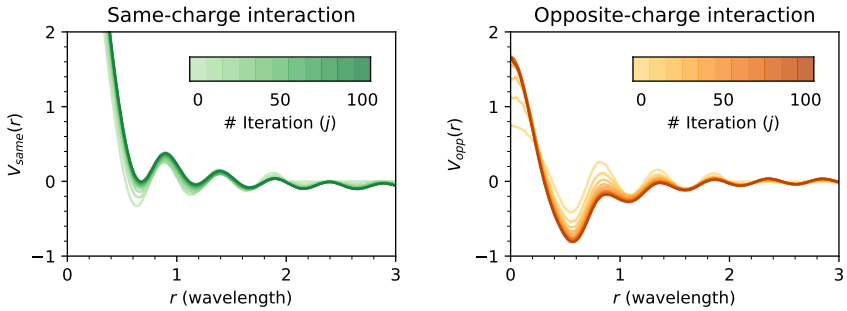

Figure 9.7: Overview of the retrieval of the effective potential between same-charge (left) and opposite-charge (right) singularities. The color palettes in the inset of the plots represent the iteration number, from light colors ($j = 0$) to dark ones (up ot $j = 100$).

see how for the lighter colors (first iterations) $V(r > 2) = 0$, due to the initial truncation. The differences between the mean-field potential and the final $V(r)$ are interesting, and they are actually crucial for the retrieved potential to reproduce the behavior of singularities in random waves. One clear difference in both $V_{\text{same}}(r)$ and $V_{\text{opp}}(r)$ is that the average value around which the potential oscillates as a function of r is not fixed at 0 as in the mean-field approximation. This average value decreases as r is increased for $V_{\text{same}}(r)$, whereas it increases with r for $V_{\text{opp}}(r)$. This is especially clear from the first dip in $V_{\text{same}}(r)$, which has been significantly lifted by the retrieval procedure. With respect to $V_{\text{opp}}(r)$, an additional clear difference implemented by the retrieval algorithm is the higher contrast between the first dip and its value at $r = 0$. In both cases of $V_{\text{same}}(r)$ and $V_{\text{opp}}(r)$, most of the changes happen in proximity of the first dip in the potential, which is indeed the most relevant as it dominates the nearest-neighbors interaction. It is not immediately obvious how to interpret the oscillations that follow the first dip, and it might be interesting to further investigate on this feature in the future. In this context it is important to point out that these oscillations can also be observed in the effective-interaction description of an ionic-liquid in a polarizable solvent [164].

The prime test to perform in order to verify the validity of the interaction potential that we computed in this section, is to perform a final Monte Carlo simulation based on this interaction, and to compare the equilibrium configuration of this simulation with the theoretical spatial distribution of phase singularities in random waves. Figure 9.8 directly compares the pair distribution functions computed on the outcome of the Monte Carlo simulation with the theoretical curves $g^{th}(r)$, for both same-charge and opposite-charge singularities. In both cases we acknowledge a very good agreement, certifying that the retrieved potential is the one that can reproduce the spatial correlation of phase singularities in random waves.

We demonstrated how phase singularities in random waves can be thought of as of interacting particles, not only qualitatively, but also quantitatively. The results of this section are shown for the prime example of singularities in isotropic random waves, well known system already for a few decades [17]. It is important to emphasize that

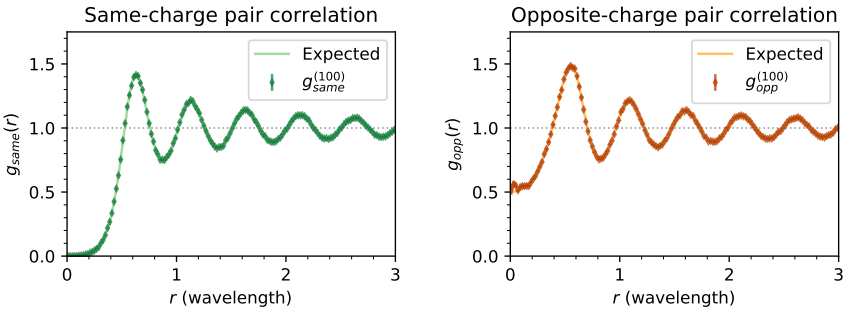

Figure 9.8: Pair correlation function measured at the iteration $j = 100$ (data points), in direct comparison with the expected theoretical functions (solid lines). In the left panel the correlation for same-charge singularities and in the right panel the correlation of opposite-charge ones .

the method shown here is general, as it only requires a knowledge of the pair correlation functions $g(r)$. This is essential in the context of this thesis, since here we uncovered different behaviors for singularities than the classic one of isotropic random waves. In Chapter 3 we found anisotropic distributions for the phase singularities arising in the vector components of a random light field, and in Chapter 6 we showed that polarization singularities invert their behavior with respect to charge in case of 2D confinement. All of these properties, can now be mapped into interaction potentials, possibly offering further insights on the role of singularities in wave fields.

9.2.4. SUPPLEMENTARY INFORMATION

MONTE CARLO SIMULATIONS

At every step j of the potential retrieval procedure described in this Section, we perform a full Monte Carlo simulation of the system, based on the interaction potential $V^{(j)}(r)$. Given this pair interaction of the system, we run a Monte Carlo simulation to compute its final state at equilibrium [111]. We do this in the canonical ensemble, i.e., with a fixed volume and a fixed number of particles. The simulation is initiated by distributing the particles in an ordered configuration with some Gaussian noise. The simulation area is a square region of side $L = 10$ (wavelength = 1), containing 314 particles, with periodic boundary conditions. Subsequently, the simulation is carried by proposing at each Monte Carlo step MCS_n a displacement Δr for the particle at r_i. We compute the difference in energy ΔE corresponding to this change

$$\Delta E = \sum_{k \in \text{system}} \left[V^{(j)}(r_i + \Delta r - r_k) - V^{(j)}(r_i - r_k) \right], \tag{9.12}$$

and accept the change with a probability

$$p_{\text{acc}} = \min \left[1, \exp\left(-\frac{\Delta E}{kT} \right) \right]. \tag{9.13}$$

This procedure is known as the Metropolis algorithm [111]. The total energy of the system is monitored after each Monte Carlo step, and it is used to determine whether the equilibrium configuration is reached, which is when this parameter does not exhibit significant changes rather than statistical fluctuations.

CONVERGENCE OF THE RETRIEVAL PROCEDURE

As a way to quantify the convergence of our iterative algorithm, we consider the total residual $R[g^{(j)}]$ of the observed pair correlations $g^{(j)}(r)$ with respect to their expectation values $g^{\text{th}}(r)$:

$$R[g^{(j)}] = \frac{1}{N_\alpha} \sum_{r_\alpha} \frac{|g^{(j)}(r_\alpha) - g^{\text{th}}(r_\alpha)|^2}{\sigma[g^{(j)}(r_\alpha)]^2}, \tag{9.14}$$

where N_α is the available number of discrete radii r_α, and $\sigma[g^{(j)}(r_\alpha)]$ the uncertainty on each observed $g^{(j)}(r_\alpha)$, estimated with the standard deviation on independent samplings of the equilibrium configuration of the Monte Carlo simulation. Figure 9.9 shows the total residual R for each iteration j. As we can see, a reasonable convergence is already obtained for $j \approx 60$.

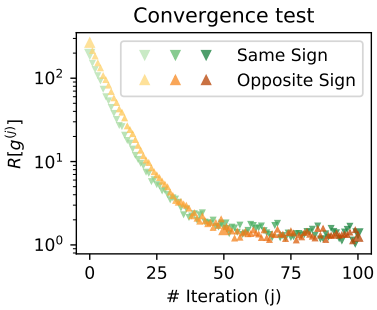

Figure 9.9: Convergence test for the iterative procedure. The plot shows the average residual $R[g^{(j)}]$ between measured and expected pair correlation functions at every iteration j, for both same- and opposite-sign singularities.

9.3. PHASE SINGULARITIES IN GENERIC WAVE FIELDS: FROM ORDER TO DISORDER

In almost every chapter of this thesis we modeled a random wave field as a superposition of plane waves with uniformly distributed random phases, as in Berry's hypothesis [138]. This hypothesis allows for straightforward numerical calculations of random wave fields by adding a set of plane waves with isotropic propagation direction and random phases. However, when calculating such field in practice, the question naturally arises as to how many waves one needs to add in order to have a fully developed random wave ensemble. Where is it, if there it is, the transition from non-random to random, is a fundamentally interesting question. The field pattern obtained by adding a limited number of waves, can in fact be clearly non-random, i.e. ordered, creating a big contrast with the random fields illustrated in this thesis. With an approach consistent with the rest of this thesis, we face this question by analyzing the impact that varying the number of waves constituting the field has on its phase singularities.

9.3.1. SINGULARITIES DISTRIBUTION *vs.* NUMBER OF WAVES

As zeros of the field, phase singularities arise from wave interference. One single plane wave does not have any zero, whereas the interference of two waves in the same plane produces lines of vanishing intensity. Instead, when three waves interfere, points of zero intensity are generated, and with them phase singularities. Figure 9.10 presents the amplitude of the wave field that is obtained by interfering three plane waves isotropically in a plane. Specifically, for the case of three waves this means that the propagation direction of each wave is rotated by $2\pi/3$ with respect to the subsequent one. Although the phase of each of these waves is a random number, the pattern is clearly not random. The symmetry of the wave propagation direction distribution results in an interference pattern that is reminiscent of a crystalline structure with hexagonal symmetry. As we increase the number of interfering waves to 5 (Fig. 9.11), we observe a situation in which the presence of an overall order is still present, as we can find the same pattern repeated in different location of the wave field. However, the five-fold rotational symmetry of the wave propagation direction distribution can not lead to a crystalline structure, as five-fold symmetry does not allow it [187]. The pattern obtained is highly similar to structures known as quasi-crystals [188]. The interference of 6 waves instead allows again for hexagonal symmetry, and it leads to crystal-like configurations. Interestingly, these configurations can differ quite a lot when using different random number for the phase of each contributing wave (Figs. 9.12 and 9.13). Patterns reminiscent of quasi-crystal are again obtained when interfering 7 (Fig. 9.14), 9 and 12 waves (not shown). Eventually, if we keep increasing the number of interfering waves, we realize a pattern consistent with the random wave model, in which no traces of short-range or long-range order can be found. This is the case in the example in Fig. 9.15, where 100 waves are used. In fact, the field pattern obtained with such number of waves is and qualitatively similar to the ones studied in Chapters 3, 4 and 5 of this thesis, with speckle-like features.

Observing the spatial distribution of the singularities which arise in these wave fields invites a comparison to condensed matter systems. In fact, in the case of 3 waves inter-

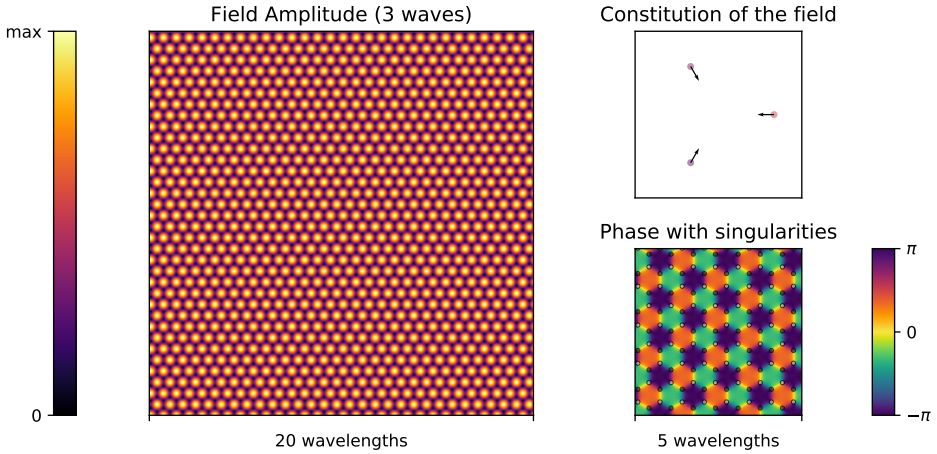

Figure 9.10: Field pattern resulting from the interference of 3 waves. On the left a false-color map for the amplitude of the field. On the top right a graphical representation of the waves that contribute to the pattern. The colors of the circles in this last plot represent the phase of each wave, and the arrows the propagation directions. On the bottom right a zoomed-in image of the phase of the field, with its singularities (dark/light circles).

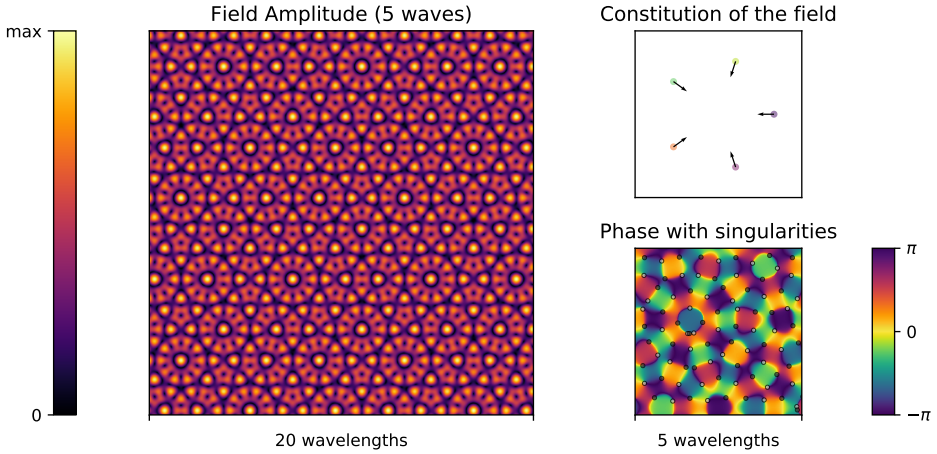

Figure 9.11: Field pattern resulting from the interference of 5 waves. On the left a false-color map for the amplitude of the field. On the top right a graphical representation of the waves that contribute to the pattern. The colors of the circles in this last plot represent the phase of each wave, and the arrows the propagation directions. On the bottom right a zoomed-in image of the phase of the field, with its singularities (dark/light circles).

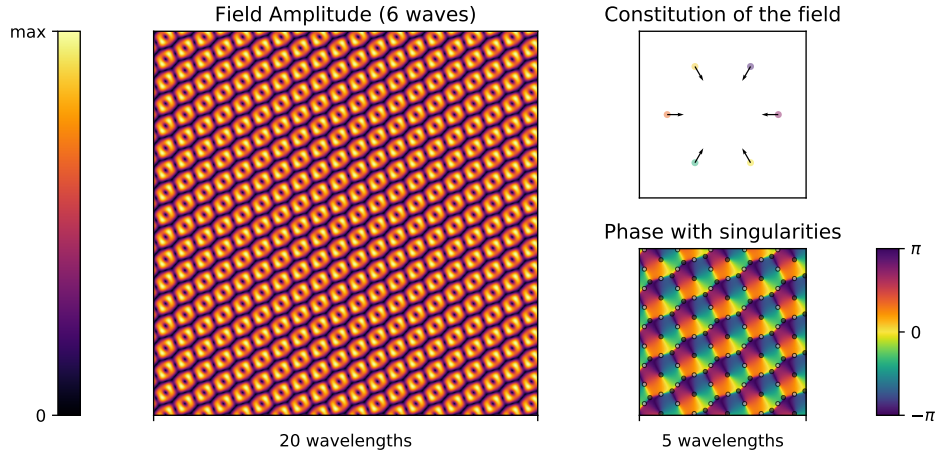

Figure 9.12: First realization of a field pattern resulting from the interference of 6 waves. On the left a false-color map for the amplitude of the field. On the top right a graphical representation of the waves that contribute to the pattern. The colors of the circles in this last plot represent the phase of each wave, and the arrows the propagation directions. On the bottom right a zoomed-in image of the phase of the field, with its singularities (dark/light circles).

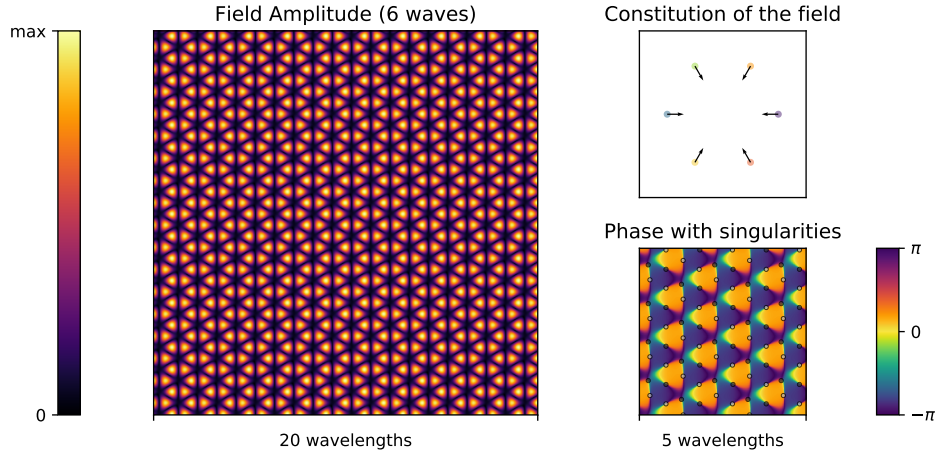

Figure 9.13: Second realization of a field pattern resulting from the interference of 6 waves. On the left a false-color map for the amplitude of the field. On the top right a graphical representation of the waves that contribute to the pattern. The colors of the circles in this last plot represent the phase of each wave, and the arrows the propagation directions. On the bottom right a zoomed-in image of the phase of the field, with its singularities (dark/light circles).

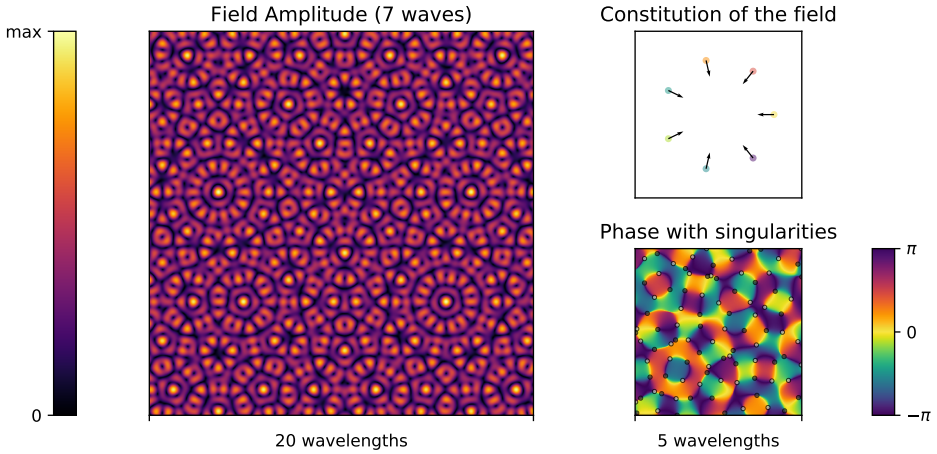

Figure 9.14: Field pattern resulting from the interference of 7 waves. On the left a false-color map for the amplitude of the field. On the top right a graphical representation of the waves that contribute to the pattern. The colors of the circles in this last plot represent the phase of each wave, and the arrows the propagation directions. On the bottom right a zoomed-in image of the phase of the field, with its singularities (dark/light circles).

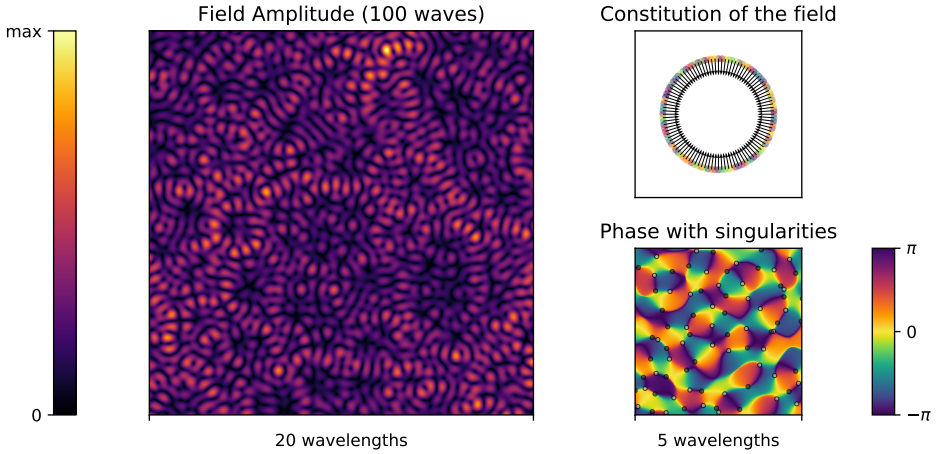

Figure 9.15: Field pattern resulting from the interference of 100 waves. On the left a false-color map for the amplitude of the field. On the top right a graphical representation of the waves that contribute to the pattern. The colors of the circles in this last plot represent the phase of each wave, and the arrows the propagation directions. On the bottom right a zoomed-in image of the phase of the field, with its singularities (dark/light circles).

ference the singularities arrange in a hexagonal lattice, for 5 waves they form a quasi-crystal and for 100 waves distribute in a liquid-like fashion. Despite the clear qualitative difference between the extreme cases, it is difficult to point a sort of phase transition. An additional difficulty is that the tuning parameter – the number of waves – produces abrupt changes in the arrangement of singularities from one step to the following. These changes are especially strong when the number of waves is limited, as the symmetry properties of the wave propagation distribution strongly influence the resulting field pattern.

The first observable we can study to describe the different fields in a simple way, is the spatial density of singularities in the generated wave fields. It is interesting to observe how this density varies as a function of number of waves, and compare it to the theoretical value expected for a random wave field, calculated by Berry and Dennis [17]. Figure 9.16 presents the spatial density of phase singularities in wave fields as a function of the number N of interfering waves (left plot). We observe that the density is highest for 3 waves, and it monotonically decreases towards an asymptotic value $d = \pi$. This asymptotic value is in fact consistent with the one predicted for phase singularities in random waves [17]. Each density in the plot was estimated by computing 100 indepen-

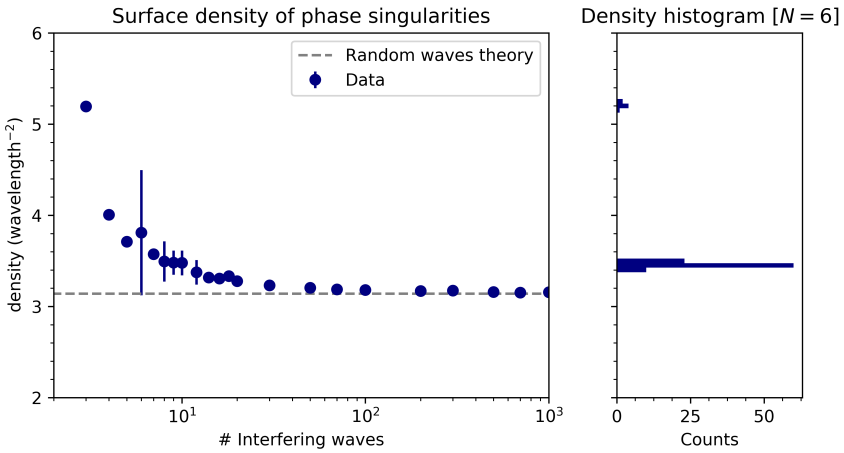

Figure 9.16: On the left, the density of singularities *vs.* the number N of waves that are used to produce the wave field in which the singularities arise. The data collected from simulations (circles) are compared with the theoretical value for random wave fields [17] (dashed line). On the right, a histogram (horizontal histogram) for the density corresponding to $N = 6$, which exhibits a bimodal distribution.

dent realizations of the wave field for each value of N. We then calculated the average density from this realization (circles), and the corresponding standard deviation (error-bars). The standard deviation gives an idea of how much variation in density there can be among different realizations of the wave field, e.g., for different choices of the random values for the phases of each contributing wave. The most interesting case is the $N = 6$. For this configuration of the wave propagation direction the density fluctuations among different realizations are bigger than in any other case. Analyzing more in detail this case

by considering the probability distribution of observing a given density, we observe that $N = 6$ exhibits a bimodal distribution for the density of singularities, as displayed in the right panel of Fig. 9.16. Just varying the sequence of random numbers associated to the phase of each interfering wave, can produce dramatic changes for this field constituted by six waves (two examples in Figs. 9.12 and 9.13). Although at the moment we do not have a physical explanation for the reason of this phenomenon, it is intriguing to notice that the case $N = 6$ is somehow special, as the representation of this field in Fourier space is a perfect hexagon, in which two consecutive apexes are separated exactly by a distance $k = 2\pi/\lambda$, the wave vector amplitude.

9.3.2. A CONTINUOUS APPROACH TO INCREASE THE NUMBER OF WAVES

In the previous Section we observed an intriguing transition from an ordered to a disordered wave pattern as the number N of interfering waves was increased. In that case, we were tuning a discrete parameter, which does not allow to zoom-in into specific regions of this parameter space, as only integer values are possible. Moreover, due to the high symmetry of some specific cases, the results were dominated by the symmetry properties of the wave propagation direction distribution rather than by the number of interfering waves. Here, we pursue a different approach, trying to emulate an increasing number of waves in a continuous fashion. This approach represents an alternative to the one of Section 9.3.1, in which the tuning parameter can be varied more continuously. Moreover, we do not vary abruptly the symmetry properties between consecutive field configurations, as they all originate from a continuous perturbation of the case of three interfering waves.

We begin the study with the case of three interfering waves. Subsequently, we add to these a number ΔN of waves, but without redistributing of the original waves. Instead, the additional waves are normally distributed in an angular spread $\delta\theta$ around the original ones. $\delta\theta$ indicates the standard deviation of such normal distribution. We define $N_s = 3$ as the number of initial waves, and N_d as the number of times these waves are duplicated and spread out, so to have a total number of waves $N = N_s N_d$. At the same time, we define the angular spread as proportional to the number of duplicated waves, with a dependence

$$\delta\theta = \alpha\,(N_d - 1)^{\beta}.$$

In the calculations that we are going to show we used $\alpha = 0.005$ and $\beta = 2$. Additionally, we do not set all the waves amplitude to be the same, but we apply a coefficient a exponentially distributed around the starting angle, with a decay length proportional to the number of duplications,

$$p(a) = e^{-2/N_d}.$$

Regarding the phase, we initiate the N_s waves with a random value uniformly distributed in $0 - 2\pi$, and then we program the phase of each additional wave to be normally distributed around these values with a standard deviation

$$\delta\varphi = \eta\,\delta\theta^{\gamma}.$$

In our calculations we set $\gamma = 3$ and $\eta = 25$. All the parameters enumerated in this section were chosen after performing preliminary simulations, with the goal of achieving

non-zero, but smooth, field variations as a function of the tuning parameters. It might seem that the (discrete) number of waves is still the relevant parameter also for this study. However, here the number of waves is directly bound to their angular spread and decorrelation properties. This relation diminishes the discreteness of the tuning parameter, as adding more waves which preserve their original phase and propagation direction does not produce changes in the resulting interference pattern. What is varied continuously here is in fact the angular spread, and the related phase decorrelation.

As the angular spread $\delta\theta$ of the wave propagation direction approaches the separation of the three initial waves $\theta_s = 2\pi/3$, amplitudes get more homogeneous, phases get more uniformly distributed, and the system approaches the isotropic random wave configuration. When $\delta\theta \gg \theta_s$ the full random wave regime is reached. In Fig. 9.17 we can observe how this process takes place in the three exemplifying cases in which $\delta\theta = 0$, 0.245 and 12.005, from top to bottom. These cases correspond to a total number of waves $N = 3$, 24 and 150, respectively. Each figure presents 5 panels. On the left the pair correlation function of the phase singularities arising in the computed field. On the right, starting from the top a graphical illustration of the wave-composition of the field. Here each wave is represented with a colored circle and an arrow. The arrow represents the propagation direction of the corresponding wave, the size of the circle represents its amplitude, and the color its phase (same false-color map of the phase plot, from $-\pi$ to π). On the bottom the amplitude of the resulting field, on the top right its Fourier representation, and on bottom right a zoomed-in image of the field's phase with its singularities (light/dark markers for positive/negative charge). Going from top to bottom in Fig. 9.17 we see how the initial lattice of singularities gets deformed, and eventually scrambled into a liquid-like phase.

With this model we can naturally take a step further, and spread the wave contribution also radially in k space. This corresponds to varying the amplitude of the wavevectors around the initial value k_0. We do this in a similar way as with the angular spread. Given a wavevector spread δk, we create an additional number of waves according to

$$N_d^k = N_d \, (\delta k/\mu)^\nu ,$$

where N_d is the number of waves spread angularly, and N_d^k is the number of waves spread radially in k. In our calculations we use $\mu = 0.005$ and $\nu = 0.5$. Figure 9.18 presents an overview of this study, in analogy to what shown in Fig. 9.17. In this figure we present the cases in which $\delta k = 0.1$, 0.3 and 0.6 (from top to bottom). These correspond to a total number of waves equal to 2682, 4647 and 6570, respectively ($N_d = 200$). As δk is increased the wave pattern gets more and more randomized, as it starts missing the features associated with the only length scale of the system, the wavelength. Already in the top panel of Fig. 9.18, the pair correlation function $g(r)$ starts losing its features at $r > 2$ wavelengths. For $\delta k = 0.6$ (bottom panel in Fig. 9.18) we cannot really distinguish any significant trend as a function of displacement in the $g(r)$, which is consistent with a flat line equal to 1, reminiscent of an ideal gas state.

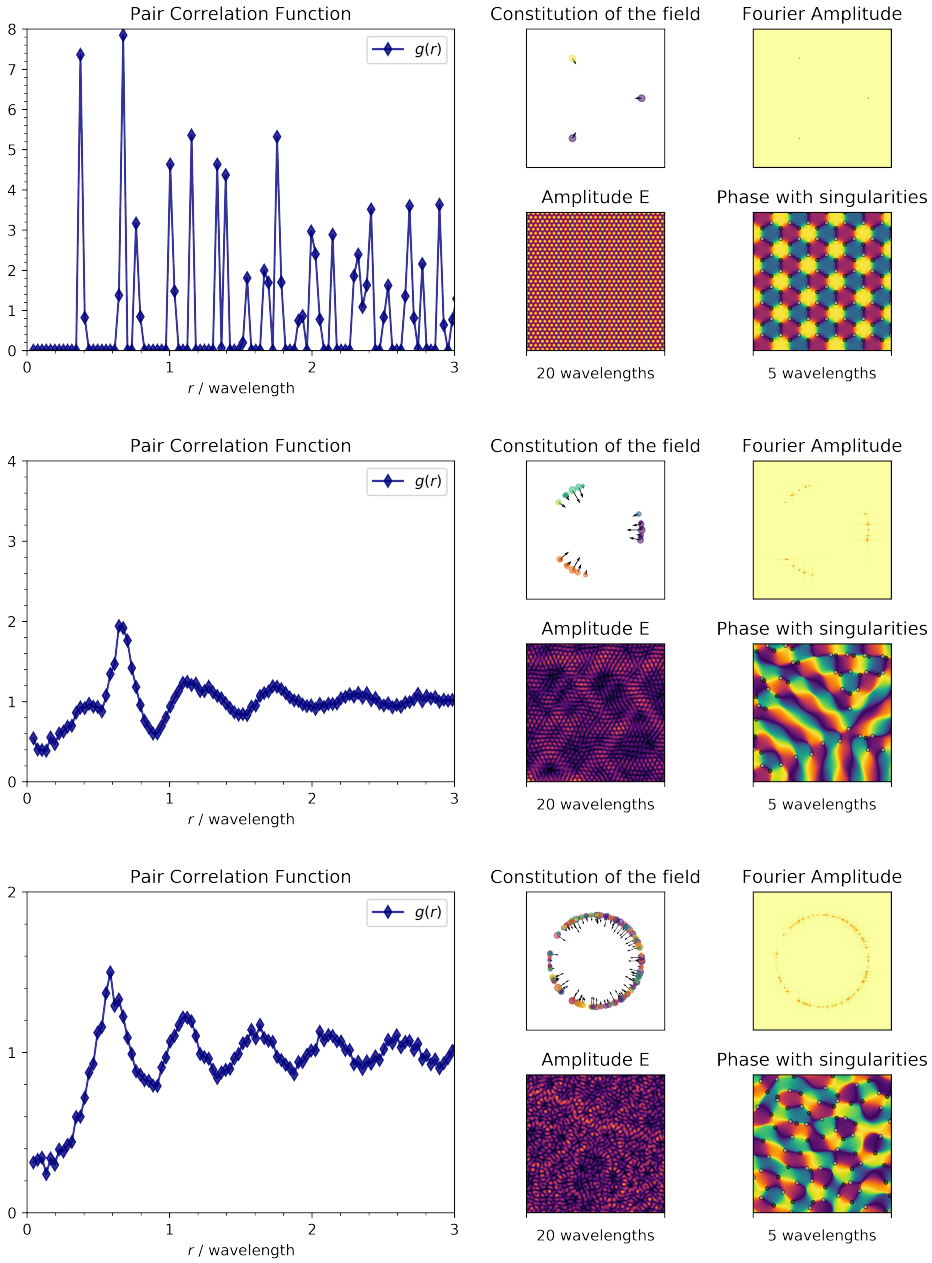

Figure 9.17: Overview of field patterns and their phase singularities for wave fields realized with different degree of angular spreads in the wave propagation direction (increasing spread from top to bottom). The figures are organized in a similar way as Fig. 9.10. Additionally, we show the pair correlation function of phase singularities (left panels), and the Fourier composition of the field (top right panels).

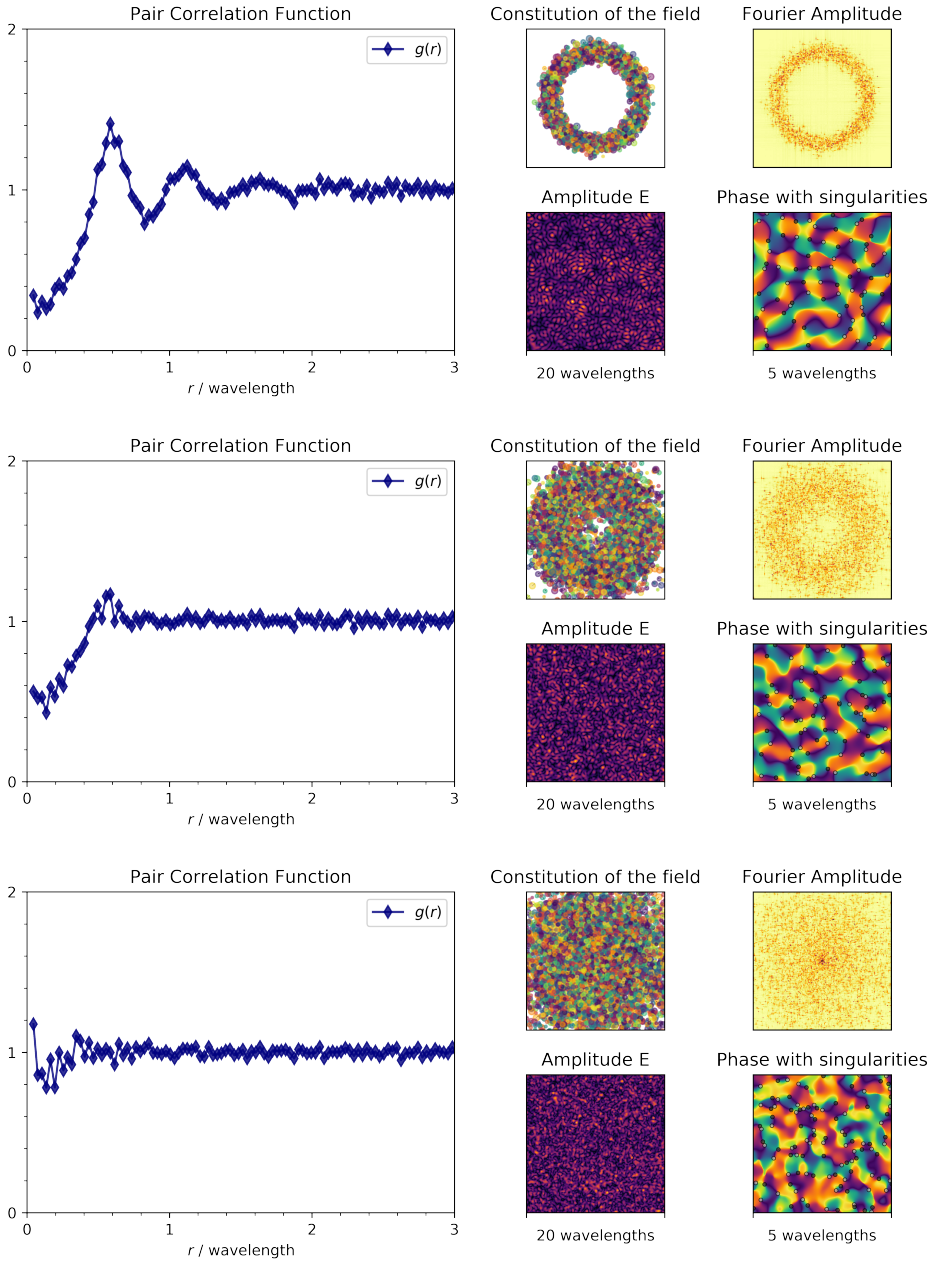

Figure 9.18: Overview of field patterns and their phase singularities for wave fields realized with different degree of wavevector's amplitude spread (increasing spread from top to bottom). The figures are organized in a similar way as Fig. 9.10. Additionally, we show the pair correlation function of phase singularities (left panels), and the Fourier composition of the field (top right panels).

Finally, in Fig. 9.19 we present a graphical impression of the pair correlation functions that we can compute at varying the two sets of parameters discussed in this Section. In the first part (red to white) we vary the angular spread, and in the second part (white to blue) the wavevectors amplitude spread. This figure offers a good overview on how we can obtain a continuous variation from crystalline-like, to liquid-like, and gaseous-like state of phase singularities in wave fields.

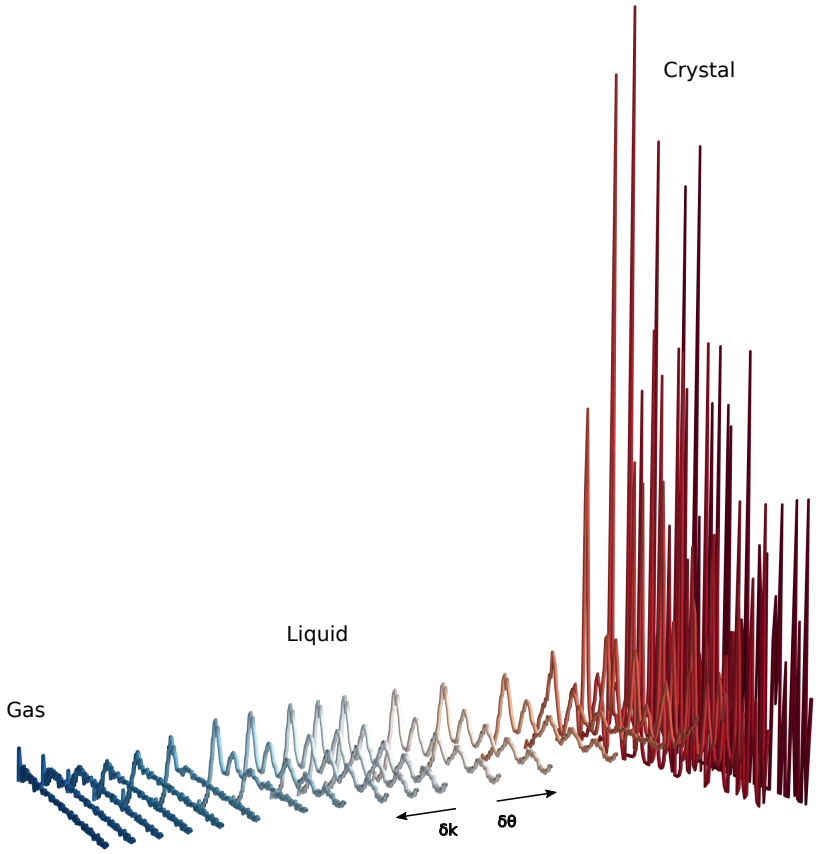

Figure 9.19: Pair correlation function of phase singularities in wave fields for different values of the tuning parameters described in Section 9.3.2. These are related to the number of interfering waves, which is increased in the tangential (red to white) and radial (white to blue) direction in k space (see also Fig. 9.17 and 9.18). The white curve correspond to the isotropic random waves model.

10

CONCLUSION

Let it go...

[11] Elsa

In this concluding chapter we briefly summarize this dissertation, and place it in a broader context as compared to the discussion in the individual chapters. Moreover, we relate our work to previous studies and current developments, also beyond the field of optics.

THIS thesis covered several properties of optical singularities, with a focus on their behavior in random light. The main approach was experimental, as we exploited near-field microscopy to study light fields confined to a planar chip. The ability to detect phase and polarization singularities allowed us to unearth a number of novel collective properties of these entities in random light. These were mainly caused by the full vectorial character of light, and by the dimensionality of the studied field that for the first time could be truly considered as two dimensional. For the key discoveries made in this thesis, we accompanied our experimental observations with theoretical modeling. This modeling often used the inspiring and foundational work of M. V. Berry and M. R. Dennis [17, 42] as starting point.

Scientific curiosity was the prime driving force for this thesis, especially in relation to the multidisciplinary connections that the study of optical singularities allows. More than once we drew a comparison between optical singularities and systems of interacting particles: in the spatial distribution of phase singularities of Chapter 3, in the analysis of topological screening of Chapter 4, and ultimately in the modeling of a fictive interaction among phase singularities of Section 9.2. It intrigued us to observe how mathematical entities defined in a generic random wave field could behave just as if they were interacting particles in a liquid-like system. Yet it was interesting to discern differences in behavior for different types of singularities, even though each of them reminiscent of liquid particles. The most striking example is the effective attraction of polarization singularities with the same topological charge. This was observed to occur in a truly two-dimensional random field rather than a two-dimensional slice of a three-dimensional field, as described in Chapter 6.

Besides fascination, the study of wave fields through their singularities revealed to be insightful as well. Describing the persistence of phase singularities in random waves required a certain eigenstate decomposition of the field. This was crucial in order to obtain the populations of the dislocations arising in such a field, as described in Chapter 5. Obtaining the same insight on the eigenstates through different means would have been hard. It is also important to recognize the potential role that such a methodology could offer to different areas of physics, and beyond. Indeed it is often the case that one has to deal with a big amount of data to analyze, in which spotting subtle correlations can be very difficult, and sometimes impossible. In this regard, the transition from the study of a massive complex field consisting of about one million pixels per frame, to the analysis of just a few thousands of singularities represents a significant leap. This thesis showed how hidden correlations in complex fields not only appear but sometimes stand out naturally in the properties of their singularities. We have shown how to interpret these properties, both in the singularities' spatial distribution (Chapters 3 and 6) and parametric evolution (Chapters 5 and 8).

Our findings on the spatial bunching of same-index C Points naturally prompted questions regarding the existence of higher order singularities, which forms the basis of Chapter 7. It was exciting to locate such higher order singularities in a random field, and to find that they exhibit a clear spatial correlation as well. To visualize a breaking of symmetry in the behavior of these singularities with respect to their topological charge was unexpected, and not yet fully understood. In fact, we have been able to justify our experimental findings by acknowledging a good agreement with our theoretical model

for two-dimensional random light. Still, an intuitive explanation of the asymmetry in formation of more positive rather than negative polarization vortices is lacking.

In a context broader than optics, topological singularities continuously attract the interest of the scientific community. This is partially due to the fact that singularities are points where mathematics fails to describe the quantity which we measure/describe, and as such they are intrinsically intriguing. However, it has been demonstrated more than once that their relevance can span beyond scientific curiosity. This is especially true in the field of biological physics, where topological defects in active matter allowed for a more straightforward understanding of the physical mechanisms underlying the complex dynamic processes which occur in biological systems [148, 189]. In the context of superconductivity, the discovery and formal introduction of vortices allowed for breakthroughs in the understanding of high-temperature superconductivity, which is still an exotic and not fully understood state of matter [190]. Also in optics, the relevance of topological singularities is now becoming established. Indeed singularities are now being used to intuitively design photonic and plasmonic structures which work efficiently, or display the desired properties [191]. In this framework, one of the most interesting outlook of our work will probably lie in the combination of what was presented in Section 9.3 for generic wave fields with the idea of repositioning singularities, as discussed in Chapter 5 and 8. In fact, by using the proper number of waves, propagating along specific directions and with suitable initial phases, one can build an engineered network of optical singularities, e.g. C points, in a two-dimensional platform. As a possible application, this network of maxima in the optical-spin density can be coupled directly on chip to systems which exhibit optical-to-electric spin conversion [27], with the potential to control such spins in space, and possibly in time.

At this stage it is difficult to say which part of this thesis will be the most relevant. Personally, the spatial bunching of same-index polarization singularities and their generation of patterns of polarization vortices is what amazed me the most. This thesis shows that light can still surprise us, especially when considering its singular aspects.

BIBLIOGRAPHY

[1] D. C. Lindberg and D. C. Lindberg, *Theories of Vision from al-Kindi to Kepler* (University of Chicago Press, Chicago, Illinois, United States, 1981).

[2] H. E. Burton, *The optics of euclid,* J. Opt. Soc. Am. **35**, 357 (1945).

[3] A. van Helden, S. Dupré, and R. van Gent, *The Origins of the Telescope* (Amsterdam University Press, Amsterdam, The Netherlands, 2010).

[4] *The double-slit experiment,* Physics World **15**, 15 (2002).

[5] M. Planck, *Ueber das gesetz der energieverteilung im normalspectrum,* Annalen der Physik **309**, 553 (1901).

[6] G. Gbur, *Singular Optics* (CRC Press, 2016).

[7] J. F. Nye and M. V. Berry, *Dislocations in wave trains,* Proc. R. Soc. Lond. A **336**, 165 (1974).

[8] M. V. Berry, in *Singular Optics*, SPIE Proceedings, Vol. 3487, edited by M. S. Soskin (SPIE-Int. Soc. Opt. Eng., Bellingham, WA, 1998).

[9] K. Knopp, *Singularities,* Theory of Functions Parts I and II , 117 (1996).

[10] J. W. Bruce, J. W. Bruce, and P. Giblin, *Curves and Singularities: a geometrical introduction to singularity theory* (Cambridge university press, 1992).

[11] R. Balian, M. Kleman, and J. Poirier, eds., *Physics of defects* (Elsevier Science Ltd, North Holland, Amsterdam, 1980).

[12] R. Penrose, *Gravitational collapse and space-time singularities,* Phys. Rev. Lett. **14**, 57 (1965).

[13] L. Ting and R. Klein, *Viscous Vortical Flows*, Lecture notes in physics (Springer-Verlag Berlin Heidelberg, Heidelberg, Germany, 1991).

[14] P. Coullet, L. Gil, and F. Rocca, *Optical vortices,* Opt. Commun. **73**, 403 (1989).

[15] M. R. Dennis, K. O'Holleran, and M. J. Padgett, *Singular optics: Optical vortices and polarization singularities,* (Elsevier, 2009) pp. 293 – 363.

[16] L. Novotny and B. Hecht, *Principles of nano-optics* (Cambridge university press, Cambridge, United Kingdom, 2012).

[17] M. V. Berry and M. R. Dennis, *Phase singularities in isotropic random waves,* Proc. R. Soc. Lond. A **456**, 2059 (2000).

[18] G. R. Fowles, *Introduction to modern optics* (Dover Publications, 1989).

[19] M. V. Berry, M. R. Dennis, and R. L. Lee Jr., *Polarization singularities in the clear sky,* New J. Phys. **6**, 162 (2004).

[20] B. Le Feber, N. Rotenberg, and L. Kuipers, *Nanophotonic control of circular dipole emission,* Nat. Commun. **6**, 6695 (2015).

[21] A. Y. Bekshaev, K. Y. Bliokh, and F. Nori, *Transverse spin and momentum in two-wave interference,* Phys. Rev. X **5**, 011039 (2015).

[22] T. Bauer, M. Neugebauer, G. Leuchs, and P. Banzer, *Optical polarization möbius strips and points of purely transverse spin density,* Phys. Rev. Lett. **117**, 013601 (2016).

[23] M. Antognozzi, C. Bermingham, R. Harniman, S. Simpson, J. Senior, R. Hayward, H. Hoerber, M. Dennis, A. Bekshaev, K. Bliokh, *et al.*, *Direct measurements of the extraordinary optical momentum and transverse spin-dependent force using a nano-cantilever,* Nat. Phys. **12**, 731 (2016).

[24] K. Y. Bliokh, A. Y. Bekshaev, and F. Nori, *Optical momentum, spin, and angular momentum in dispersive media,* Phys. Rev. Lett. **119**, 073901 (2017).

[25] Y. Wang and G. Gbur, *Hilbert's hotel in polarization singularities,* Opt. Lett. **42**, 5154 (2017).

[26] T. Fösel, V. Peano, and F. Marquardt, *L lines, c points and chern numbers: understanding band structure topology using polarization fields,* New J. Phys. **19**, 115013 (2017).

[27] S.-H. Gong, F. Alpeggiani, B. Sciacca, E. C. Garnett, and L. Kuipers, *Nanoscale chiral valley-photon interface through optical spin-orbit coupling,* Science **359**, 443 (2018).

[28] H.-J. Stöckmann, *Quantum chaos: an introduction* (Cambridge university press, Cambridge, United Kingdom, 2006).

[29] S. Åberg, T. Guhr, M. Miski-Oglu, and A. Richter, *Superscars in billiards: A model for doorway states in quantum spectra,* Phys. Rev. Lett. **100**, 204101 (2008).

[30] L. Huang, Y.-C. Lai, D. K. Ferry, S. M. Goodnick, and R. Akis, *Relativistic quantum scars,* Phys. Rev. Lett. **103**, 054101 (2009).

[31] G. Wang, L. Huang, Y.-C. Lai, and C. Grebogi, *Nonlinear dynamics and quantum entanglement in optomechanical systems,* Phys. Rev. Lett. **112**, 110406 (2014).

[32] A. J. Taylor and M. R. Dennis, *Vortex knots in tangled quantum eigenfunctions,* Nat. Commun. **7**, 12346 (2016).

[33] M. Akila, D. Waltner, B. Gutkin, P. Braun, and T. Guhr, *Semiclassical identification of periodic orbits in a quantum many-body system,* Phys. Rev. Lett. **118**, 164101 (2017).

[34] S. R. Jain and R. Samajdar, *Nodal portraits of quantum billiards: Domains, lines, and statistics,* Rev. Mod. Phys. **89**, 045005 (2017).

[35] C.-H. Yi, J. Kullig, and J. Wiersig, *Pair of exceptional points in a microdisk cavity under an extremely weak deformation,* Phys. Rev. Lett. **120**, 093902 (2018).

[36] I. Freund, N. Shvartsman, and V. Freilikher, *Optical dislocation networks in highly random media,* Opt. Commun. **101**, 247 (1993).

[37] I. Freund, *Optical vortices in gaussian random wave fields: statistical probability densities,* J. Opt. Soc. Am. A **11**, 1644 (1994).

[38] N. Shvartsman and I. Freund, *Wave-field phase singularities: near-neighbor correlations and anticorrelations,* J. Opt. Soc. Am. A **11**, 2710 (1994).

[39] I. Freund, *Critical-point level-crossing geometry in random wave fields,* J. Opt. Soc. Am. A **14**, 1911 (1997).

[40] I. Freund and V. Freilikher, *Parameterization of anisotropic vortices,* J. Opt. Soc. Am. A **14**, 1902 (1997).

[41] I. Freund and M. Wilkinson, *Critical-point screening in random wave fields,* J. Opt. Soc. Am. A **15**, 2892 (1998).

[42] M. Berry and M. Dennis, *Polarization singularities in isotropic random vector waves,* Proc. R. Soc. Lond. A **457**, 141 (2001).

[43] J. F. Nye, J. V. Hajnal, and H. J. H., *Phase saddles and dislocations in two-dimensional waves such as the tides,* Proc. R. Soc. Lond. A **417**, 7 (1988).

[44] G. P. Karman, M. W. Beijersbergen, A. van Duijl, and J. P. Woerdman, *Creation and annihilation of phase singularities in a focal field,* Opt. Lett. **22**, 1503 (1997).

[45] J. F. Nye, *Unfolding of higher-order wave dislocations,* J. Opt. Soc. Am. A **15**, 1132 (1998).

[46] M. V. Berry, *Wave dislocation reactions in non-paraxial gaussian beams,* Journal of Modern Optics **45**, 1845 (1998).

[47] M. Barth and H.-J. Stöckmann, *Current and vortex statistics in microwave billiards,* Phys. Rev. E **65**, 066208 (2002).

[48] Y.-H. Kim, U. Kuhl, H.-J. Stöckmann, and P. W. Brouwer, *Measurement of long-range wave-function correlations in an open microwave billiard,* Phys. Rev. Lett. **94**, 036804 (2005).

[49] R. Höhmann, U. Kuhl, H.-J. Stöckmann, J. D. Urbina, and M. R. Dennis, *Density and correlation functions of vortex and saddle points in open billiard systems,* Phys. Rev. E **79**, 016203 (2009).

[50] F. Flossmann, K. O'Holleran, M. R. Dennis, and M. J. Padgett, *Polarization singularities in 2D and 3D speckle fields,* Phys. Rev. Lett. **100**, 203902 (2008).

[51] K. O'Holleran, M. R. Dennis, F. Flossmann, and M. J. Padgett, *Fractality of light's darkness,* Phys. Rev. Lett. **100**, 053902 (2008).

[52] K. O'Holleran, M. R. Dennis, and M. J. Padgett, *Topology of light's darkness,* Phys. Rev. Lett. **102**, 143902 (2009).

[53] X. Cheng, Y. Lockerman, and A. Z. Genack, *Phase singularity diffusion,* Opt. Lett. **39**, 3348 (2014).

[54] X. Cheng and A. Z. Genack, *Motion of intensity maxima in averaged speckle patterns of transmitted radiation,* Opt. Lett. **40**, 5279 (2015).

[55] C. Liu, R. E. C. van der Wel, N. Rotenberg, L. Kuipers, T. F. Krauss, A. Di Falco, and A. Fratalocchi, *Triggering extreme events at the nanoscale in photonic seas,* Nat. Phys. **11**, 358 (2015).

[56] J. D. Joannopoulos, S. G. Johnson, J. N. Winn, and R. D. Meade, *Photonic crystals: molding the flow of light* (Princeton university press, Princeton, New Jersey, United States, 2011).

[57] N. Rotenberg and L. Kuipers, *Mapping nanoscale light fields,* Nat. Photonics **8**, 919 (2014).

[58] M. L. M. Balistreri, D. J. W. Klunder, F. C. Blom, A. Driessen, H. W. J. M. Hoekstra, J. P. Korterik, L. Kuipers, and N. F. van Hulst, *Visualizing the whispering gallery modes in a cylindrical optical microcavity,* Opt. Lett. **24**, 1829 (1999).

[59] M. Sandtke, R. J. P. Engelen, H. Schoenmaker, I. Attema, H. Dekker, I. Cerjak, J. P. Korterik, F. B. Segerink, and L. Kuipers, *Novel instrument for surface plasmon polariton tracking in space and time,* Rev. Sci. Instrum. **79**, 013704 (2008).

[60] M. L. M. Balistreri, J. P. Korterik, L. Kuipers, and N. F. van Hulst, *Local observations of phase singularities in optical fields in waveguide structures,* Phys. Rev. Lett. **85**, 294 (2000).

[61] M. Burresi, R. J. P. Engelen, A. Opheij, D. van Oosten, D. Mori, T. Baba, and L. Kuipers, *Observation of polarization singularities at the nanoscale,* Phys. Rev. Lett. **102**, 033902 (2009).

[62] B. Le Feber, N. Rotenberg, D. M. Beggs, and L. Kuipers, *Simultaneous measurement of nanoscale electric and magnetic optical fields,* Nat. Photonics **8**, 43 (2014).

[63] J. A. Veerman, A. M. Otter, L. Kuipers, and N. F. van Hulst, *High definition aperture probes for near-field optical microscopy fabricated by focused ion beam milling,* Applied Physics Letters **72**, 3115 (1998).

[64] D. Courjon, *Near-field microscopy and near-field optics* (World Scientific Publishing Company, London, United Kingdom, 2003).

[65] A. V. Zayats and D. Richards, *Nano-optics and near-field optical microscopy* (Artech house, London, United Kingdom, 2009).

[66] A. F. Koenderink, M. Kafesaki, B. C. Buchler, and V. Sandoghdar, *Controlling the resonance of a photonic crystal microcavity by a near-field probe,* Phys. Rev. Lett. **95**, 153904 (2005).

[67] L. Lalouat, B. Cluzel, P. Velha, E. Picard, D. Peyrade, J. P. Hugonin, P. Lalanne, E. Hadji, and F. de Fornel, *Near-field interactions between a subwavelength tip and a small-volume photonic-crystal nanocavity,* Phys. Rev. B **76**, 041102 (2007).

[68] A. García-Etxarri, I. Romero, F. J. García de Abajo, R. Hillenbrand, and J. Aizpurua, *Influence of the tip in near-field imaging of nanoparticle plasmonic modes: Weak and strong coupling regimes,* Phys. Rev. B **79**, 125439 (2009).

[69] B. Hecht, B. Sick, U. P. Wild, V. Deckert, R. Zenobi, O. J. F. Martin, and D. W. Pohl, *Scanning near-field optical microscopy with aperture probes: Fundamentals and applications,* The Journal of Chemical Physics **112**, 7761 (2000).

[70] M. B. Wabuyele and T. Vo-Dinh, *Nanoimaging of biomolecules using near-field scanning optical microscopy* (CRC Press, 2017) p. 127.

[71] J. Sun, P. S. Carney, and J. C. Schotland, *Strong tip effects in near-field scanning optical tomography,* Journal of Applied Physics **102**, 103103 (2007).

[72] K. Karrai and R. D. Grober, *Piezoelectric tip-sample distance control for near field optical microscopes,* Applied Physics Letters **66**, 1842 (1995).

[73] A. de Hoogh, N. Rotenberg, and L. Kuipers, *Optical singularities in plasmonic fields near single subwavelength holes,* Journal of Optics **16**, 114004 (2014).

[74] M. Hammer, *1D mode solver for dielectric multilayer slab waveguides,* `http://www.computational-photonics.eu/oms.html`, accessed: 21-05-2018.

[75] E. Devaux, A. Dereux, E. Bourillot, J.-C. Weeber, Y. Lacroute, J.-P. Goudonnet, and C. Girard, *Local detection of the optical magnetic field in the near zone of dielectric samples,* Phys. Rev. B **62**, 10504 (2000).

[76] R. L. Olmon, M. Rang, P. M. Krenz, B. A. Lail, L. V. Saraf, G. D. Boreman, and M. B. Raschke, *Determination of electric-field, magnetic-field, and electric-current distributions of infrared optical antennas: A near-field optical vector network analyzer,* Phys. Rev. Lett. **105**, 167403 (2010).

[77] H. Kihm, S. Koo, Q. Kim, K. Bao, J. Kihm, W. Bak, S. Eah, C. Lienau, H. Kim, P. Nordlander, *et al.*, *Bethe-hole polarization analyser for the magnetic vector of light,* Nature communications **2**, 451 (2011).

[78] M. Esslinger and R. Vogelgesang, *Reciprocity theory of apertureless scanning near-field optical microscopy with point-dipole probes,* ACS Nano **6**, 8173 (2012).

[79] A. V. Kildishev, A. Boltasseva, and V. M. Shalaev, *Planar photonics with metasurfaces,* Science **339** (2013), 10.1126/science.1232009.

[80] B. le Feber, *Nanoscale electric and magnetic optical vector fields: mapping & injection* (2015) PhD Thesis.

[81] M. L. M. Balistreri, H. Gersen, J. P. Korterik, L. Kuipers, and N. F. van Hulst, *Tracking femtosecond laser pulses in space and time,* Science **294**, 1080 (2001).

[82] M. Schnell, A. Garcia-Etxarri, J. Alkorta, J. Aizpurua, and R. Hillenbrand, *Phase-resolved mapping of the near-field vector and polarization state in nanoscale antenna gaps,* Nano Letters **10**, 3524 (2010), pMID: 20701270.

[83] V. J. A., G.-P. M. F., K. L., and V. H. N. F., *Single molecule mapping of the optical field distribution of probes for near-field microscopy,* Journal of Microscopy **194**, 477 (2011).

[84] P. Uebel, M. A. Schmidt, H. W. Lee, and P. S. Russell, *Polarisation-resolved near-field mapping of a coupled gold nanowire array,* Opt. Express **20**, 28409 (2012).

[85] N. Rotenberg, T. L. Krijger, B. l. Feber, M. Spasenović, F. J. G. de Abajo, and L. Kuipers, *Magnetic and electric response of single subwavelength holes,* Phys. Rev. B **88**, 241408 (2013).

[86] J. W. Goodman, *Statistical optics* (Wiley, New York, 1985).

[87] L. De Angelis, F. Alpeggiani, A. Di Falco, and L. Kuipers, *Spatial distribution of phase singularities in optical random vector waves,* Phys. Rev. Lett. **117**, 093901 (2016).

[88] D. S. Wilks and R. L. Wilby, *The weather generation game: a review of stochastic weather models,* Prog. Phys. Geog. **23**, 329 (1999).

[89] L. Laloux, P. Cizeau, J.-P. Bouchaud, and M. Potters, *Noise Dressing of Financial Correlation Matrices,* Phys. Rev. Lett. **83**, 1467 (1999).

[90] A. Lagendijk, B. Van Tiggelen, and D. S. Wiersma, *Fifty years of Anderson localization,* Phys. Today **62**, 24 (2009), and references therein.

[91] J. Bertolotti, E. G. van Putten, C. Blum, A. Lagendijk, W. L. Vos, and A. P. Mosk, *Non-invasive imaging through opaque scattering layers.* Nature **491**, 232 (2012).

[92] D. Pierangeli, F. Di Mei, C. Conti, A. J. Agranat, and E. DelRe, *Spatial rogue waves in photorefractive ferroelectrics,* Phys. Rev. Lett. **115**, 093901 (2015).

[93] I. Freund, *Saddles, singularities, and extrema in random phase fields,* Phys. Rev. E **52**, 2348 (1995).

[94] R. Bhandari, *Singularities of the mixed state phase,* Phys. Rev. Lett. **89**, 268901 (2002).

[95] D. M. Palacios, I. D. Maleev, A. S. Marathay, and G. A. Swartzlander, *Spatial correlation singularity of a vortex field,* Phys. Rev. Lett. **92**, 143905 (2004).

[96] S. Vignolini, M. Burresi, S. Gottardo, L. Kuipers, and D. S. Wiersma, *Observation of vortices and field correlations in the near-field speckle of a three-dimensional photonic crystal,* Opt. Lett. **35**, 2001 (2010).

[97] V. Peano, C. Brendel, M. Schmidt, and F. Marquardt, *Topological phases of sound and light,* Phys. Rev. X **5**, 031011 (2015).

[98] N. Rotenberg, B. le Feber, T. D. Visser, and L. Kuipers, *Tracking nanoscale electric and magnetic singularities through three-dimensional space,* Optica **2**, 540 (2015).

[99] A. Fernández-Nieves, V. Vitelli, A. S. Utada, D. R. Link, M. Márquez, D. R. Nelson, and D. A. Weitz, *Novel defect structures in nematic liquid crystal shells,* Phys. Rev. Lett. **99**, 157801 (2007).

[100] E. J. Yarmchuk, M. J. V. Gordon, and R. E. Packard, *Observation of stationary vortex arrays in rotating superfluid helium,* Phys. Rev. Lett. **43**, 214 (1979).

[101] M. Barth and H.-J. Stöckmann, *Current and vortex statistics in microwave billiards,* Phys. Rev. E **65**, 066208 (2002).

[102] R. Höhmann, U. Kuhl, H.-J. Stöckmann, J. D. Urbina, and M. R. Dennis, *Density and correlation functions of vortex and saddle points in open billiard systems,* Phys. Rev. E **79**, 016203 (2009).

[103] J.-D. Urbina and K. Richter, *Random quantum states: recent developments and applications,* Adv. Phys. **62**, 363 (2013).

[104] A. T. Ngo, E. H. Kim, and S. E. Ulloa, *Spatial correlations in chaotic nanoscale systems with spin-orbit coupling,* Phys. Rev. B **84**, 155457 (2011).

[105] J.-P. Hansen and I. R. McDonald, *Theory of simple liquids* (Academic Press, London, 1990).

[106] I. Freund, D. A. Kessler, V. Vasyl'ev, and M. S. Soskin, *Singularity screening in generic optical fields,* Opt. Lett. **40**, 4747 (2015).

[107] B. A. van Tiggelen, D. Anache, and A. Ghysels, *Role of mean free path in spatial phase correlation and nodal screening,* Europhys. Lett. **74**, 999 (2006).

[108] R. L. Olmon, M. Rang, P. M. Krenz, B. A. Lail, L. V. Saraf, G. D. Boreman, and M. B. Raschke, *Determination of electric-field, magnetic-field, and electric-current distributions of infrared optical antennas: A near-field optical vector network analyzer,* Phys. Rev. Lett. **105**, 167403 (2010).

[109] L. D. Angelis and L. Kuipers, *Screening and fluctuation of the topological charge in random wave fields,* Opt. Lett. **43**, 2740 (2018).

[110] S. Balibar, *Physics: The force of fluctuations,* Nature **451**, 136 (2008).

[111] D. Frenkel and B. Smit, *Understanding molecular simulation: from algorithms to applications*, Vol. 1 (Academic press, 2001).

[112] M. M. Genkin, A. Sokolov, O. D. Lavrentovich, and I. S. Aranson, *Topological defects in a living nematic ensnare swimming bacteria,* Phys. Rev. X **7**, 011029 (2017).

[113] S. Prokhorenko, Y. Nahas, and L. Bellaiche, *Fluctuations and topological defects in proper ferroelectric crystals,* Phys. Rev. Lett. **118**, 147601 (2017).

[114] G. Gbur, *Fractional vortex hilbert's hotel,* Optica **3**, 222 (2016).

[115] L. De Angelis, F. Alpeggiani, A. Di Falco, and L. Kuipers, *Persistence and lifelong fidelity of phase singularities in optical random waves,* Phys. Rev. Lett. **119**, 203903 (2017).

[116] H. Yilmaz, E. G. van Putten, J. Bertolotti, A. Lagendijk, W. L. Vos, and A. P. Mosk, *Speckle correlation resolution enhancement of wide-field fluorescence imaging,* Optica **2**, 424 (2015).

[117] R. I. Egorov, M. S. Soskin, D. A. Kessler, and I. Freund, *Experimental measurements of topological singularity screening in random paraxial scalar and vector optical fields,* Phys. Rev. Lett. **100**, 103901 (2008).

[118] M. R. Dennis, *Correlations and screening of topological charges in gaussian random fields,* J. Phys. A-Math. Gen. **36**, 6611 (2003).

[119] D. A. Kessler and I. Freund, *Singularities in speckled speckle: screening,* J. Opt. Soc. Am. A **25**, 2932 (2008).

[120] I. Freund and D. A. Kessler, *Singularities in speckled speckle: Statistics,* Opt. Commun. **281**, 5954 (2008).

[121] I. Freund, R. I. Egorov, and M. S. Soskin, *Umbilic point screening in random optical fields,* Opt. Lett. **32**, 2182 (2007).

[122] A. J. H. Houston, M. Gradhand, and M. R. Dennis, *A random wave model for the aharonov–bohm effect,* J. Phys. A-Math. Theor. **50**, 205101 (2017).

[123] W. G. Cochran, *The $\chi 2$ test of goodness of fit,* Ann. Math. Stat. **23**, 315 (1952).

[124] M. W. Zwierlein, J. R. Abo-Shaeer, A. Schirotzek, C. H. Schunck, and W. Ketterle, *Vortices and superfluidity in a strongly interacting fermi gas,* Nature **435**, 1047 (2005).

[125] K. G. Lagoudakis, M. Wouters, M. Richard, A. Baas, I. Carusotto, R. André, L. S. Dang, and B. Deveaud-Plédran, *Quantized vortices in an exciton–polariton condensate,* Nat. Phys. **4**, 706 (2008).

[126] O. M. Auslaender, L. Luan, E. W. Straver, J. E. Hoffman, N. C. Koshnick, E. Zeldov, D. A. Bonn, R. Liang, W. N. Hardy, and K. A. Moler, *Mechanics of individual isolated vortices in a cuprate superconductor,* Nat. Phys. **5**, 35 (2009).

[127] G. Roumpos, M. D. Fraser, A. Löffler, S. Höfling, A. Forchel, and Y. Yamamoto, *Single vortex-antivortex pair in an exciton-polariton condensate,* Nat. Phys. **7**, 129 (2011).

[128] F. Manni, K. Lagoudakis, T. H. Liew, R. André, V. Savona, and B. Deveaud, *Dissociation dynamics of singly charged vortices into half-quantum vortex pairs,* Nat. Commun. **3**, 1309 (2012).

[129] L. Giomi, *Geometry and topology of turbulence in active nematics,* Phys. Rev. X **5**, 031003 (2015).

[130] R. Barboza, U. Bortolozzo, M. G. Clerc, S. Residori, and E. Vidal-Henriquez, *Optical vortex induction via light–matter interaction in liquid-crystal media,* Adv. Opt. Photon. **7**, 635 (2015).

[131] S. M. Barnett, *Relativistic electron vortices,* Phys. Rev. Lett. **118**, 114802 (2017).

[132] A. Souslov, B. C. van Zuiden, D. Bartolo, and V. Vitelli, *Topological sound in active-liquid metamaterials,* Nat. Phys. (2017), 10.1038/nphys4193.

[133] J. M. Kosterlitz and D. J. Thouless, *Ordering, metastability and phase transitions in two-dimensional systems,* J. Phys. C Solid State **6**, 1181 (1973).

[134] D. Rozas, Z. S. Sacks, and G. A. Swartzlander, *Experimental observation of fluidlike motion of optical vortices,* Phys. Rev. Lett. **79**, 3399 (1997).

[135] M. Dennis, R. King, B. Jack, K. O'Holleran, and M. Padgett, *Isolated optical vortex knots,* Nat. Phys. **6**, 118 (2010).

[136] L. Giomi, M. J. Bowick, X. Ma, and M. C. Marchetti, *Defect annihilation and proliferation in active nematics,* Phys. Rev. Lett. **110**, 228101 (2013).

[137] M. V. Berry, *Nature's optics and our understanding of light,* Contemp. Phys. **56**, 2 (2015).

[138] M. V. Berry, *Regular and irregular semiclassical wavefunctions,* J. Phys. A-Math. Gen. **10**, 2083 (1977).

[139] L. De Angelis, F. Alpeggiani, and L. Kuipers, *Spatial bunching of same-index polarization singularities in two-dimensional random vector waves,* Phys. Rev. X **8**, 041012 (2018).

[140] B. Hensen, H. Bernien, A. E. Dréau, A. Reiserer, N. Kalb, M. S. Blok, J. Ruitenberg, R. F. Vermeulen, R. N. Schouten, C. Abellán, *et al.*, *Loophole-free bell inequality violation using electron spins separated by 1.3 kilometres,* Nature **526**, 682 (2015).

[141] A. F. Koenderink, A. Alù, and A. Polman, *Nanophotonics: Shrinking light-based technology,* Science **348**, 516 (2015).

[142] A. Polman, M. Knight, E. C. Garnett, B. Ehrler, and W. C. Sinke, *Photovoltaic materials: Present efficiencies and future challenges,* Science **352** (2016), 10.1126/science.aad4424.

[143] A. de Hoogh, L. Kuipers, T. Visser, and N. Rotenberg, *Creating and controlling polarization singularities in plasmonic fields,* Photonics **2**, 553–567 (2015).

[144] K. Shibata, T. Tanigaki, T. Akashi, H. Shinada, K. Harada, K. Niitsu, D. Shindo, N. Kanazawa, Y. Tokura, and T.-h. Arima, *Current-driven motion of domain boundaries between skyrmion lattice and helical magnetic structure,* Nano Lett. **18**, 929 (2018).

[145] C. Reichhardt and C. O. Reichhardt, *Noise fluctuations and drive dependence of the skyrmion hall effect in disordered systems,* New J. Phys. **18**, 095005 (2016).

[146] A. Fert, N. Reyren, and V. Cros, *Magnetic skyrmions: advances in physics and potential applications,* Nat. Rev. Mater. **2**, 17031 (2017).

[147] T. N. Shendruk, A. Doostmohammadi, K. Thijssen, and J. M. Yeomans, *Dancing disclinations in confined active nematics,* Soft Matter **13**, 3853 (2017).

[148] J. M. Yeomans, *Active matter: Playful topology,* Nat. Mater. **13**, 1004 (2014).

[149] T. B. Saw, A. Doostmohammadi, V. Nier, L. Kocgozlu, S. Thampi, Y. Toyama, P. Marcq, C. T. Lim, J. M. Yeomans, and B. Ladoux, *Topological defects in epithelia govern cell death and extrusion,* Nature **544**, 212 (2017).

[150] A. Doostmohammadi, M. F. Adamer, S. P. Thampi, and J. M. Yeomans, *Stabilization of active matter by flow-vortex lattices and defect ordering,* Nat. Commun. **7**, 10557 (2016).

[151] M. Dennis, *Polarization singularities in paraxial vector fields: morphology and statistics,* Opt. Commun. **213**, 201 (2002).

[152] F. Flossmann, U. T. Schwarz, M. Maier, and M. R. Dennis, *Polarization singularities from unfolding an optical vortex through a birefringent crystal,* Phys. Rev. Lett. **95**, 253901 (2005).

[153] S. Barkhofen, J. J. Metzger, R. Fleischmann, U. Kuhl, and H.-J. Stöckmann, *Experimental observation of a fundamental length scale of waves in random media,* Phys. Rev. Lett. **111**, 183902 (2013).

[154] B. Redding, S. F. Liew, R. Sarma, and H. Cao, *Compact spectrometer based on a disordered photonic chip,* Nat. Photonics **7**, 746 (2013).

[155] T. Strudley, D. Akbulut, W. L. Vos, A. Lagendijk, A. P. Mosk, and O. L. Muskens, *Observation of intensity statistics of light transmitted through 3d random media,* Opt. Lett. **39**, 6347 (2014).

[156] Z. Shi, M. Davy, and A. Z. Genack, *Statistics and control of waves in disordered media,* Opt. Express **23**, 12293 (2015).

[157] D. Pierangeli, A. Tavani, F. Di Mei, A. J. Agranat, C. Conti, and E. DelRe, *Observation of replica symmetry breaking in disordered nonlinear wave propagation,* Nat. Commun. **8**, 1501 (2017).

[158] N. Bender, H. Yilmaz, Y. Bromberg, and H. Cao, *Customizing speckle intensity statistics,* Optica **5**, 595 (2018).

[159] A. Mohtashami, C. I. Osorio, and A. F. Koenderink, *Angle-resolved polarimetry of antenna-mediated fluorescence,* Phys. Rev. Appl. **4**, 054014 (2015).

[160] J. F. Nye, *Lines of circular polarization in electromagnetic wave fields,* Proc. R. Soc. Lond. A **389**, 279 (1983).

[161] M. R. Dennis, *Polarization singularity anisotropy: determining monstardom,* Opt. Lett. **33**, 2572 (2008).

[162] B. A. Cvarch, B. Khajavi, J. A. Jones, B. Piccirillo, L. Marrucci, and E. J. Galvez, *Monstar polarization singularities with elliptically-symmetric q-plates,* Opt. Express **25**, 14935 (2017).

[163] J. A. Barker and D. Henderson, *What is "liquid"? understanding the states of matter,* Rev. Mod. Phys. **48**, 587 (1976).

[164] A. P. Lyubartsev and A. Laaksonen, *Calculation of effective interaction potentials from radial distribution functions: A reverse monte carlo approach,* Phys. Rev. E **52**, 3730 (1995).

[165] M. Baldini, P. Postorino, L. Malavasi, C. Marini, K. W. Chapman, and H.-k. Mao, *Pair distribution function analysis: The role of structural degrees of freedom in the high-pressure insulator to metal transition of* vo_2, Phys. Rev. B **93**, 245137 (2016).

[166] B. A. Frandsen, M. Brunelli, K. Page, Y. J. Uemura, J. B. Staunton, and S. J. L. Billinge, *Verification of anderson superexchange in mno via magnetic pair distribution function analysis and ab initio theory,* Phys. Rev. Lett. **116**, 197204 (2016).

[167] N. Thaicharoen, A. Schwarzkopf, and G. Raithel, *Control of spatial correlations between rydberg excitations using rotary echo,* Phys. Rev. Lett. **118**, 133401 (2017).

[168] J. M. Sobstyl, T. Emig, M. J. A. Qomi, F.-J. Ulm, and R. J.-M. Pellenq, *Role of city texture in urban heat islands at nighttime,* Phys. Rev. Lett. **120**, 108701 (2018).

[169] J.-P. Hansen and I. R. McDonald, *Theory of simple liquids* (Academic Press, London, 1990).

[170] H. Snijders, J. Frey, J. Norman, M. Bakker, E. Langman, A. Gossard, J. Bowers, M. Van Exter, D. Bouwmeester, and W. Löffler, *Purification of a single-photon nonlinearity,* Nat. Commun. **7**, 12578 (2016).

[171] W. V. Li and A. Wei, *Gaussian integrals involving absolute value functions,* in *High Dimensional Probability V: The Luminy Volume*, Vol. 5, edited by C. Houdré, V. Koltchinskii, D. M. Mason, and M. Peligrad (Institute of Mathematical Statistics, Beachwood, Ohio, USA, 2009) pp. 43–59.

[172] W. H. Press, S. A. Teukolsky, W. T. Vetterling, and B. P. Flannery, *Numerical Recipes: The Art of Scientific Computing (3rd ed.)* (Cambridge University Press, New York, 2007).

[173] S. N. Alperin and M. E. Siemens, *Angular momentum of topologically structured darkness,* Phys. Rev. Lett. **119**, 203902 (2017).

[174] G. Milione, H. I. Sztul, D. A. Nolan, and R. R. Alfano, *Higher-order poincaré sphere, stokes parameters, and the angular momentum of light,* Phys. Rev. Lett. **107**, 053601 (2011).

[175] K. Volke-Sepulveda, V. Garcés-Chávez, S. Chávez-Cerda, J. Arlt, and K. Dholakia, *Orbital angular momentum of a high-order bessel light beam,* Journal of Optics B: Quantum and Semiclassical Optics **4**, S82 (2002).

[176] F. Cardano, E. Karimi, S. Slussarenko, L. Marrucci, C. de Lisio, and E. Santamato, *Polarization pattern of vector vortex beams generated by q-plates with different topological charges,* Appl. Opt. **51**, C1 (2012).

[177] M. Neugebauer, T. Bauer, A. Aiello, and P. Banzer, *Measuring the transverse spin density of light,* Phys. Rev. Lett. **114**, 063901 (2015).

[178] D. Naidoo, F. S. Roux, A. Dudley, I. Litvin, B. Piccirillo, L. Marrucci, and A. Forbes, *Controlled generation of higher-order poincaré sphere beams from a laser,* Nature Photonics **10**, 327 (2016).

[179] H. Rubinsztein-Dunlop, A. Forbes, M. V. Berry, M. R. Dennis, D. L. Andrews, M. Mansuripur, C. Denz, C. Alpmann, P. Banzer, T. Bauer, *et al., Roadmap on structured light,* Journal of Optics **19**, 013001 (2017).

[180] L. Dominici, G. Dagvadorj, J. M. Fellows, D. Ballarini, M. De Giorgi, F. M. Marchetti, B. Piccirillo, L. Marrucci, A. Bramati, G. Gigli, M. H. Szymańska, and D. Sanvitto, *Vortex and half-vortex dynamics in a nonlinear spinor quantum fluid,* Sci. Adv. **1**, E1500807 (2015).

[181] B. Zhen, C. W. Hsu, L. Lu, A. D. Stone, and M. Soljačić, *Topological nature of optical bound states in the continuum,* Phys. Rev. Lett. **113**, 257401 (2014).

[182] H. M. Doeleman, F. Monticone, W. Hollander, A. Alù, and A. F. Koenderink, *Experimental observation of a polarization vortex at an optical bound state in the continuum,* Nat. Photonics **12**, 397 (2018).

[183] H. Gersen, J. P. Korterik, N. F. van Hulst, and L. Kuipers, *Tracking ultrashort pulses through dispersive media: Experiment and theory,* Phys. Rev. E **68**, 026604 (2003).

[184] H. Gersen, D. J. W. Klunder, J. P. Korterik, A. Driessen, N. F. van Hulst, and L. Kuipers, *Propagation of a femtosecond pulse in a microresonator visualized in time,* Opt. Lett. **29**, 1291 (2004).

[185] H. Gersen, E. M. H. P. van Dijk, J. P. Korterik, N. F. van Hulst, and L. Kuipers, *Phase mapping of ultrashort pulses in bimodal photonic structures: A window on local group velocity dispersion,* Phys. Rev. E **70**, 066609 (2004).

[186] H. Dym and H. McKean Jr, *Fourier series and integrals* (Academic Press, London, 1972).

[187] M. Tinkham, *Group theory and quantum mechanics* (McGraw Hill, Inc., New York, United States, 1964).

[188] D. Levine and P. J. Steinhardt, *Quasicrystals: A new class of ordered structures,* Phys. Rev. Lett. **53**, 2477 (1984).

[189] M. C. Marchetti, J. F. Joanny, S. Ramaswamy, T. B. Liverpool, J. Prost, M. Rao, and R. A. Simha, *Hydrodynamics of soft active matter,* Rev. Mod. Phys. **85**, 1143 (2013).

[190] G. Blatter, M. V. Feigel'man, V. B. Geshkenbein, A. I. Larkin, and V. M. Vinokur, *Vortices in high-temperature superconductors,* Rev. Mod. Phys. **66**, 1125 (1994).

[191] W. Ahn, S. V. Boriskina, Y. Hong, and B. M. Reinhard, *Electromagnetic field enhancement and spectrum shaping through plasmonically integrated optical vortices,* Nano Lett. **12**, 219 (2012).

ACKNOWLEDGEMENTS

Here we are at the end credits of my doctorate. The four year story behind this dissertation is rich in emotions, difficult and exciting situations, amusement and frustration, insecurity and confidence. As in every good story, this one is also full of characters: people who contributed to it in countless different ways. The results of these experiences go way beyond what can be written in a doctoral thesis. My personal development has been shaped by the past four years in ways that I could not have imagined. I am extremely grateful for it.

It is always a good idea to start at the beginning. I am very thankful to **Kobus** for giving me the possibility to work in his group. But beyond that, I am grateful that he always made sure that working in his group meant being a part of a highly stimulating and friendly environment. I had the luxury of benefiting from his expert guidance and having feeling of scientific freedom. It may sound like a paradox, but getting the best of both worlds as a student allowed me to grow immensely as a scientist. It is striking how Kobus can come out from a meeting and catch up with your physics in no time. But even better is how he continuously demonstrates a deep awareness and integrity. I admire the person Kobus is and I am grateful to have had such a role model early on in my career.

A big gratitude also goes to **Andrea**, without whom the chaotic cavity would not have existed, as well as this thesis. I enjoyed our scientific discussions and I can only wish we had the opportunity to interact more. I hope this opportunity will come in the future.

The first steps are always the most difficult. I am glad that since the very beginning I found a supportive team in the NanoOptics group. These people have been essential in getting me started rather than lost. I am grateful for the time spent in the lab with **Ruben**, who initiated me to the troublesome art of near-field microscopy. It was a privilege to drop by the office of **Boris**, I treasured all his tips and considered him as a great role model. It is also thanks to **Matthias** that I could take over the python minority tradition of the group. Thanks to **Anouk** for introducing me to the magic world of singularities and to **Nir** that pushed me along my first small research project. The time I shared with all of you was too short, but vital.

My PhD was also my first experience in a professional environment. I could not hope for a better place than my lively corner office. That was mainly thanks to my office mates **Alexei**, **Sebastian** and **Sander**. You all helped to make my days brighter and whenever I needed advice I knew I could bother you. I am privileged to still not know what a nasty office environment looks like. Moreover, I am happy to have three more friends, even though they are scattered around the world.

In general, **AMOLF** was a great setting for my personal growth. I felt at home with all the members of the scientific staff, technical and non-technical support. There are only a few problems in the universe that **Hinco** is not able to solve. His presence was crucial for facing many of the hardest challenges I experienced. The interactions with

Marco, **Idsart** and **Jan** were always great opportunities to learn more of the multitude of technicalities behind a state-of-the-art near-field microscope. I was impressed by the efficiency of **Sabine**, **Roos** was always very friendly and helpful. What makes AMOLF a great place is that it really feels like being part of a big team, where everybody contributes to the success of the whole institute. I have made so many friends at AMOLF and ARCNL that it is impossible to name them all. I thank all of these wonderful people for the weeks, months, years we spent together. It has been a lot of fun!

When **Nikhil** and **Dolfine** joined the group, I not only found two great companions of doctoral challenges, but two very good friends. Going to a summer school with you was an excellent and fun way to start our paths together. Events and circumstances moved us apart and I fear the physical distance will only increase with time. Nevertheless, I feel a strong connection, which I see to be long lasting. Having **Irina** as a colleague was another opportunity that I felt as too short. I treasured her wisdom and enjoyed her vitality. It was important to find in **Filippo** that senior member of the group that I missed for a long time. I am lucky I could share so much of my work with a person of his inherent talent and astonishing intuition for physics. During my PhD, I realized that academia is not a bowl of cherries. It can be a nasty environment, competitive and impregnated with arrogance. I was extremely lucky to meet **Su-Hyun**, who everyday demonstrated to everyone that much more can be achieved with modesty and kindness. She silently helped me moving through some of the toughest times of my PhD. An injection of daily smiles that kept me up and running. A happy island that healed me.

At some point during the last paragraph, we ended up moving to **TU Delft**. It is only thanks to some of the people that I am naming in these pages that such a transition in both my professional and personal life could take place. It was a humongous challenge to move a scientific laboratory. It was psychologically demanding to start everything over in a new – hypothetically hostile – environment. Luckily things never stay as they are at the beginning and soon the group started breathing a new life. This is thanks to **Felipe**, **Aron**, **Thomas**, **Irina** (a new one!), **Thijs** and **Martin**. Your vibe revitalized my motivation and that of the whole group. I am happy to leave the NanoOptics lab in good hands and now it is in great shape.

As a matter of fact, the environment at TU Delft was anything but hostile. It was great to have **Heleen**, **Etty** and **Tino**, who made sure our arrival was smooth and cheerful. New working place means new office, and once again I was lucky. Besides Su-Hyun, I was happy to share my space with **Felix** and **Nikos**. In the past year or two we shared opinions and points of view on many matters. They were the first connections I could make in TU Delft, and I am glad they are still among the strongest. Another person that contributed a lot in making me feel part of the TU Delft family was **Giordano**. Incredibly friendly and ingenious, I hold him in very high regard. It was great to enjoy some good beach volley together during your last months in Delft. It was a lot of fun to work together with **Daniel**. This was helpful both for bringing me back to the lab and for learning a lot of new things, from a very brilliant and enthusiastic person.

The acknowledgments are naturally drifting towards personal aspects rather than professional ones. There is one person that I met right at the beginning of my PhD. He was always there in the fun moments as well as in the difficult ones. What is awesome about **Alessandro** is that you know you can count on him. The only difficulty you can

have with Ale is not being able to keep up with his rhythm and sometimes it happens that you have to let him down. And it is always a difficult choice, believe me. However, I also met a few people that were able to keep up with him. Among these people there are **Giorgios** and **Nicola**, with whom it was always great to hang out. It is amusing that during "one of those nights", in which the party was maybe a bit "too happy", we accidentally introduced ourselves to **Marco**. It will be difficult to stop laughing at the idea that his first impression of us was "who are these crazy people screaming Italian songs at 2 a.m. in the morning?". Well begun is half done! I am happy to have lived just below you and I am still eager to elicit some of your northern cooking secrets. It was a lot of fun – and worth testifying – that together with Alessandro, Nicola and Marco we managed to form an extraordinary **rowing crew**. I really enjoyed cutting through the water of the Amstel with you, in our unconvincing conditions and guided by debatable mentors.

The "Italian family" kept growing and growing. I am lucky to have found a good friend in **Vanessa**, with whom I can share a lot of values and interests (and coffees!). It is thanks to her that I also met **Domenico**, one of these people who is always worth meeting. To spend time with **Giorgio** is always exciting and rewarding. His creativity has no equals and his broad interests make him a person who will never bore you. I am thankful for all the time I shared with **Giulia**. She has probably been the first person I met outside working hours. Although it sounds like a long time ago, and many things have changed, the connection is still there.

The warmest thanks goes to my parents **Luigi** e **Renata**. The roots that make me feel safe, the motivation to look ahead. I cannot know how difficult it was for you to have me distant for all this time. But I can imagine, because it was tough for me to know you far away. You gave me wings with which to fly, I will be happy to use them to fly close to you. A brother is friend and family at the same time. My relationship with **Michele** is like a good wine, it only improves with time. Over these years I felt your thoughts always with me, and I know you felt mine with you. We do not need to be together to feel together, because we know we are always on the same side. Thanks for being there. It is priceless to have such a life reference. A grandma is more than family, it is a bless. Thanks nonna **Maddalena** to be such a great presence in my life and source of unconditional love.

Friends come and go, but the precious ones remain. Besides family, **Emanuele** is the closest person to me, even at thousands of kilometers of distance and following weeks without hearing from each other. He kept the lights on during my dark times and during the bright ones as well, for many years past and many more to come. To know **Piergiorgio** gives me the same feeling. A person I can always feel by my side, and who in addition is a lot of fun to be with. Again, distance seems not an issue here. **Daniele** was an essential reference for my days back in Italy, it is a great fortune to have a friend like him you can count on. The same goes for **Stefano**, another good mix of family and friendship, and a continuous inspiration.

It would be unfair not to spend a single line for the person who was by my side for the largest fraction of these four years. We left together on this adventure, overcame many obstacles and enjoyed beautiful days that were worth living. It is odd that we parted ways. *Because life is not a mathematical shape or calculation, but a wonder.*[12]

QUOTES BIBLIOGRAPHY

1. The Beatles, *All you need is love* (Olympic Sound Studios, London, United Kingdom, 1967).
2. J. K. Rowling, *Harry Potter and the Prisoner of Azkaban* (Bloomsbury, London, United Kingdom, 1999).
3. Luigi Pirandello, *Quaderni di Serafino Gubbio operatore* (Bemporad, Firenze, Italy, 1925).
4. Ernest Hemingway, *The Old Man and The Sea* (Charles Scribner's Sons, New York City, United States, 1952).
5. Gorgias, *On Nature or the Non-Existent* (Leontinoi, Sicily, c. 485 BC – c. 380 BC).
6. Julian Barnes, *The Noise of Time* (Jonathan Cape, London, United Kingdom, 2016).
7. Erri De Luca, *Il Contrario di Uno* (Feltrinelli, Milano, Italy, 2003).
8. Kurt Vonnegut, *Cat's Cradle* (Holt, Rinehart and Winston, New York City, United States, 1963).
9. Edoardo Bennato, *L'isola che non c'è* (Ricordi, Milano, Italy, 1980).
10. Lewis Carroll, *Alice's Adventures in Wonderland* (MacMillan, London, United Kingdom, 1865).
11. Walt Disney Animation Studios, *Frozen* (Walt Disney Pictures, Burbank, California, United States, 2013).
12. Hermann Hesse, *La Cura* (Adelphi, Milano, Italy, 1978).

CURRICULUM VITÆ

Lorenzo DE ANGELIS

06-01-1990 Born in Ronciglione, Italy.

EDUCATION

2004–2009 Scientific High School
Liceo Scientifico A. Meucci, Ronciglione, Italy

2009–2012 Bachelor in Physics
Sapienza University, Rome, Italy

2012–2014 Master in Condensed Matter Physics
Sapienza University, Rome, Italy
Thesis: Study, development and characterization of nanostructured substrates for Surfaced Enhanced Raman Scattering
Promotor: Prof. dr. P. Postorino

2014 Ph.D. in Physics
AMOLF, Amsterdam, The Netherlands (2014–2016)
TU Delft, Delft, The Netherlands (2016–2018)
Thesis: The Singular Optics of Random Light
Promotor: Prof. dr. L. Kuipers

AWARDS

2015 Laureato Eccellente (Ass. NoiSapienza)

2016 Best Poster (NNV AMO Lunteren)

2017 "Emil Wolf" Award (The Optical Society)

2018 "Emil Wolf" Award (The Optical Society)

LIST OF PUBLICATIONS

9. **L. De Angelis** and L. Kuipers, *Effective Interaction of Phase Singularities in Random Waves*, In Preparation.

8. **L. De Angelis**, F. Alpeggiani, T. Bauer and L. Kuipers, *Polarization Vortices Unbalance in Two-Dimensional Random Vector Waves*, In Preparation.

7. D. V. Verschueren, S. Pud, X. Shi, **L. De Angelis**, L. Kuipers, and C. Dekker, *Label-free optical detection of DNA translocations through plasmonic nanopores*, In Review.

6. **L. De Angelis**, F. Alpeggiani, and L. Kuipers, *Spatial Bunching of Same-Index Polarization Singularities in Two-Dimensional Random Vector Waves*, Physical Review X **8**, 041012 (2018).

5. **L. De Angelis** and L. Kuipers, *Screening and fluctuation of the topological charge in random wave fields*, Optics Letters **43**, 12 (2018).

4. **L. De Angelis**, F. Alpeggiani, A. Di Falco, and L. Kuipers, *Persistence and Lifelong Fidelity of Phase Singularities in Optical Random Waves*, Physical Review Letters **119**, 203903 (2017).

3. **L. De Angelis**, F. Alpeggiani, A. Di Falco, and L. Kuipers, *Spatial Distribution of Phase Singularities in Optical Random Vector Waves*, Physical Review Letters **117**, 093901 (2016).

2. F. Domenici, C. Fasolato, E. Mazzi, **L. De Angelis**, F. Brasili, F. Mura, P. Postorino, F. Bordi, *Engineering microscale two-dimensional gold nanoparticle cluster arrays for advanced Raman sensing: An AFM study* Colloids and surfaces A: Physicochemical and engineering aspects **498**, 168-175 (2016).

1. C. Fasolato, F. Domenici, S. Sennato, F. Mura, **L. De Angelis**, F. Luongo, F. Costantini, F. Bordi, P. Postorino, *Dimensional scale effects on surface enhanced Raman scattering efficiency of self-assembled silver nanoparticle clusters* Applied Physics Letters **105**, 073105 (2014).